Università degli Studi di Genova
Facoltà di Scienze Matematiche Fisiche e Naturali

Ph.D. Thesis

# Statistical properties of mixing in Rayleigh–Taylor turbulence

**by**

*Lara Vozella*

**Supervisor:**
*Prof. Andrea Mazzino*

**Co-supervisor:**
*Prof. Guido Boffetta*

XXI Ciclo di Dottorato (2006-2008)

Settore scientifico-disciplinare: FIS/02

# Statistical properties of mixing in Rayleigh–Taylor turbulence

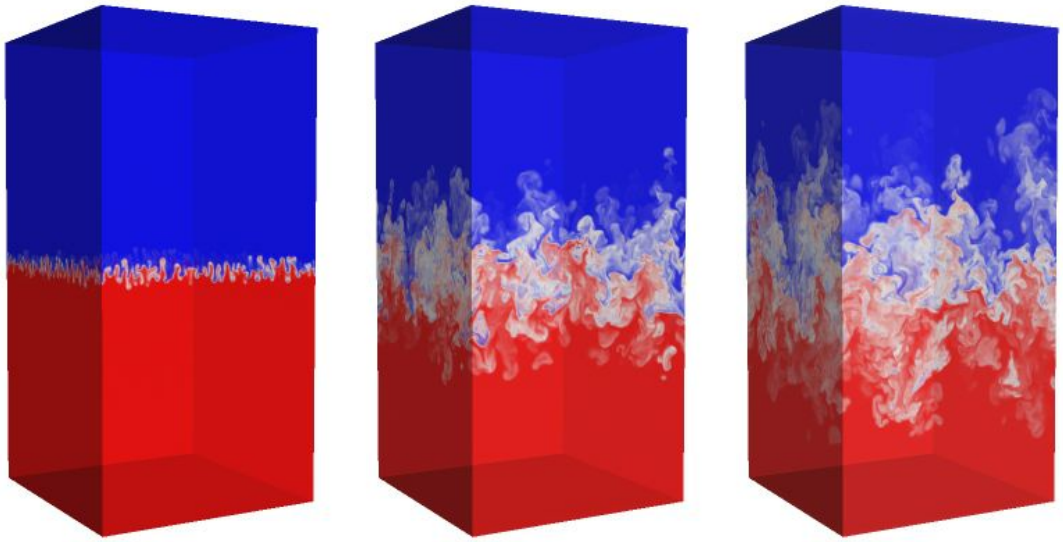

*"It is shown that, when two superposed fluids of different densities are accelerated in a direction perpendicular to their interface, this surface is stable or unstable according to whether the acceleration is directed from the heavier to the lighter fluid or vice versa..."*
Sir G. Taylor The instability of liquid surfaces when accelerated in a direction perpendicular to their planes. I. *Proc. R. Soc. A*, 201:192–197, 1950

*"La vita è un'opportunità, traine profitto.*
*La vita è bellezza, ammirala.*
*La vita è benedizione, sperimentalo.*
*La vita è sogno, realizzalo.*
*La vita è una sfida, accettala.*
*La vita è un dovere, portalo a termine.*
*La vita è un gioco, giocalo.*
*La vita è un bene, salvaguardalo.*
*La vita è amore, godilo.*
*La vita è mistero, scoprilo.*
*La vita è una promessa, adempila.*
*La vita è dolore, superalo.*
*La vita è un canto, cantalo.*
*La vita è una lotta, accettala.*
*La vita è una tragedia, sappi tenerle testa.*
*La vita è un'avventura, osala.*
*La vita è vita, preservala.*
*La vita è fortuna, approfittane.*
*La vita è troppo preziosa, non distruggerla."*
Madre Teresa di Calcutta

*"... All men dream: but nor equally.*
*Those who dream by night*
*in the dusty recesses*
*of their minds*
*wake in the day to find that it was vanity.*
*But the dreamers of the day*
*are dangerous men,*
*for they may act their dream*
*with open eyes,*
*to make it possible..."*
Seven pillars of wisdom by Thomas Edward Lawrence (1922)

# Contents

# Introduction

The main concern of the present thesis is the investigation (at both theoretical and numerical level) of the statistical properties of turbulent mixing in the context of the Rayleigh–Taylor instability.
The Rayleigh–Taylor (RT) instability is a fluid-mixing mechanism occurring at the interface between two fluids of different densities, subjected to an external acceleration. A simple RT system consists of two homogeneous fluids under gravity, with the heavy fluid placed on top of the light one. If a disturbance is imposed on the interface, the instability develops and a mixing region, between fluids, grows up.
Such a mechanism was first discovered by Lord Rayleigh in the 1880s for a fluid in a gravitational field [120], and later applied to all accelerated fluids by Sir Geoffrey Taylor in 1950 [138] (see Fig. 1).

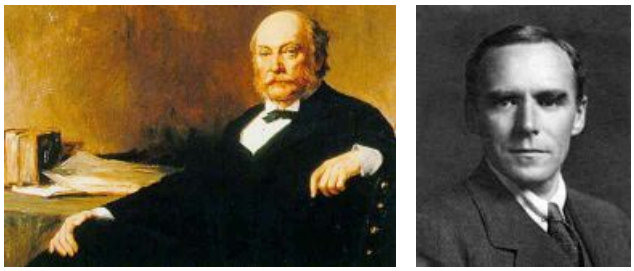

**(a)** Lord Rayleigh **(b)** Sir Taylor

**Figure 1: (a)** In 1883, Lord Rayleigh, motivated by a better comprehension of the formation of *cirrus* clouds, analysed the interfacial motion that occurs when a heavy fluid is supported by a lighter one. In his study the idealised case of two incompressible immiscible fluids with a constant gravitational field is considered [120]. **(b)** In 1950 Sir Taylor realised that the configuration studied by Lord Rayleigh is equivalent to the case without gravity and the lighter fluid accelerating into the heavier one [138].

The relevance of this mixing mechanism embraces several phenomena occurring in completely different contexts. We just mention, among the many, astrophysical supernovae [26, 155], solar-flare formation [76], cloud formation in atmospheric sciences [125], geophysical formations like salt domes and volcanic islands [51, 53], continental magmatism caused by lithospheric gravitational instability [56, 91]. In Fig. 2, the descriptions of some of these natural

phenomena are reported. RT instability also plays a crucial role in inertial confinement fusion [121], as it finally causes fuel-pusher mixing that potentially quenches thermonuclear ignition. The suppression of the RT instability is thus absolutely crucial for the ultimate goal of inertial fusion energy [62].

**(a)** Supernovae **(b)** Solar flares **(c)** Mammatus clouds

**Figure 2:** Some examples where RT instability plays a crucial role. **(a)** Supernovae. RT-driven turbulence is the dominant acceleration mechanism for thermonuclear flames in type-Ia supernovae. In addition to producing many intermediate mass elements, type-Ia supernovae serve as standard candles for measuring the rate of expansion of the universe. They begin as carbon-oxygen white dwarfs, which accrete mass from a companion star. When the mass of the white dwarf reaches the Chandrasekhar limit of 1.4 solar masses, ignition occurs near the centre, thus generating a thermonuclear flame front. The expansion of ashes behind the front causes the flame to become RT unstable as it propagates outward. Uncertainties remain at all stages of the process: from how it ignites to how the flame accelerates. A major difficulty in supernova modelling is the need to cover the vast dynamic range associated with high-Reynolds-number turbulence: from the $10^8$ cm radius of the dwarf down to the $10^{-4}$ cm thickness of the flame [155]. No single simulation can encompass all length scales, so approximations must be made [26, 155]. **(b)** Solar Flares. The magnetic flux emerges from the solar surface in the form of dark filaments connecting small sunspots with opposite polarities. These filamentary structures arise spontaneously from the magnetic RT instability [76]. **(c)** Mammatus clouds. The *Glossary of Meteorology* defines Mammatus cloud as "hanging protuberances, like pouches, on the undersurface of a cloud". These clouds are an enigma of atmospheric fluid dynamics: relatively little is known about their formation mechanism, microphysics and dynamics. RT instability is one of the proposed formation mechanisms [125].

Back to classical fluid applications, RT instability is the first step eventually leading to a fully developed turbulent regime. A deeper understanding of the mechanism of flows driven by RT instability would thus shed light on the many processes that underpin fully developed turbulence.

The difficulty inherent in sustaining an unstable density stratification has challenged experimentalists for over half a century. Several innovative approaches have recently been developed (see, e.g., [118]). With the advent of supercomputers, high-resolution numerical simulations of RT at high Reynolds numbers have become a reality. However, simulations using many different benchmark codes and experiments already disagree on apparently innocent observables such as, for instance, the value of the growth constant, $\alpha$, associated to the spread of the turbulent mixing zone (see, e.g., [51]). The differences can be as high as $100\%$.

Despite the long history of RT turbulence, consistent phenomenological theories have been presented only recently, in the 2000s, by Chertkov and coworkers [41, 43] both in the absence (the so-called miscible configuration) and in the presence of surface tension (the so-called immiscible configuration). In the case of negligible surface-tension effects, an alternative theory, leading to totally different conclusions, has been formulated by Poujade [114]. These theories have some intrinsic limitations. Indeed their results constitute a set of mean-field predictions for relevant statistical observables (e.g., the moments of velocity/density differences on different scales) in the mixing zone. These predictions need to be verified numerically or experimentally in order to understand the role of fluctuations and more specifically their effects on intermittency and anomalous scaling.

The aforementioned works represent the starting point of our investigation. We consider the simple configuration of two homogeneous fluids in gravitational field in the limit of small differences of densities. This choice simplifies the numerical investigation thus allowing us a more extensive exploration of the mixing properties. Different configurations are analysed: both the two- and the three-dimensional miscible cases, and the two-dimensional immiscible one. The necessity of studying both two- and three-dimensional configurations is due to the expected different turbulent pictures. This expectation is based on the fact that two-dimensional and three-dimensional hydrodynamical turbulence are ruled by a totally different physics.

As far as the miscible system is concerned, an idea of the mixing-region development is given in Fig. 3, where we report the temporal evolution of the density field in the three-dimensional configuration, as obtained by our numerical simulations. The investigation of statistical properties in the turbulent mixing zone is our first concern. The turbulence regime

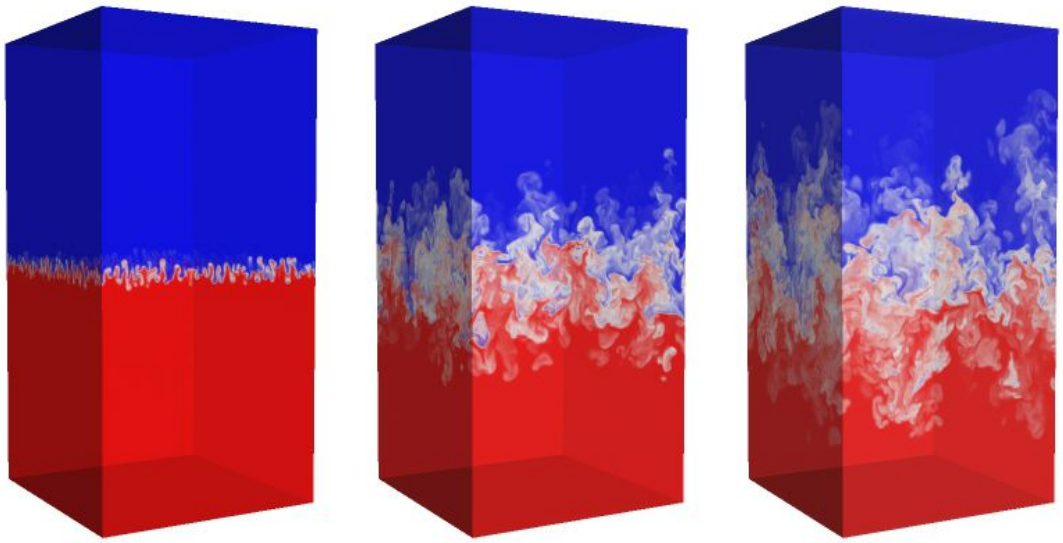

**Figure 3:** Three snapshots of the temporal evolution of three-dimensional miscible RT turbulence. Colours are coded in a way that blue represents the denser fluid and red the lighter one. Gravity is directed downward. Time grows from left to right. See Chap. 3 for more details.

is characterised by a huge nonlinearly coupled number of degrees of freedom: the scale of

energy injection, where turbulence is excited, differs dramatically from the scale of energy damping, where the dissipation takes place. Moreover, nonlinear interactions strongly couple the degrees of freedom by transferring excitations from the injection to the damping scale throughout the intermediate scales. The ensuing complicated and irregular dynamics calls for a statistical description. Therefore, we focus on determination of scaling laws of relevant statistical observables in the mixing region and we investigate the merit and the limit of the aforementioned phenomenological theories. Moreover, we show how to extend these phenomenological theories by taking into account the intermittency corrections. The intermittency phenomenon which refers to the violation of dimensional predictions for the scaling laws, reflects a breakdown of scale invariance. The statistics at a certain scale cannot be obtained by a simple rescaling of the statistics at another scale. The latter extension analysis allows us to include the RT problem in a wider-ranging context. Indeed, the intermittency corrections are found to be consistent with the scenario of universality of Navier–Stokes turbulence with respect to the forcing mechanism. The universality issue in Navier–Stokes is one of the most relevant and unsolved theoretical problems in modern turbulence theory. As far as the immiscible configuration is concerned, the RT instability appear even richer than the corresponding miscible situation. Indeed, the evolution is characterised by the interplay between hydrodynamical degrees of freedom and those associated to surface tension. Our main aim is to highlight this interaction in a turbulence regime. Regarding the latter regime, numerical accuracy and efficiency are fundamental requirements to reproduce its correct statistical features. Unfortunately, the presence of surface tension raises serious problems in the numerical description. Presently, we perform a first important step along a careful numerical investigation. Indeed we focus our attention to test a statistical approach (the so-called phase-field model, [25]) that overcomes the problems induced by the surface tension. In this case, our main aim is to understand whether or not the phase-field approach is able to capture the physics underlying the mixing properties of immiscible fluids.

This thesis is organised as follows. We will first introduce some background information in order to make the readers familiar with the RT problem. Open questions for RT systems will be also introduced and discussed. In the following chapters our theoretical and numerical analysis are presented and discussed. Chapters 2 and 3 treat the miscible configuration in the case of two-dimensional and three-dimensional systems, respectively. The surface-tension effect is introduced in Chap. 4, where we will show that the phase-field approach is a proper technique to deal with the numerical description of instability evolution. Lastly, we will dedicate Chap. 5 to our recent results (still in progress) on the role of polymers on the mixing properties of RT. Each chapter (except for the first one) contains conclusions and possible perspectives.
Appendices A and B collect supplementary information not contained in the main text. The former is devoted to an introduction of general concepts of turbulence, the latter to the description of the implemented numerical strategy.

# Publication List

## Published papers related to the thesis

### International journals

p. 13 A. Celani, A. Mazzino and L. Vozella
Rayleigh–Taylor instability in two dimensions
*Phys. Rev. Lett.*, 96:134504 , 2006.

p. 25 G. Boffetta, A. Mazzino, S. Musacchio and L. Vozella
Kolmogorov scaling and intermittency in Rayleigh–Taylor turbulence
*submitted to Phys. Rev. Lett.*

p. 35 A. Celani, A. Mazzino, P. Muratore-Ginanneschi and L. Vozella
Phase-field model for the Rayleigh–Taylor instability of immiscible fluids
*J. Fluid Mech.*, 622:115–134, 2009.

### Conference proceedings

p. 13 A. Celani, A. Mazzino and L. Vozella
Intermittency in the miscible Rayleigh–Taylor turbulence
*Advances in Turbulence XI, Proceedings of the 11th EUROMECH European Turbulence Conference, Porto (Portugal), June 25-28, 2007*
(eds. J. M. L. M. Palma and A. Silva Lopes)
Springer Proceedings in Physics volume 117:404–406,
Heidelberg.

### In preparation

p. 53 G. Boffetta, A. Mazzino, S. Musacchio and L. Vozella
Rayleigh–Taylor instability and turbulence of viscoelastic fluids

# Chapter 1

# Introduction to the Rayleigh–Taylor instability

*"... memorie e passi d'altri ch'io calpesto ..."*
Inquieto CSI's song (1994)

Rayleigh–Taylor (RT) instability [120, 138] is a fluid-mixing mechanism occurring whenever a light fluid pushes a heavy one. The understanding of such instability, especially in the developed turbulent regime, is of primary interest in many fields of physics (e.g., in relation to supernova explosions [26, 155] and solar flares [76]) and technology (e.g., in relation to inertial confinement fusion [121]).
Despite decades of investigations, fundamental questions on turbulent RT still wait for quantitative answers. Among the most relevant questions, we recall those on the possible memory of turbulent state on the initial conditions, on the self-similar behaviour of spatial/temporal evolution.
We focus our attention on a simple configuration: a heavy fluid on top of a light fluid subjected to a gravitational acceleration. Moreover, in order to simplify the framework, we only focus on the case of small differences of densities between the two fluids. The advantage of this regime is that the numerical computations are more economical, thus allowing a more extensive exploration of the mixing properties. Physically, our calculations correspond to cases in which the density contrast is introduced by the distribution of a scalar field, for example, salt and temperature (see, e.g., [48, 89]). Usually, the density varies weakly with the scalar concentration.

This chapter provides some background information. We first formulate the problem and briefly describe the temporal evolution of RT instability (Sec. 1.1). In the following sections, the results concerning the three stages of instability evolution are shown: linear, Sec. 1.2, weakly nonlinear, Sec. 1.3, and turbulent stage in the absence (Sec. 1.4.2) and in the presence (Sec. 1.4.3) of surface tension.

## 1.1 Time evolution of instability

RT system consists of two incompressible fluids (labelled by 1 and 2) having different densities, $\rho_1$ and $\rho_2(>\rho_1)$, with the denser fluid placed above the less dense one (see Fig. 1.1). The density difference can be expressed in terms of an adimensional number called *Atwood number* $\mathcal{A}$:

$$\mathcal{A} = \frac{\rho_2 - \rho_1}{\rho_2 + \rho_1} \quad . \tag{1.1}$$

Thus, considering small differences of densities is equivalent to examining small Atwood numbers, i.e. $\mathcal{A} \ll 1$.

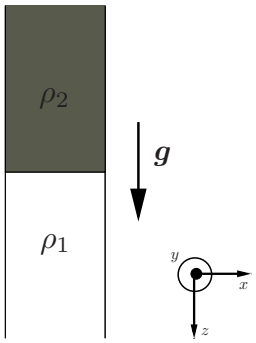


**Figure 1.1:** Initial fluid configuration corresponding to a heavier fluid of density $\rho_2$ placed above a lighter one of density $\rho_1 < \rho_2$. The gravity acceleration $\boldsymbol{g}$ is selected along the $z$ axis.

In the absence of gravity, this flow configuration is stable. In the presence of the gravitational force, the reduction of fluid potential energy drives the growth of the perturbation at the interface to form a mixing region whose width grows in time[1]. The development of this mixing can be divided into three regimes [127, 147]: linear, weakly nonlinear and turbulent stages (see sketch in Fig. 1.2). Initially, an exponential growth of an infinitesimal perturbation (corresponding to a linear stability theory) is expected. When the disturbance becomes large enough, it deforms into bubbles of light fluid and spikes of heavy fluid, i.e. coherent mushroom-like structures whose dynamics strongly depends on the Atwood number $\mathcal{A}$. The interaction among these objects defines the third flow regime. A mixing region between the fluids develops, where fluid motions become highly irregular. At sufficiently long time the irregular motions within the mixing zone become turbulent.
Numerous factors influence the development of this instability. Some of these are: density ratio [53], compressibility [87], the time dependence of the driving acceleration [53], viscosity [39], diffusivity [57], surface tension, system dimensionality [149], initial perturbation [119].

In the sequel, we focus our attention on a few of these factors: viscosity, Sec. 1.2.1, surface tension, Sec. 1.2-1.3-1.4.3, and system dimensionality, Sec. 1.4.2-1.4.3.
In the following, we refer to the case without surface tension as miscible configuration and to the case with surface tension as immiscible one.

[1] A simple experiment on RT evolution can be carried out by using a wine glass! The details can be found on the webpage `http://www.physicscentral.org/explore/pictures/cup.cfm`.

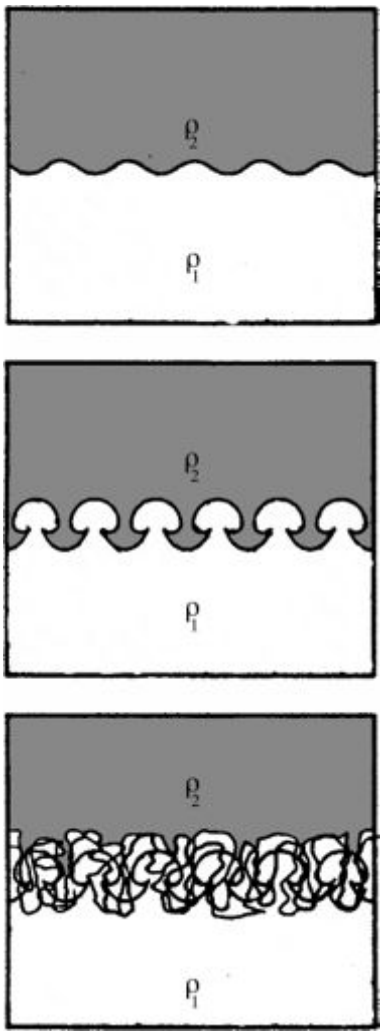


**Figure 1.2:** Sketch of the three temporal stages of a single mode initial perturbation. From top to bottom: linear, weakly nonlinear (under the hypothesis of small difference of fluid densities) and turbulent stage.

## 1.2 Linear stage: the growth rate

Under the hypothesis of small disturbances at the interface, the instability evolution can be described by a linear theory. Chandrasekhar in the Chap. X of his book [39] presents a careful analysis of this first regime. In this section we recall the mean results in the presence of surface tension.
Two infinitely extended immiscible fluids, at the equilibrium configuration described at the beginning of the previous paragraph, are considered (see Fig. 1.1). The gravity acceleration $\boldsymbol{g}$ is selected along the $z$ axis; the unperturbed interface is defined by $z = 0$. At first, let us suppose that the two fluids are inviscid.
At $t = 0$ the fluids are at rest and the interface is perturbed so as to have the form:

$$h\left(t=0;x\right) = h_0 \sin(kx). \tag{1.2}$$

with $h_0 \ll \lambda$ ($\lambda = 2\pi/k$). Thus the initial interface consists of a set of crests and troughs parallel to the $y$ axis. Using a potential-theory argument via the Bernoulli equation [39] the disturbance time evolution is given by:

$$h(t) = h_0 \cosh\left(nt\right) \tag{1.3}$$

where:

$$n = \sqrt{\mathcal{A}gk - \left(\frac{\sigma}{\rho_2+\rho_1}\right)k^3} \tag{1.4}$$

is the growth rate (see in Fig. 1.3 the black continuous line). At an early stage, the surface-tension effect is to suppress the growth of small scales. Indeed, the surface tension selects a wavenumber mode:

$$k_c = \sqrt{\mathcal{A}g(\rho_2+\rho_1)/\sigma} \quad , \tag{1.5}$$

called critical, defined by the condition of a null growth rate (i.e., $n = 0$). The higher wavenumber modes (stable modes) are suppressed and the lower wavenumber modes (unstable modes) continue to grow but with a smaller growth rate than in the miscible case ($\sigma = 0$). Fig. 1.3 confronts immiscible case and miscible one. The surface tension can thus be able to keep the system in equilibrium, provided the density contrast is not large.

### 1.2.1 Bounds for the perturbation growth rate in the presence of viscosity

The effect of viscosity is to reduce the perturbation growth rate. However it does not remove the instabilities. Analytically, it is more difficult to consider the effect of viscosity with respect to that of the surface tension (see Eq. (115) on page 443 of [39]). Nonetheless, it is possible to determine a lower and an upper bound to the growth rate $n_\nu$. These bounds are the solutions of the following equations [99]:

$$n_\nu^4 + 2\nu k^2 n_\nu^3 + (\nu^2 k^3 - \frac{n^2}{k})kn_\nu^2 - (\nu^2 k^3 + \frac{n^2}{k})\nu k^3 n_\nu - (\nu^4 k^6 - \frac{n^4}{k^2})k^3 = 0 \tag{1.6}$$

$$n_\nu^2 + 2\nu k^2 n_\nu - n^2 = 0 \tag{1.7}$$

where $\nu$ is the viscosity and $n$ is the growth-rate in the inviscid case (see Eq. (1.3)). The solution of Eq. (1.7) is:

$$n_\nu = -k^2\nu + \sqrt{k^4\nu^2 + n^2} \quad , \tag{1.8}$$

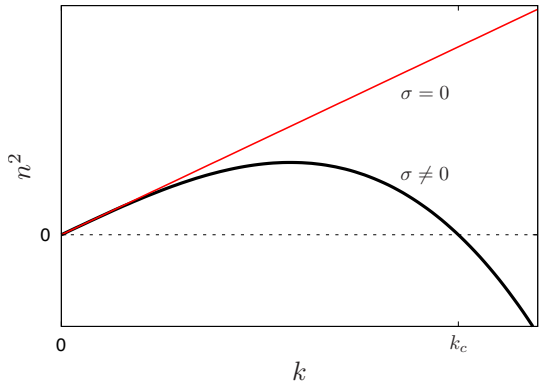


**Figure 1.3:** The square growth-rate $n^2$ (see Eq. (1.3)). The cases without (red continuous line) and with (black continuous line) surface tension are compared.

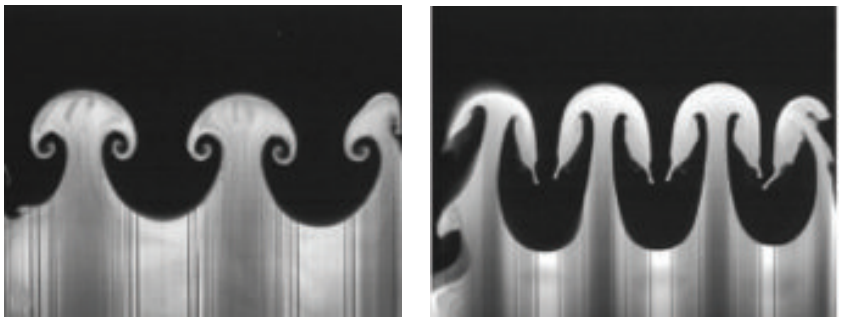

**(a)** miscible configuration, $\mathcal{A} \ll 1$ **(b)** immiscible configuration, $\mathcal{A} \ll 1$

**Figure 1.4:** Two-color images of bubbles/spikes from the experiments [141]. Different structures are observed in **(a)** miscible and **(b)** immiscible configurations, reflecting the surface-tension effects on the dynamics at small scales.

while only a numerical solution is available for Eq. (1.6).

## 1.3 Weakly nonlinear stage: models for the terminal bubble/ spike velocities

Substantial deviations from the linear theory are observed when the perturbation amplitude reaches a size of the order of $0.1\,\lambda$ - $0.4\,\lambda$ [127].
In that case the disturbance grows nonlinearly and the interface starts to deform. Indeed, at least for finite values of $\mathcal{A}$, the interface can be divided into spikes corresponding to the regions where the heavier fluid penetrates into the lighter one, and bubbles associated to those regions where lighter fluid rises in the heavier one. The roll-up of vortices produces a mushroom-type shape for bubbles and spikes (see, for instance, Fig. 1.4). When the fluid densities are similar (corresponding to our case $\mathcal{A} \ll 1$) spikes and bubbles coincide and

approach a constant and equal velocity. On the contrary, as $\mathcal{A}$ approaches $1$, the spikes become narrow and approach free fall [1, 150, 152]. In both cases, the exponential growth of the perturbation amplitude characterising the linear phase of the evolution is replaced by a linear-in-time behaviour [141]. Two models are available to describe this stage: the drag-buoyancy model [1] and the "Layzer model" [65, 90, 148]. The former model describes bubble and spike motion by balancing the buoyancy and drag forces and it assumes that these velocities reach constant values for sufficiently long times. The latter model uses an expansion of the perturbation amplitudes and conservation equations near the tip of bubbles and spikes. This approach has been first applied to the fluid-vacuum interface ($\mathcal{A} = 1$) [90] and then extended to arbitrary Atwood numbers [65] to include the surface-tension contribution [148]. According to the latter study, in our case (immiscible fluids and small Atwood number) one expects that the terminal bubble and spike velocity can be obtained from the results in [148]:

$$U(t \to \infty) = \sqrt{\frac{2}{3}\mathcal{A}\frac{g}{k} - \frac{2}{9}\frac{\sigma}{\rho_2 + \rho_1}k} \quad . \tag{1.9}$$

## 1.4 Turbulent stage

At a sufficiently long time a mixing layer of width $L(t)$ sets in, giving rise to a fully developed, nonstationary, turbulent regime. The motion is characterised by the coalescence of structures at smaller and smaller scales. A principal focus of experimental and theoretical studies has been the temporal behaviour of the mixing layer with scarce attention to the investigation of the statistical properties of small-scale fluctuations. Along this latter direction, the first consistent phenomenological theories has been proposed only recently by Chertkov and coworkers [41, 43] and by Poujade [114]. These theories have however some intrinsic limitations. Indeed, their results constitute a set of mean-field (i.e., dimensional) predictions, which needs to be verified against numerics and/or experiments in order to understand the role of fluctuations and more specifically their affects on intermittency and anomalous scaling (see App. A).
In this Section, we first discuss the time evolution of the mixing layer. Afterwards, we briefly recall the main predictions of the phenomenological theory both in the miscible configuration [41] and in the immiscible one [43]. Concerning the miscible configuration in three-dimensions we also mention the alternative phenomenological theory formulated in [114].

### 1.4.1 Measuring of the time behaviour of mixing-layer width

At sufficiently larger times, the extent of the mixing region has historically been assumed to behaves as [147]:

$$L(t) = \alpha \mathcal{A} g t^2 \quad , \tag{1.10}$$

where $\alpha$ is a dimensionless coefficient. This similarity solution results from dimensional analysis if the following conditions are met: any memory of the initial conditions is lost, there are no boundary effects, and viscosity and diffusivity do not influence the large-scale motion[2]. Physically, this quadratic law has a simple meaning in terms of gravitational fall and rise of

[2] Under these hypotheses, $gt^2$ is the only length scale of importance.

thermal plumes (i.e., the well-organised structures of hot rising fluid and cold descending fluid). Indeed, as viscous forces are negligible compared with inertial forces, thermal plumes accelerate as if they were free particles subjected to gravity.
If, on the one hand, there is a general consensus on the foregoing time behaviour, on the other hand, the value of the prefactor and its possible universality is a much debated issue. This prefactor is a focus of almost any paper written on the subject of RT instability. Experimental and computational estimates for $\alpha$ span a fairly wide range, from $\alpha = 0.02$ to values one order of magnitude higher (see, for instance, [53, 54]). A slight decrease in time and a dependence on the Atwood number have been also observed [45, 54]. Moreover, there is not agreement between simulations and experiments. In [54, 119] this difference is attributed to long-wavelength modes in the experiments, which are generally not present in the simulations.
Recently, the problem concerning the determination of $\alpha$ value has been related to the estimation of the time behaviour of the mixing layer. Indeed, from the relation (1.10), numerous attempts to measure $\alpha$ have been made by plotting $L$ versus $\mathcal{A}gt^2$ thus obtaining $\alpha$ as a quadratic best fit. In [46,124] the authors realised that this method is not completely correct. Indeed, in the aforementioned studies the authors, using completely different approaches, derived the following governing equation for $L$:

$$\dot{L}^2 = 4\alpha\mathcal{A}gL(t) \quad . \tag{1.11}$$

For constant $\alpha$, $\mathcal{A}$ and $g$, its solution is (taking the positive root as the only physically meaningful):

$$L(t) = \alpha\mathcal{A}gt^2 + 2(\alpha\mathcal{A}L_0)^{1/2}t + L_0 \tag{1.12}$$

where $L_0$ is an initial-condition memory. Dividing the last equation by $\mathcal{A}gt^2$ one has:

$$\alpha = \frac{L}{\mathcal{A}gt^2} - \left(\frac{\alpha L_0}{\mathcal{A}g}\right)^2 \frac{2}{t} - \frac{L_0}{\mathcal{A}gt^2} \quad . \tag{1.13}$$

Thus the *naïve* compensation of $L(t)$ with $\mathcal{A}gt^2$ does not give a precise estimation of the coefficient $\alpha$ because of the presence of subleading terms which decay slowly in time.

**Definition 1** (**Mixing region width**). *The mixing-layer width can be defined in terms of the so-called volume fraction, which represents the probability that a given fluid occupies a point at a given time (see, e.g., [45, 147]). The volume fraction of heavy fluid is defined as:*

$$\mathcal{X}(z,t) = \frac{\langle\rho\rangle_z(z,t) - \rho_1}{\rho_2 - \rho_1} \tag{1.14}$$

*where brackets $\langle\cdots\rangle_z$ denote the spatial average in the horizontal planes. At every time, the mixing width is defined as the range in the gravitational direction for which $\chi \leq \mathcal{X} \leq 1-\chi$, where $\chi$ is a volume-fraction threshold. We selected $\chi = 0.02$.*

### 1.4.2 Miscible configuration

Let us start by introducing the equations of motion of RT system. We first concentrate on a miscible configuration in the case of small density differences between fluids. Here,

small is relative to the mean density $(\rho_1 + \rho_2)/2$. In the limit of small Atwood numbers (i.e., $\mathcal{A} \to 0$ and yet $\mathcal{A}g$ a finite constant), the equations of motion can be written in the so-called Boussinesq approximation (see, e.g., [86]). There is a variety of ways of achieving a small density jump across the horizontal interface: one may choose, for instance, a single fluid into which a contaminant is added, which changes the fluid density slightly. Such small vertical density variation depends linearly on temperature. Thus, in this formulation, the density jump across the interface is replaced by a temperature difference: colder fluid on top of warmer fluid. Therefore the equations for the miscible, incompressible, RT instability in the Boussinesq limit are the incompressible ($\boldsymbol{\partial} \cdot \boldsymbol{v} = 0$) Navier–Stokes equation (see Sec. A.1 for its description) coupled to an advection-diffusion equation for the temperature field:

$$\partial_t \boldsymbol{v} + \boldsymbol{v} \cdot \boldsymbol{\partial} \boldsymbol{v} = -\boldsymbol{\partial} p' + \nu \partial^2 \boldsymbol{v} + \beta \boldsymbol{g}(T - T_o) \tag{1.15}$$

$$\boldsymbol{\partial} \cdot \boldsymbol{v} = 0 \tag{1.16}$$

$$\partial_t T + \boldsymbol{v} \cdot \boldsymbol{\partial} T = \kappa \partial^2 T \quad , \tag{1.17}$$

$T$ being the temperature, $\boldsymbol{v}$ the velocity, $p' = p + \rho_o U_g$ where $p$ is the pressure field and $U_g$ is the gravitational potential, $\nu$ the viscosity, $\beta$ the thermal-expansion coefficient, $\boldsymbol{g}$ the gravitational acceleration along $z$ axis, $T_o$ the temperature mean value and $\kappa$ molecular diffusivity. The coupling term $\beta \boldsymbol{g}(T - T_o)$ is the so-called buoyancy which expresses the Archimedes principle.
From the balance between the buoyancy term on the right-hand side of Eq. (1.15) and the temporal-derivative term on the left-hand side, the temporal behaviour of $L(t)$ is obtained again:

$$\frac{\delta_L v}{t} \sim \frac{L(t)}{t^2} \sim \beta g \Theta \qquad \Rightarrow \qquad L(t) \sim \beta g \Theta t^2, \tag{1.18}$$

where $\delta_L v$ is the typical velocity at the scale $L$, $\Theta$ is the initial jump of temperature between the fluids and $\beta\Theta/2$ is the Atwood number[3]. The statistics of velocity and temperature fluctuations inside the mixing zone, at small scales $r \ll L$, is the realm of application of the phenomenological theory of Ref. [41]. The cornerstone of this theory is the quasiequilibrium picture where small scales adjust adiabatically as temperature and velocity fluctuations decay in time due to the increasing growth of the mixing layer. Adiabaticity means that the turbulent small-scale fluctuations rapidly adjust themselves to the large-scale change. At the small scales $r \ll L(t)$ the author of [41] suggests different behaviours depending on space dimensionality. Depending on the space dimension (two or three), temperature and therefore buoyancy are expected to have different role.

#### 1.4.2.1 Three-dimensional configuration

A generalised Kolmogorov picture for the velocity (see, for an introduction to turbulence, App. A) and an Obukhov–Corrsin scenario (see App. A) for the temperature are predicted. Generally, in a turbulent system, the energy is injected at large scales (e.g., the size of the

[3]Under the Boussinesq approximation, the relation between the temperature field and the density field is linear [86]:

$$\rho = \rho_o - \beta \rho_o (T - T_o) \quad ,$$

where $\rho_o$ is the mean density.

bath in which the fluid moves); it propagates through smaller and smaller scales and is dissipated at the smallest scales, at which the dissipation dominates over the advection which controls the energy distribution towards smaller scales. The intermediate domain of scales is called the inertial range. The Kolmogorov–Obukhov–Corrsin scenario of steady turbulence are based on the assumption that in the inertial range the kinetic-energy and the temperature variance flow towards smaller scales at a constant flux.
Assuming adiabaticity, kinetic-energy flux ($\epsilon_v$) and temperature-variance flux ($\epsilon_T$) immediately follow from simple dimensional considerations: $\epsilon_v \sim (\delta_r v)^3/r \sim (\delta_L v)^3/L$ and $\epsilon_T \sim (\delta_r T)^2 \delta_r v/r \sim \Theta^2 \delta_L v/L$. From relation (1.18):

$$\delta_r v \sim \delta_L v(t) \left(\frac{r}{L(t)}\right)^{1/3} \sim (\beta g \Theta)^{2/3} r^{1/3} t^{1/3} \tag{1.19}$$

$$\delta_r T \sim \Theta \left(\frac{r}{L(t)}\right)^{1/3} \sim \Theta^{2/3} (\beta g)^{-1/3} r^{1/3} t^{-2/3} \quad . \tag{1.20}$$

The temperature behaves as a passive scalar (see, Sec. A.4.1 in appendix) advected by the velocity field: the effect of buoyancy on turbulence becomes irrelevant at small scales. Indeed, from the above relations, one can verify that the distortion of the kinetic energy balance due to the buoyancy term is negligible in comparison with the flux of energy, i.e.:

$$(\delta_r v)^3 \gg \beta g \delta_r T \delta_r v \quad . \tag{1.21}$$

Finally, by matching the inertial and the viscous terms in Eq. (1.15) the time behaviour of the viscous scale is easily derived[4]:

$$\eta(t) \sim \left(\frac{\nu}{\delta_L v}\right)^{3/4} L(t)^{1/4} \sim (\beta g \Theta)^{-1/2} \nu^{3/4} t^{-1/4} \quad . \tag{1.22}$$

Phenomenologically, there is no complete agreement on the Kolmogorov–Obukhov–Corrsin mechanism, just described. Indeed an alternative interpretation of numerical and experimental data has been recently proposed by Poujade in [114]. In the Chertkov predictions, the buoyancy, although fundamental at large scale, becomes irrelevant at small scales, as expressed in (1.21). On the contrary, in the Poujade theory, a balance mechanism between buoyancy and energy transfer is expected not only at large scales but also at smaller ones.

#### 1.4.2.2 Two-dimensional configuration

Two-dimensional turbulence is expected to be different form the three-dimensional one (in Sec A.3 an introduction to the phenomenology of two-dimensional turbulence is presented). This expectation is based on the following standard phenomenological consideration: if injection and dissipation are not taken into account, the velocity field dynamics is characterised by two conserved quantities, i.e. in addition to the kinetic energy, the enstrophy (defined as $|\boldsymbol{\partial} \times \boldsymbol{v}|^2$) is also conserved. From the assumption that the temperature behaves as a

[4] In [26, 44] the numerical results are consistent with Kolmogorov's "5/3"- spectrum described in (1.19)-(1.20). Moreover the authors confirm the time behaviour of the viscous scale $\eta(t)$.

passive scalar, the analysis of two-dimensional Navier–Stokes turbulence leads to two scenarios. While the temperature variance flows to small scales at a constant flux, the velocity field either undergoes an inverse cascade, with an inertial range characterised by a backward scale-independent energy flux or develops a direct enstrophy cascade. Both possibilities actually turn out to be inconsistent [41]. This apparent deadlock can be broken by rejecting the initial assumption that temperature behaves as a passively transported quantity at all scales. Indeed Chertkov [41] suggests that buoyancy and nonlinear terms in Eq. (1.15) must be in equilibrium. This is the essence of the Bolgiano–Obukhov regime (see for details, Sec. A.4.2 in appendix). Under the assumption that temperature fluctuations cascade to small scales at a constant rate, one arrives [41] to the following scaling relations:

$$\delta_r v \sim \delta_L v \left(\frac{r}{L(t)}\right)^{3/5} \sim (\beta g \Theta)^{2/5} r^{3/5} t^{-1/5} \tag{1.23}$$

$$\delta_r T \sim \Theta \left(\frac{r}{L(t)}\right)^{1/5} \sim (\beta g)^{-1/5} \Theta^{4/5} r^{1/5} t^{-2/5} \quad , \tag{1.24}$$

where the spatial power law is exactly the Bolgiano scaling. Moreover, one defines the viscous scale, $\eta(t)$, as the scale at which both the buoyancy and the nonlinear advection terms from Eq. (1.15) become of the order of the viscous term. From relations (1.23) and $(\delta_\eta v)\eta \sim \nu$ one easily obtains:

$$\eta(t) \sim \left(\frac{\nu}{\delta_L v}\right)^{5/8} L(t)^{3/8} \sim (\beta g \Theta)^{-1/4} \nu^{5/8} t^{1/8} \quad . \tag{1.25}$$

In contrast with the three-dimensional expression (1.22), the preceding relation shows that the two-dimensional viscous scale grows with time. Note also that the quadratic growth of $L(t)$ is still rapid enough to guarantee an increase of the Bolgiano-Obukhov range width.

### 1.4.3 Immiscible configuration

Let us introduce the effect played by surface tension in RT turbulence. In [43] a phenomenological theory is proposed to study the mixing of immiscible fluids (e.g., water and oil): the turbulence regime is characterised by the interplay between hydrodynamic and interface degrees of freedom. The size of the turbulent mixing zone grows according to (1.18). Hydrodynamic motions at scales $\sim L$ continue to be driven by buoyancy. At smaller scales the dynamics is accompanied by mutual penetration of the fluids, which is initiated by the injection of pure fluid jets into the mixing zone. The collision of jets of different fluids produces complex interfacial structures. Drops of both types are shed from the interface: the result is the creation of an emulsion-like state (see Fig. 1.5). Surface tension becomes relevant at the scale typical of the drop size, $\ell$, leading to the interface breakdown into drops. By considering a typical drop size larger than the viscous scale, $\ell \gg \eta$, the size $\ell$ can be estimated as the scale where the kinetic-energy density of the fluids and the interfacial-energy density are of the same order of magnitude:

$$\rho_o (\delta_\ell v)^2 \sim \sigma/\ell \tag{1.26}$$

where $\rho_o = (\rho_1 + \rho_2)/2$. At this scale, in [43] an interplay between the hydrodynamics and the surface-tension degrees of freedom is suggested.

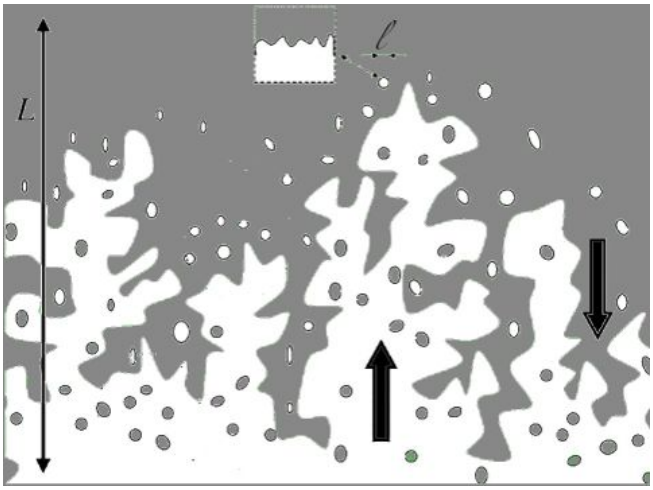


**Figure 1.5:** Schematic view of a density distribution snapshot in a turbulent regime. Different densities are marked as gray for heavier and white for lighter fluid. The black arrows indicate the mean direction of two single-fluid phases. The inset on the top illustrates that a drop surface is populated by capillary waves.

The time behaviour of $\ell$ depends on the dimensionality of the system.
In three dimensions, from relation (1.19), one easily gets:

$$\ell \sim \left(\frac{\sigma^3}{\mathcal{A}^4 g^4 \rho_o^3}\right)^{1/5} t^{-2/5} \quad . \tag{1.27}$$

Dynamically, the permanent decrease in the typical drop size $\ell$ is realised through the creation of new drops as well as through the breakup of already existing drops into smaller ones. In [43] the authors claim the existence of a Kolmogorov in-volume cascade between the integral scale $L(t)$ and the time-dependent scale $\ell$. As far as the dynamics on the drop surface is concerned, a turbulent cascade of capillary waves is expected to take place (for the capillary-wave dynamics see, for instance, [59, 116, 117, 153]). The capillary-wave dynamics opens an additional channel for the energy transfer to small scales. The energy flux, coming from the scale $L(t)$, splits in two parts at the scale $\ell$: a part of the energy cascades further (towards the viscous scale $\eta$) in the bulk (the mechanism is equivalent to that for single phase turbulence) while the remainder feeds capillary fluctuations, giving rise to the capillary-wave energy cascade at the surfaces of the drops.

In two dimensions, in analogy with the miscible case considered in the previous section, one expects that the Bolgiano-Obukhov regime, rather than the Kolmogorov picture, is realised. Therefore, by using (1.23), one obtains:

$$\ell \sim \left(\frac{\sigma^5}{\rho_o^5 \mathcal{A}^4 g^4}\right)^{1/11} t^{2/11} \quad . \tag{1.28}$$

Unlike the three dimensional case, the capillary scale $\ell$ increases in time. Also in the immiscible case, two-dimensional RT and three-dimensional RT turbulence radically differ.

# Chapter 2

# Miscible two-dimensional configuration

*"I call our world Flatland, not because we call it so, but to make its nature clearer to you, my happy readers, who are privileged to live in Space..."*
Flatland by Edwin A. Abbott (1884)

The final stage of RT instability leads to the so-called RT turbulence. Despite the long history of RT turbulence, a consistent phenomenological theory has been presented only very recently by Chertkov [41] (and briefly recalled in Sec. 1.4.2). We present the first attempt to compare numerical results with such phenomenological theory in two dimensions. By means of Direct Numerical Simulations, we confirm the spatiotemporal prediction of the theory and explore the breakdown of the phenomenological description due to intermittency effects. We show that the small-scale statistics of velocity and temperature follow the Bolgiano-Obukhov scaling. At the level of global observables, we show that the time-dependent Nusselt and Reynolds numbers scale as the square root of the Rayleigh number. These results point to the conclusion that RT turbulence, thanks to the absence of boundaries, provides a natural physical realization of the Kraichnan scaling regime, hitherto associated with the elusive "ultimate state of thermal convection" [82].

In Sec 2.2 we first introduce the numerical strategy used in the investigations described in the present thesis. Afterwards we formulate the problem and outline the numerical setup. The following sections are devoted to the description of numerical results: concerning the scales typical of the mixing-layer width, Sec. 2.3, the small scales, Sec. 2.4, and global-quantities scaling, Sec. 2.5. Sec. 2.6 provides the conclusions by summarising the main results.

## 2.1 Numerical strategy: an introduction

Our research activity is devoted to investigate the evolution of RT instability by means of numerical simulations. The numerical strategy used is the so-called Direct Numerical Simulation (DNS). Generally, a DNS consists in solving equations ruling the fluid evolutions, resolving all active scales of motion, with the appropriate initial and boundary conditions. Each simulation produces a single realization of the flow.

Moreover, in order to efficiently and accurately solve the equations ruling the fluid evolution a pseudospectral method is used [29]. The main advantage of the method consists on the fact that the derivatives are calculated in Fourier space (then becoming free from truncation errors typical of finite differences to calculate derivatives) and the products in physical space (thus avoiding to compute convolutions in Fourier space) Accordingly, periodic boundary conditions have to be assumed along the two or three directions. In the investigation of RT instability, for the horizontal directions this is a natural choice [26, 92] while along the gravitational one (the direction of instability development), it deserves some comments which will be given in the sequel.
Finally, the time evolution is implemented by a standard second-order Runge–Kutta scheme. More details on the numerical scheme are given in App. B.

## 2.2 Formulation of the problem

The system consists of two miscible, incompressible fluids (labelled by 1 and 2) having different temperatures, $T_1$ and $T_2$ ($> T_1$) in the gravitational field $\boldsymbol{g}$, selected along the $z$ axis. We only focus on the low-Atwood-number regime. At the initial time the system is at rest with the colder fluid placed above the hotter one. This amounts to assuming a step function for the initial temperature profile:

$$\boldsymbol{v} = \boldsymbol{0} \tag{2.1}$$

$$T(0,z) = -\,\mathrm{sign}(z)\,\frac{\Theta}{2} \tag{2.2}$$

with $\boldsymbol{v}$ the velocity field and $\Theta$ the initial jump of temperature. The value of $\mathcal{A}g = \beta g \Theta/2$ is equal to 0.15 (model units).
When a disturbance is imposed on the interface separating the fluids, the fluid evolution is described by the Navier–Stokes and the advection-diffusion equations (1.15)-(1.16)-(1.17) under the Boussinesq approximation.

### 2.2.1 Numerical setting and statistics

In the present study we consider the initial perturbations imposed to the interface as varying along one of the horizontal directions, say the $x$ axis, and invariant along the other horizontal direction, say the $y$ axis. The perturbation is thus intimately two-dimensional, a fact that allows us to solve the original Navier–Stokes equations coupled to the advection-diffusion equation for the temperature, Eqs. (1.15)-(1.16)-(1.17), in two dimensions. For a two-dimensional flow it is convenient to introduce the vorticity field $\omega$ [$\omega = (\boldsymbol{\partial} \times \boldsymbol{v})_y$] (in this way pressure cancels out from the equations) and to study the equations:

$$\partial_t \omega + \boldsymbol{v}\cdot\boldsymbol{\partial}\omega = \nu\partial^2\omega + \beta\boldsymbol{\partial}T \times \boldsymbol{g} \tag{2.3}$$

$$\partial_t T + \boldsymbol{v}\cdot\boldsymbol{\partial}T = \kappa\partial^2 T \quad . \tag{2.4}$$

The integration of both equations is performed on a doubly periodic domain of horizontal-vertical aspect ratio $L_x : L_z = 1 : 4$. The resolution is $128 \times 4096$ collocation points. Different aspect ratios (up to $1:8$) and resolutions (up to $128 \times 8192$) did not show substantial modifications on the results. As a testground for the code, we investigate the linear

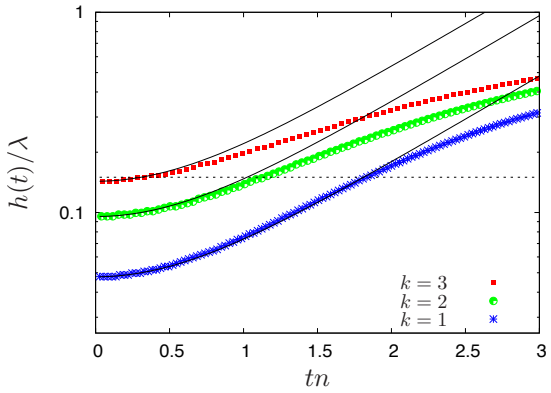


**Figure 2.1:** Time behaviour of the amplitude perturbation, $h(t)$ for three different perturbations with fixed wave number: $k = 1$ (blue symbols), $k = 2$ (green symbols) and $k = 3$ (red symbols) and with the same initial amplitude $h_0/L_z = 0.048$. $n$ is the linear growth rate (see Eq. 1.4 where $\sigma = 0$). The black continuous lines correspond to the linear-theory prediction (see Sec. 1.2). When $h(t)/\lambda \sim 0.15$ (indicated by the dashed line) the nonlinear effects start to enter into play giving rise to corrections to the linear behaviour (see Sec. 1.3). The aspect ratio is 1:2 and the resolution $128 \times 2048$.

and weakly nonlinear phases. The results accurately verify the predictions (see Secs. 1.2-1.3). In Fig. 2.1 the linear-stage results are summarised.

Concerning the study of the turbulent regime, given that the system is intrinsically non-stationary, the averages to compute statistical observables are performed over different realisations (about $40$ in this study[1]). The latter are produced by generating initial interfaces with sinusoidal waves of equal amplitude and random phases [45]. Each realisation is advanced in time until the mixing layer invades the $75\%$ of the domain.
The panels on page 16 offer one realisation example. The time evolution of the temperature field is shown.

Large-scale structures (i.e., the thermal plumes) identify the direction of gravity. The gravity, by selecting one direction, breaks isotropy at least at large scales. Our question is now on what happens at small scales. The basic phenomenology of turbulence predicts a recovery of isotropy at sufficiently small scales of the turbulent flows. Nevertheless, both recent experimental works and theoretical analysis suggested that the actual rate of recovery is much slower than the one predicted by simple dimensional analysis (see the review [16] and references therein). In order to avoid spurious anisotropy effects on the results, and thus to be able to compare numerical results with the phenomenological predictions, for each statistical indicator (e.g., structure functions) we have extracted the isotropic contribution to the scaling by averaging, for a given separation, over all possible directions. This is the

[1]The chosen number of realisations results from the necessity of conciliating three demanding computational requirements: high resolution, long time integration, large statistics. The computational effort for the present set of simulations has been of thousands of CPU hours. A posteriori, the degree of statistical convergence can be appreciated in Fig. 2.3, where the average of $\alpha$, and its value in some individual realisations, is presented. From these and other similar checks, not shown here, this number of realisations is estimated to be sufficient to draw robust quantitative conclusions.

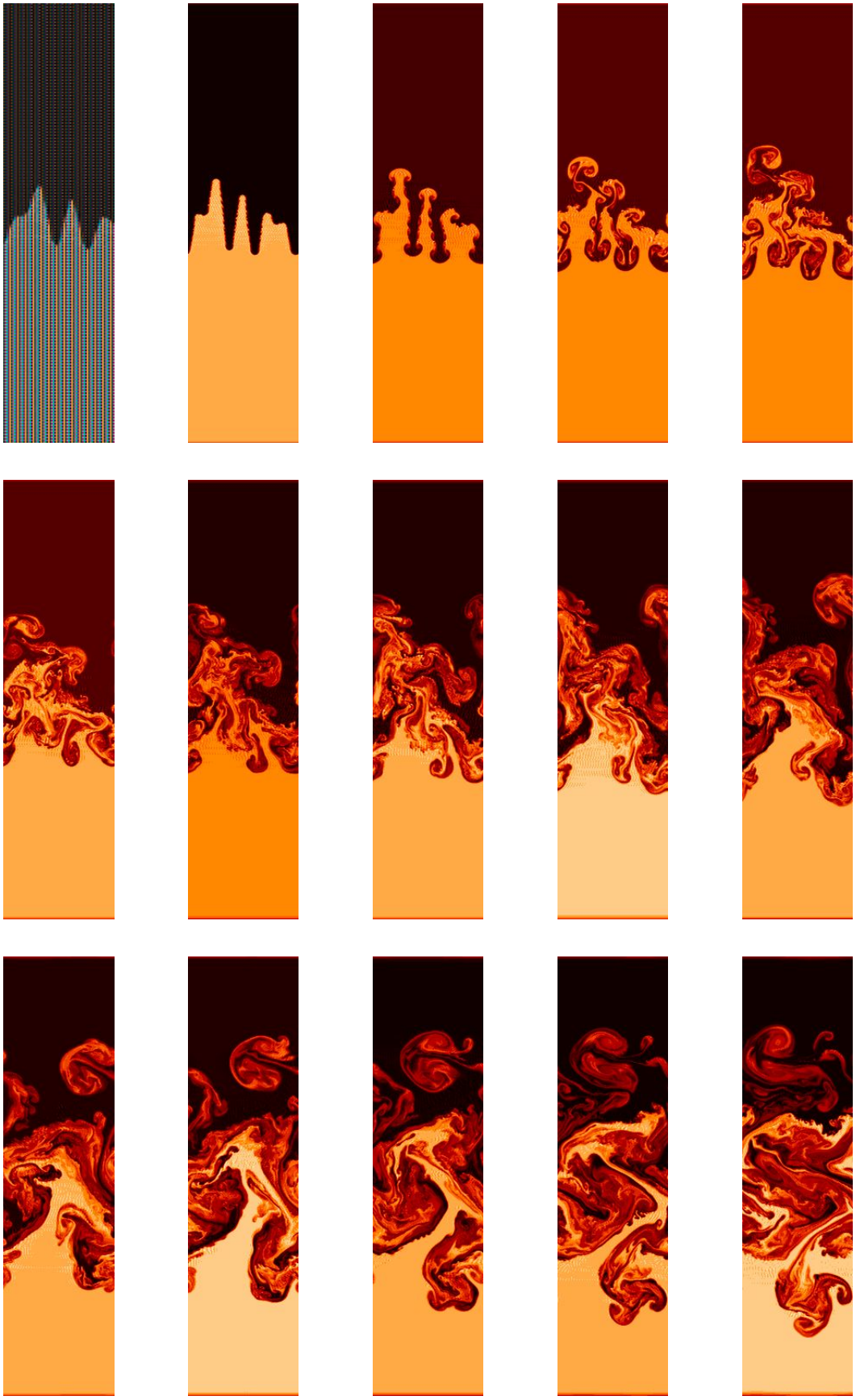

**Table 2.1:** Time evolution of miscible Rayleigh–Taylor instability. Dark (yellow) areas identify cold (hot) regions.

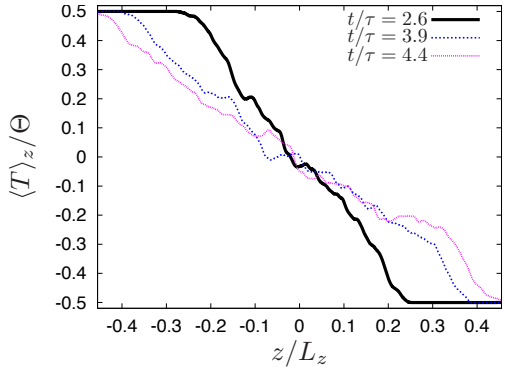


**Figure 2.2:** The horizontally ensemble-averaged temperature field at $t/\tau = 2.6$, $t/\tau = 3.9$ and $t/\tau = 4.4$. The dimensional group $\tau \equiv [L_z/(\mathcal{A}g)]^{1/2}$ is a characteristic time scale of the flow [48]. Note the almost linear behaviour of $\langle T \rangle_z$ in the mixed layer.

essence of the $SO(2)$ decomposition to disentangle the effects of anisotropy on the scaling behaviour [16].

In the following we denote by $\langle \cdot \rangle_z$ the average over the $z$ plane and by $\langle \cdot \rangle$ the average over the whole mixing region.

## 2.3 Large-scale statistics

The horizontally ensemble-averaged temperature field at three different instants is shown in Fig. 2.2. It is worth observing the almost linear behaviour of the averaged temperature within the mixing layer. This is a first clue suggesting a possible relationship between RT turbulence and the two-dimensional Boussinesq driven convection studied in Refs. [34, 35]. In this particular instance of 2D thermal convection the fluid is heated from below and the turbulent fluctuations are driven by an external, fixed, linearly-behaving-with-the-elevation, temperature profile. The fluid evolution is modelled by the same set of equations as the RT problem, with constant boundary conditions (i.e. the width of turbulent motions is constant in time), instead of the initial conditions (2.1) describing the RT setting. regime clearly appears from the data [35]. As a consequence, we argue that two-dimensional RT turbulence may to correspond to the case driven by a linear temperature profile with a mean gradient that adiabatically decreases in time as $\Theta/L \sim t^{-2}$.
The mixing-layer growth rate is shown in Fig. 2.3 in terms of the growth-rate parameter $\alpha$. The compensation of $L$ with $\mathcal{A}gt^2$ (black filled circles) and the compensation of $\dot{L}$ with $4\mathcal{A}gL$ (red filled circles) are compared (for details see Sec. 1.4.1). The former method suffers from the $\sim t^{-1}$ dependence of the missing terms (as discussed in Sec. 1.4.1), whereas the latter method yields a nearly constant value $\alpha \simeq 0.013$ from $t/\tau \simeq 2.6$. The two measures do not match and the $L/(\mathcal{A}gt^2)$ compensation presents a larger value than the $\dot{L}/(4\mathcal{A}gL)$ one, as observed in the study of the three-dimensional RT problem [26].

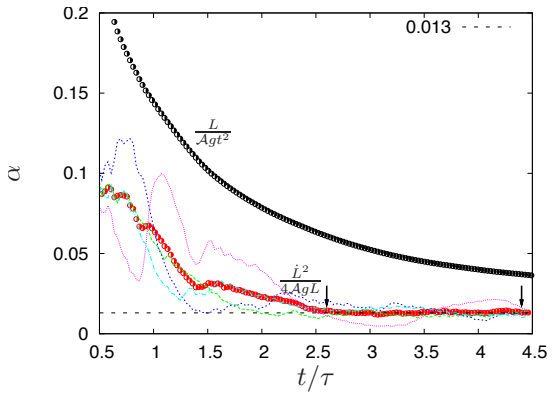


**Figure 2.3:** The time evolution of the layer-growth parameter $\alpha$. Two different compensations are compared: $L(t)/\mathcal{A}gt^2$ (black filled circles) and $\dot{L(t)}/(4\mathcal{A}gL(t))$ (red filled circles). The mixing-layer width $L(t)$ is defined as the distance between the $z$ levels at which $\mathcal{X} = 2\%$ and $98\%$, respectively (see the operational definition on page 7). The black and red filled circles represent the ensemble-averaged quantities. The thin lines refer to some individual realisations, thus giving an indication of the level of fluctuations. Two arrows, corresponding to $t/\tau = 2.6$ and $t/\tau = 4.4$, bound the time range in which the turbulent investigation is performed.

## 2.4 Small-scale statistics

In order to quantitatively assess the presence of the Bolgiano regime for RT turbulence, let us focus on the scaling behaviour of fluxes and structure functions.
The behaviour of kinetic-energy flux, $\epsilon_v = \langle(\delta_r v)^3/r\rangle$, and temperature-variance flux, $\epsilon_T = \langle(\delta_r T)^2\delta_r v/r\rangle$, are shown in Fig. 2.4. Dimensional expectations following from the Bolgiano–

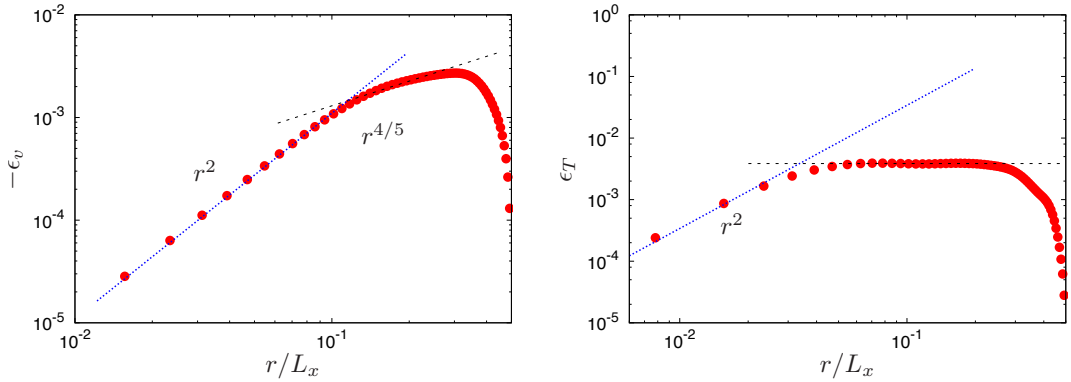


**(a)** kinetic-energy flux **(b)** temperature-variance flux

**Figure 2.4:** The scaling behaviour of **(a)** $-\epsilon_v = -\langle(\delta_r v)^3/r\rangle$ and **(b)** $\epsilon_T = \langle(\delta_r T)^2(\delta_r v)/r\rangle$. These ones are compatible with the dimensional prediction à la Bolgiano–Obukhov. Note the negative sign of $\epsilon_v$ reflecting the fact that the energy is flowing from small to large scales (even if at a non-constant rate) [136]. In both figures the scaling $r^2$ corresponding to the dissipative scales is shown (blue short-dashed line).

Obukhov relations (1.24)-(1.23) are $\epsilon_v \sim r^{4/5}$ and $\epsilon_T \sim \text{const.}$. Both of them are compatible

with the data shown in Fig. 2.4. The dependence on the scale of $\epsilon_v \sim r^{4/5}$ excludes the presence of both inverse cascade of energy and direct cascade of enstrophy.
The scenario à la Bolgiano is confirmed by looking at the structure functions (i.e., the moments of field differences). For both velocity and temperature differences, they are shown in Fig. 2.5. On one hand, second-order functions follow the dimensional predictions (1.24)

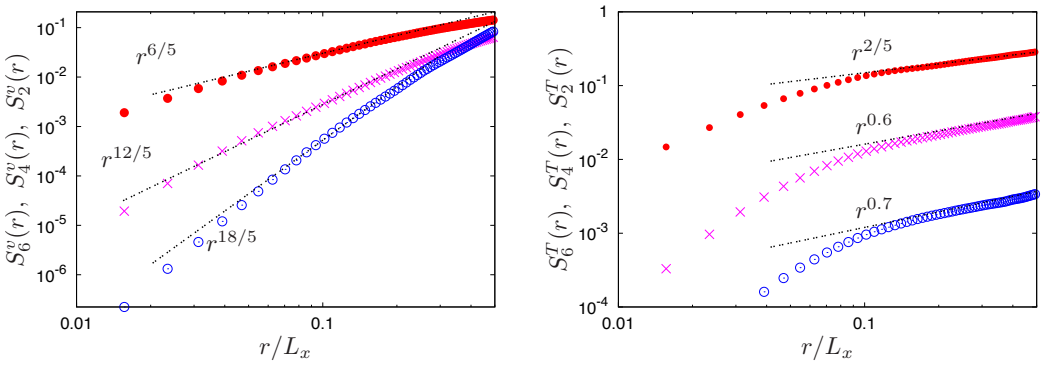


**(a)** moments of longitudinal velocity differences **(b)** moments of temperature differences

**Figure 2.5:** The moments of longitudinal velocity differences **(a)** and temperature differences **(b)**. The isotropic contribution to the statistics is considered by averaging over all the directions of separations $\mathbf{r}$. In **(a)** the dashed lines are the dimensional predictions, $S_p^v \sim r^{3n/5}$ [41]. In **(b)**, for $p = 2$, the dashed line is the Bolgiano–Obukhov dimensional prediction: $S_2^T \sim r^{2/5}$ [41]. For $p = 4$ and 6, the scaling exponents are anomalous, and their values are compatible with those of the two-dimensional turbulent convection model of Refs. [34, 35] (dashed lines). The moments are averaged over different $L$'s ranging from $L/L_z = 0.4$ to $L/L_z = 0.6$ (see Fig. 2.7).

- (1.23). On the other hand, moments of order 4 and 6 display non-dimensional corrections for the temperature, e.g., deviations from (1.24), while this is not the case for the velocity. The non dimensional corrections, the so-called intermittency (see App. A), is related to a breakdown of scale invariance. The statistical property of the temperature, which displays intermittency corrections, at a certain scale cannot be obtained by a simple rescaling of the statistics at another scale. The velocity, which do not present intermittency corrections, shows a close-to-Gaussian probability density function (PDF) for inertial-range increments (see Fig. 2.6a) and once the PDFs are rescaled by the Bolgiano–Obukhov prediction, they collapse one into another as shown in Fig. 2.6b. The slopes of Fig. 2.5b associated to $S_4^T$ and $S_6^T$ are relative to the scaling exponents found in Ref. [35]. This is a further quantitative evidence in favor of the equivalence between RT turbulence and Boussinesq turbulence in two dimensions [35]. With the present statistics, moments of order higher than 6 are not accessible. Instead, in [35] moments of order larger than 6 are investigated. In [35] the authors observe the saturation of anomalous exponents, i.e. for high orders, the scaling exponents saturate to a constant value. This phenomenon[2] is physically related to the presence of abrupt changes in the spatial structure of the scalar field, the so-called fronts. In the temperature field, these quasi-discontinuities correspond to the boundaries between hot rising and cold descending patches of fluid [35]. In the present study, these

[2]The saturation of exponents is predicted by means of instantonic calculus [7, 40] in the passive scalar context. Concerning the observation of passive-scalar exponent saturation see also [32, 33].

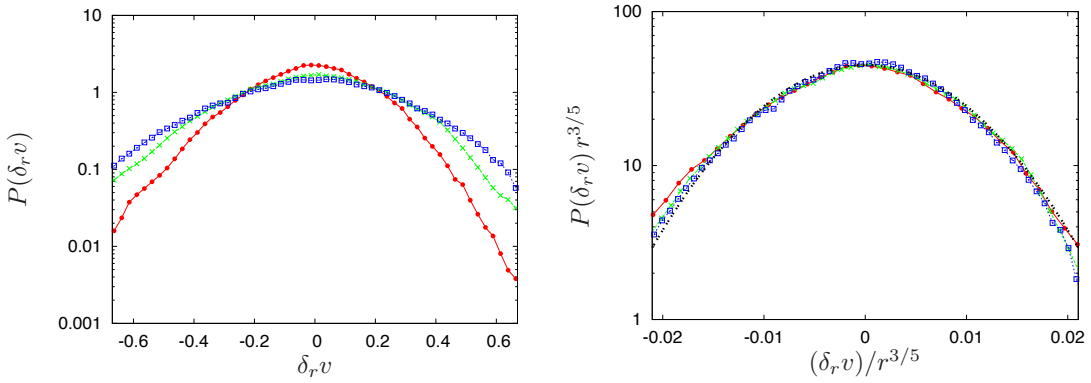


**(a)** PDF of velocity increments

**(b)** PDF of velocity increments rescaled by the Bolgiano prediction

**Figure 2.6:** The probability density functions (PDFs) of the velocity increments for three different separations in the inertial range of scales (see Fig. 2.5): $r/L_x = 0.14$, $r/L_x = 0.23$ $r/L_x = 0.31$, **(a)** without rescaling and **(b)** with rescaling corresponding to the Bolgiano prediction [41]. In **(b)** the Gaussian probability density is shown for comparison (dashed line).

boundaries are easily recognizable in the temperature-field snapshots in Fig. 2.1. It is easy to understand because the fronts are related to the intermittency. The probability of strong, rare fluctuations between two points increases as the two points approach with one another (i.e., at smaller and smaller scales $r$). As a consequence the PDFs of temperature field, as the separation $r$ decreases, change shape and display higher and higher tails.
Our claim on the possible equivalence between RT and driven 2D Boussinesq turbulence can be further corroborated by looking at the temporal behaviour of structure functions. Dimensional predictions immediately follow from Eqs. (1.24) and (1.23). The latter are well verified for all displayed orders for the velocity field (see Fig. 2.7a). For the temperature field, anomalous corrections start to appear at the fourth order and are of the form:

$$S_p^T(r) \sim \Theta^p \left[r/L(t)\right]^{p/5} \left[r/L(t)\right]^{-\sigma_p} \quad . \tag{2.5}$$

By assuming (see Fig. 2.5b) that the present RT model possesses the same spatial scaling exponents as those of the model presented in Ref. [41], i.e., $S_4^T \sim r^{0.6}$ and $S_6^T \sim r^{0.7}$ (and thus $\sigma_4 = 0.2$ and $\sigma_6 = 0.5$), we immediately get a prediction for the exponents relative to the temporal behaviour. We just have to remember that $L(t) \sim t^2$ to obtain the scaling relations $S_4^T \sim L^{-0.6} \sim t^{-1.2}$ and $S_6^T \sim L^{-0.7} \sim t^{-1.4}$. The latter are compatible with the results presented in Fig. 2.7b.

## 2.5 Ultimate state of thermal convection

Let us now pass to discuss the behaviour of turbulent heat flux, mean temperature gradient and root-mean-square velocity as a function of time. These quantities are customarily represented in adimensional variables by the Nusselt number

$$\mathcal{N}u \equiv \frac{\text{thermal transport (including advection and diffusion)}}{\text{diffusive thermal transport in the absence of flow}} = \frac{\langle v_z T \rangle L}{(\kappa \Theta)} + 1 \quad , \tag{2.6}$$

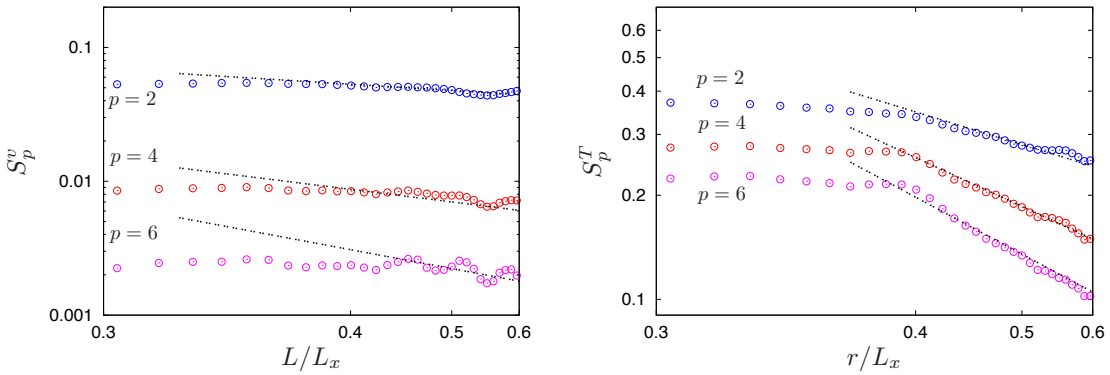


**(a)** temporal evolution of velocity-difference moments

**(b)** temporal evolution of temperature-difference moments

**Figure 2.7:** Evolution with $L$ of moments of velocity differences $S_p^v$ **(a)** and temperature differences $S_p^T$ **(b)**. The results are obtained by averaging over a fixed range of separations belonging to the inertial scales. I found a better scaling behaviour by displaying the behaviour of structure functions as a function of the mixing layer width, $L$, rather than with respect to time. Those are connected by the relation $L \sim t^2$. The dash-dotted lines correspond to the dimensional scaling for velocity and to the intermittency-corrected scaling for temperature (see text for details).

the Rayleigh number

$$\mathcal{R}a \equiv \frac{\text{buoyancy driving force}}{\text{dissipation and viscous forces}} = \frac{g\beta\Theta L^3}{\nu\kappa} \tag{2.7}$$

and the Reynolds number

$$\mathcal{R}e \equiv \frac{\text{inertial force}}{\text{viscous force}} = \frac{v_{rms}L}{\nu} \quad . \tag{2.8}$$

Generally, in the case of natural convection, the velocity, expressed by $\mathcal{R}e$, is not imposed but is set by buoyancy effects. A central issue is to find a relationship between a temperature difference applied to the system, expressed by $\mathcal{R}a$, and the corresponding heat flux, expressed by $\mathcal{N}u$. The question about what functional relations exist among these quantities is a long-debated issue in the context of three-dimensional Rayleigh-Bénard (RB) turbulence[3], (see, for example, Refs. [72, 103, 104, 129, 144] and references therein). In two-dimensional RT turbulence exact expressions linking these adimensional numbers to temperature- and kinetic-energy input/dissipation rates can be derived closely following Ref. [72]. For the RT case one has to deal with the additional complication of time dependence, yet compensated by the simplification originating from the absence of boundary effects. If $\boldsymbol{\partial} \equiv (\partial_1, \partial_2, \partial_3) = (\partial_x, \partial_y, \partial_z)$ and $\boldsymbol{v} \equiv (v_1, 0, v_3) = (u, 0, w)$, from the equations of motion one obtains:

$$\partial_t \langle \boldsymbol{v}^2/2 \rangle = \nu\kappa^2 L^{-4}(\mathcal{N}u - 1)\mathcal{R}a - \nu\langle(\partial_j v_i)(\partial_j v_i)\rangle \tag{2.9}$$

$$\partial_t \langle \theta^2/2 \rangle = \kappa\Theta^2 L^{-2}(\mathcal{N}u - 1) - \kappa\langle|\boldsymbol{\partial}\theta|^2\rangle \quad , \tag{2.10}$$

[3]The Rayleigh–Bénard thermal convection corresponds to the case of a fluid confined between two plates at different temperature. The top plate is colder than the bottom one. Under the Boussinesq approximation the equations ruling the fluid evolution are the same as the RT problem, with constant boundary conditions (i.e. the distance between two plates is constant in time).

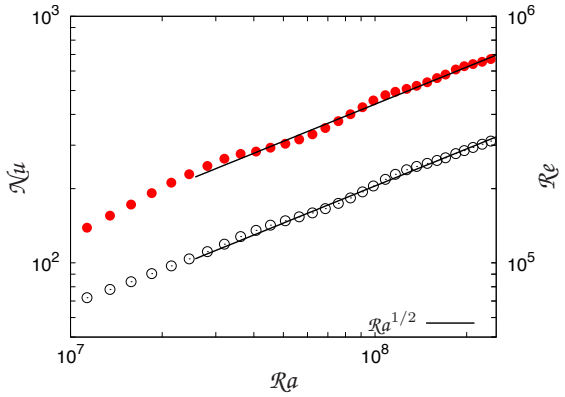


**Figure 2.8:** The behaviour of the Nusselt number (red filled circles) and Reynolds number (open circles) versus the Rayleigh number. The observed slopes are compatible with the $\mathcal{R}a^{1/2}$ behaviour (see text). In this study $\mathcal{P}r$ is equal to 1. Note that the different scales on the two ordinates derive from the indeterminate dimensionless factors in relations (2.13)-(2.14).

$\theta$ being the departure from the mean temperature profile. The two terms $\langle(\partial_j v_i)(\partial_j v_i)\rangle$ and $\langle|\boldsymbol{\partial}\theta|^2\rangle$ are the kinetic and thermal dissipation rates, respectively. These terms describe the kinetic-energy and the thermal-energy dissipations which take place at viscous and diffusive scales respectively.
Since in two-dimensional RT the kinetic energy is transferred upscale, one has a negligible $\nu\langle(\partial_j v_i)(\partial_j v_i)\rangle$ and one can estimate a rate-of-change of kinetic energy $(\beta g\Theta)^2 t$ from the dimensional prediction (1.23) and $L = \beta g\Theta t^2$. For the temperature one has $\langle\theta^2\rangle \sim \Theta^2$ independent of time. Temperature performs a direct cascade and thus dissipation can be estimated as $\delta_L\theta^2\delta_L v/L \sim \Theta^2/t$. Plugging those estimates into the exact relations we have:

$$\mathcal{N}u \sim (\beta g\Theta)^2\kappa^{-1}t^3 \tag{2.11}$$
$$\mathcal{R}a \sim (\beta g\Theta)^4(\nu\kappa)^{-1}t^6 \quad , \tag{2.12}$$

therefore

$$\mathcal{N}u \sim \mathcal{R}a^{1/2}\mathcal{P}r^{1/2} \tag{2.13}$$

where $\mathcal{P}r = \nu/\kappa$ is the Prandtl number.
As for the Reynolds number, relation (1.23) gives:

$$\mathcal{R}e \sim (\beta g\Theta)^2\nu^{-1}t^3 \sim \mathcal{R}a^{1/2}\mathcal{P}r^{-1/2} \quad . \tag{2.14}$$

It is worth remarking that a similar analysis for the 3D RT case leads *mutatis mutandis* to the same scaling laws. In the two-dimensional system, the numerical results allow us to verify these predictions (see Fig. 2.8).
The aforementioned predictions, when considered as a function of $\mathcal{R}a$, coincide with the results derived by Kraichnan for the pure bulk contribution to 3D RB turbulence in the regime of very large Rayleigh numbers [82]. In this state, the heat flux and the turbulent velocity are expected to be independent of viscosity and heat diffusivity. Physically the heat is advected by gravitationally driven buoyant structures (e.g., the thermal plumes). However, such Kraichnan scaling regime for RB convection, also dubbed "the ultimate state of thermal

convection", has so far eluded both numerical and experimental confirmation [3, 104]. The reason may be traced back to the fundamental role played by the boundaries in establishing the turbulent heat transport in RB convection. Indeed, when boundaries are artificially removed as in the numerical simulations of Refs. [28, 64, 93], the Kraichnan scaling is clearly observed. In this context, RT turbulence provides a natural framework where heat transport takes place exclusively by bulk mechanisms, and thus provides a physically realisable example of the Kraichnan scaling regime, inviting further experimental and numerical effort in this direction.

## 2.6 Conclusions

Two-dimensional Rayleigh–Taylor turbulence is well described by the phenomenological theory presented by Chertkov (see Sec. 1.4.2.2) at least for low-order statistics. However, strong intermittency effects appear for temperature increments already at level of fourth-order structure functions. Such corrections are in quantitative agreement with previous results obtained in two-dimensional Boussinesq driven convection [34, 35]. This points to the equivalence between two-dimensional Rayleigh–Taylor turbulence and two-dimensional Boussinesq driven convection with a linear, adiabatically decreasing mean temperature profile.

Equivalence means that these different settings of thermal convection belong to the same universality class. The presence of intermittency corrections reflects the breakdown of scale invariance and the large scales explicitly appears in the inertial-range expressions of temperature correlations. Therefore, the question on the independency of the behaviour at large scales (the so-called universality problem) arise. Having the same anomalous scaling exponents means that the physical mechanism ruling the dynamics at small scales, are the same, although the details of flow at large scales are different.

Finally, the numerics point out to the conclusion that Rayleigh–Taylor turbulence might provide a physical realisation of the "ultimate state of thermal convection" [82].

# Chapter 3

# Miscible three-dimensional configuration

*"... Alice remained looking thoughtfully at the mushroom..."*
Alice's adventures in wonderland by Lewis Carroll (1865)

The three-dimensional miscible RT turbulence is investigated by means of high-resolution numerical simulations. In three dimensions, the phenomenological theory, recently presented in [41] (and described in Sec. 1.4.2.1), predicts a Kolmogorov–Obukhov–Corrsin turbulent cascade in which temperature fluctuations are passively transported. This scenario, which is partially supported by numerical simulations [26, 44], has however been contrasted by an alternative picture which rules out Kolmogorov phenomenology [114].
The first aim of the present study is to clarify the above controversy through a deep analysis of the scaling behaviour of relevant statistical observables. Moreover, another important question is addressed here: can the RT phenomenology be considered as a manifestation of universality of Navier–Stokes equation with respect to the forcing mechanism? With this aim, the effects of intermittency on the mean-field scaling predictions are also discussed.

The chapter is organised as follows. After providing a description of the numerical setup, we describe our results. Sec 3.2 is devoted to single out the mechanism ruling the turbulence evolution. In Sec 3.3 the intermittency phenomenon is analysed by focusing on the kinetic-energy dissipation statistics and the velocity structure functions (i.e., the moments of velocity increments) statistics. Sec 3.4 deals with the scaling of global quantities. Finally, the main results are summarised in Sec 3.5.

## 3.1 Numerical setting

We consider the three-dimensional, incompressible, miscible RT flow in the Boussinesq approximation (see Sec. 1.4.2):

$$\partial_t \boldsymbol{v} + \boldsymbol{v} \cdot \boldsymbol{\partial} \boldsymbol{v} = -\boldsymbol{\partial} p' + \nu \partial^2 \boldsymbol{v} + \beta \boldsymbol{g} T \tag{3.1}$$

$$\partial_t T + \boldsymbol{v} \cdot \boldsymbol{\partial} T = \kappa \partial^2 T \quad . \tag{3.2}$$

where $\boldsymbol{g}$ is selected along the $z$ axis. At time $t = 0$ the system is in the initial configuration described in Sec 2.2. The previous equations are integrated by means of a standard 2/3-dealiasing pseudospectral method (see App. B) on a periodic domain with uniform grid spacing, square basis $L_x = L_y$ and aspect ratio $L_x/L_z = r$. The DNS (see page 13) are carried out on a $512 \times 512 \times N_z$ vertically expanding grid. At the beginning of the simulation, $N_z$ is 512 and $r = 1/2$, at the end $N_z$ reaches a value of 2048 and $r = 1/4$. In all runs, $\mathcal{A}g = 0.25$ (model units), the Prandtl number $\mathcal{P}r = \nu/\kappa = 1$, and the initial jump of temperature $\Theta = 1$ (model units). Viscosity must be taken sufficiently large to resolve small scales, and thus to describe the turbulence dynamics accurately. According to the Chertkov predictions [41], the dissipative scale $\eta(t)$ given by (1.25), decreases in time and, as a consequence, numerical investigations in three dimensions are trickily than in two dimensions. However, at the final time, we have $\eta(t)/r_{min} \simeq 1.2$, $r_{min}$ being the smallest scale resolved by the code.
In the results, scales and times are made dimensionless with the larger box scale $L_z$ and the characteristic time $\tau = (L_z/(\mathcal{A}g))^{1/2}$ [48]. Moreover, we denote the velocity components as $\boldsymbol{v} \equiv (u, v, w)$.
RT instability is seeded by perturbing the initial condition with respect to the step profile. Two different perturbations are implemented in order to check the independence of the turbulent stage from initial conditions. In the first case, the interface at $T = 0$ is perturbed by a superposition of small-amplitude waves in a narrow range of wavenumbers around the most unstable linear mode [119]. For the second set of simulations, we perturbed the initial condition by "diffusing" the interface around $z = 0$. Specifically, we added a $10\%$ of white noise to the value of $T(\boldsymbol{x}, 0)$ in a small layer of width $L_0$ around $z = 0$.

## 3.2 Quasiequilibrium Kolmogorov scenario

The analysis of the mixing-layer growth is presented in Fig. 3.1a. By implementing the method described in Sec. 1.4.1, an almost constant value of $\alpha \simeq 0.038$ (red filled circles) for $t/\tau \simeq 1.5$ is observed. The constant value is consistent with previous studies [26, 54, 124][1]. Fig. 3.2 shows a snapshot of the temperature field for a simulation with $r = 1/2$ within the similarity regime. The large-scale structures (the thermal plumes) identify the gravity direction. As discussed on page 15, the gravity introduces anisotropy effects. The scale dependence of the anisotropy can be quantified by $w_{rms}/u_{rms}$, which gives information of possible large-scale anisotropy, and by $(\partial_z w)_{rms} / (\partial_x u)_{rms}$ which, on the contrary, gives information of possible small-scale anisotropy. We find that at small scales isotropy is almost completely recovered: $w_{rms}/u_{rms} \simeq 1.8$ and $(\partial_z w)_{rms} / (\partial_x u)_{rms} \simeq 1.0$. Therefore a stronger anisotropy is observed at large scales than a small ones (as observed by [26]). Moreover, the horizontally averaged temperature $\langle T \rangle_z$, shown in Fig. 3.1b, closely follows a linear profile within the mixing layer where, therefore, the system recovers statistical homogeneity. These results are thus in agreement with classical picture of turbulence where isotropy tends to be restored at small scales despite the presence of large-scale anisotropy.
As the RT instability flow evolves, the initial energy spectrum of the perturbation grows and

[1] In [26] a different operational definition of the mixing-layer thickness is used. Their and our $\alpha$-values are compatible.

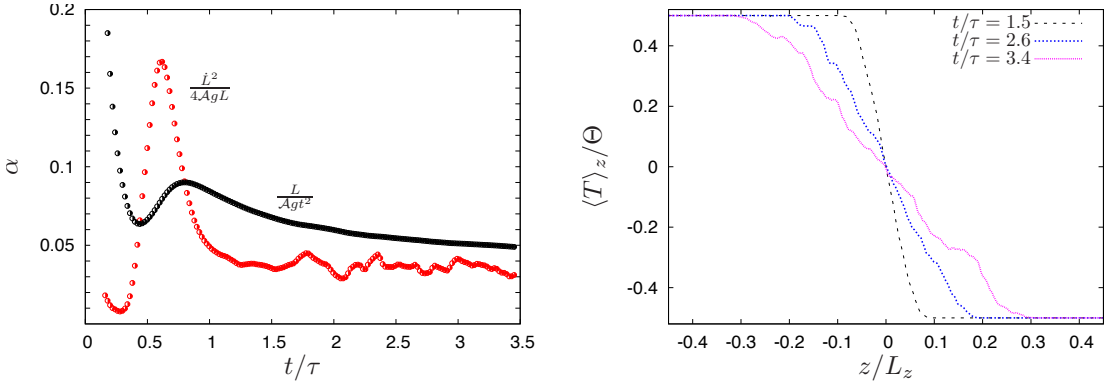


**(a)** mixing-layer growth parameter **(b)** horizontally-averaged temperature

**Figure 3.1:** **(a)** The mixing-layer thickness $L$ and its growth rate $\dot{L}$ adimensionalized. Black simbols $\alpha = L/\left(\mathcal{A}gt^2\right)$ and red symbols $\alpha = \dot{L}^2/\left(4\mathcal{A}gL\right)$. The mixing-layer thickness $L(t)$ is defined as described on page 1. **(b)** Horizontally averaged temperature $\langle T\rangle_z$ for times $t/\tau = 1.5$ (black line), $t/\tau = 2.6$ (blue line) and $t/\tau = 3.4$ (violet line). The results are obtained from runs with a resolution up to $512 \times 512 \times 2048$ and aspect ratio up to $r = 1/4$.

**Figure 3.2:** Black (light orange) fluid is the cold (hot) one. The other colours represent mixed fluid of various compositions. The gravity is directed downward. The simulation time is $t/\tau = 2.6$ which corresponds to a time belonging to the self-similar regime (see Fig. 3.1a). The aspect ratio is $r = 1/2$ and $N_x \times N_y \times N_z = 512 \times 512 \times 1024$.

broadens, eventually developing an inertial range. Fig. 3.3a shows temperature and velocity spectra within the similarity regime. As time runs, the peak of each spectrum moves to lower wavenumbers, whereas the tail (dissipation range) moves to higher wavenumbers: hence the range of scales participating in the dynamics grows. This observation qualitatively confirms the Chertkov predictions: the time evolution of $L(t)$, given by (1.18), and the time evolution of the dissipative scale $\eta(t)$, given by (1.22), allow the time growth of the inertial range. More quantitatively, from the relations (1.19) and (1.20), the following spatial-temporal scalings of spectra[2]

$$E^v(k,t) \sim k^{-5/3}t^{2/3} \tag{3.4}$$
$$E^T(k,t) \sim k^{-5/3}t^{-4/3} \tag{3.5}$$

are expected. In Fig. 3.3a, Kolmogorov scaling $k^{-5/3}$ is evident for both velocity and temperature fluctuations. Moreover, the self-similar temporal evolution of spectra is well reproduced as shown in the inset. In order to confirm the presence of the Kolmogorov–Obukhov–Corrsin scenario, we verify that the temperature fluctuations are transported passively in the cascade, that is, the buoyancy term $\beta g T$, at small scales, becomes subleading in Eq. (3.1) (see Sec. 1.4.2.1 and relation (1.21)). The two contributions to kinetic-energy flux in spectral space are also shown in Fig. 3.3b. The buoyancy contribution, dominant at large scales, becomes subleading at smaller scales, in agreement with the Kolmogorov–Obukhov–Corrsin picture.

The above results, together with previous simulations [26, 44] and theoretical arguments [41], give a coherent picture of RT turbulence as a Kolmogorov cascade of kinetic energy forced by large-scale temperature instability and reject the alternative interpretation recently proposed [114].

In the following section we push this analogy one step ahead by showing that small-scale fluctuations in RT turbulence are intermittent and their statistical signature gives rise to corrections to the mean-field scaling exponents whose values are compatible with those occurring in Navier–Stokes turbulence.

## 3.3 Intermittency and universality

This section is devoted to the investigation of the small-scale intermittent statistics of velocity fluctuations.

Differently from two-dimensional turbulence, in three dimensions the velocity is, generally, expected to be intermittent and the reason of this difference is still an open problem [21,108]. The intermittency can be studied both considering the velocity increments, across a distance

[2]Kinetic-energy spectrum $E^v(k)$ is defined as the integral of the square modulus of velocity over a shell with fixed modulus $k$ in Fourier space:

$$E^v(k) = \frac{1}{2}\int k^2 d\Omega_k |\hat{\boldsymbol{v}}(\boldsymbol{k})|^2 \tag{3.3}$$

where $\int d\Omega_k$ indicates the integral over angular variables. If $E^v = \langle|\boldsymbol{v}|^2\rangle/2$ is the total energy, the Parseval equality for Fourier transforms allows to write: $E^v = \int_0^\infty dk E^v(k)$. It can be shown [60] that, if $E^v(k) \sim k^n$ with $1 < n < 3$ the second-order longitudinal structure function of $\boldsymbol{v}$ is a power law of the form $S_2^v \sim (\delta_r v)^2 \sim r^{n-1}$. *Mutatis mutandis* for the temperature-variance spectrum $E^T(k)$.

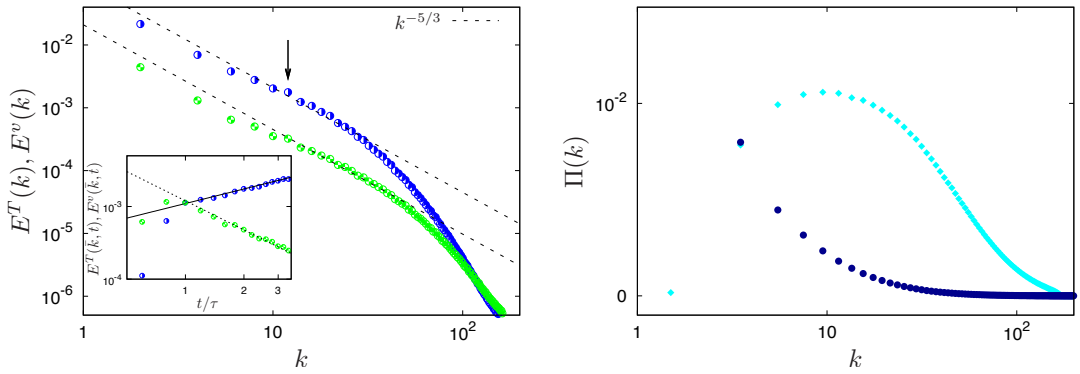


**(a)** spectra **(b)** contributions to kinetic-energy flux

**Figure 3.3:** **(a)** Two-dimensional kinetic-energy spectrum (blue filled circles) and temperature-variance spectrum (green filled circles) at time $t/\tau = 2.6$. Spectra are computed by Fourier transforming velocity and temperature fields on two-dimensional horizontal planes and averaging over $z$ planes in the mixing zone. Dashed lines represent Kolmogorov scaling $k^{-5/3}$. The black arrow points to the wavenumber $\bar{k} = 12$ considered in the inset. **Inset:** time evolution of the amplitude of kinetic-energy (blue filled circles) and temperature-variance (green filled circles) spectra at fixed wavenumber $\bar{k} = 12$. Lines represent the dimensional predictions $\sim t^{2/3}$ (continuous line) and $\sim t^{-4/3}$ (dashed line) given by relations (1.19) and (1.20). **(b)** Inertial (rhombi) and buoyancy (filled circles) contributions to kinetic-energy flux $\Pi(k)$ in Fourier space.

$r$, and the fluctuations of the local velocity dissipation averaged on a ball of radius $r$ [60]. We report results concerning both approaches.

Before discussing our results, let us provide a short background of Navier–Stokes turbulence in order to clarify where the intermittency manifests itself (for details see the App. A).

In the fully developed turbulence and in the presence of forcing at large scale, one has a non-equilibrium statistical steady state, with a range of scales (the so-called inertial range), where neither energy pumping nor dissipation act. The inertial range shows strong departures from the equipartition [24, 60]. A simple and elegant explanation of the main statistical features of the fully developed turbulence is due to Kolmogorov in 1941 (K41) [79, 80]: briefly, he assumed the existence of a range of scales (the inertial range) where the energy, injected at large scale $L$, flows down to the viscous scale $\eta$, where it is dissipated by molecular viscosity. Since, neither injection nor dissipation takes place in the inertial range, the only relevant quantity is the average energy transfer $\epsilon_v$ (in the following, for the sake of notation $\epsilon_v$ is replaced by $\epsilon$). Under the assumption of stationarity, homogeneity and isotropy, Kolmogorov [60, 79] derived an exact relation, from the Navier–Stokes equation, for the third-order moment of the longitudinal velocity increments:

$$\langle (\delta_r v)^3 \rangle = \langle \{ [\boldsymbol{v}(\boldsymbol{x}+\boldsymbol{r},t) - \boldsymbol{v}(\boldsymbol{x},t)] \cdot \boldsymbol{r}/r \}^3 \rangle = -\frac{4}{5}\epsilon\, r \quad . \tag{3.6}$$

This relation is the so-called "four-fifths" law. The sign minus is the fingerprint of the energy flow from large to small scales [60]. Note that the "four-fifths" law implies that the third-order moment is universal (for a discussion on this subject, see [61]), that is, it depends on the injection and the dissipation only through the mean energy injection rate, coinciding with $\epsilon$ in the stationary state. To obtain other statistical indicators, a natural step made by

Kolmogorov himself was to assume the statistics in the inertial range to be scale invariant. The scale invariance amounts to assuming that the probability density function (PDF) of rescaled velocity differences $r^{-h}\delta_r v$ can be made $r$-independent for an appropriate $h$. The $p$th-order moment of the longitudinal velocity increments (i.e., longitudinal structure functions) would then depend on the separation as a power law $r^{\zeta_p}$ with the "normal scaling" behaviour $\zeta_p = p\,h$. The scaling exponents $h$ may be determined by the "four-fifths" law, e.g., $h = 1/3$ for the Navier–Stokes turbulence. This result is not in agreement with several experimental investigations [60, 133]. Indeed the structure functions are found experimentally to have a power-law dependence on the separation $r$ but with scaling exponents which deviate from the dimensional predictions[3]. This phenomenon, which goes under the name of intermittency, is a consequence of non-uniform transfer of energy. Indeed the PDF of the velocity differences at various separations cannot be collapsed one onto another by simple rescaling.
Several studies have been devoted to the intermittent statistics in Navier–Stokes turbulence, where the main issue concerns the possible universality of the anomalous scaling exponents with respect to the forcing mechanisms and the large-scale geometry of the flow. While the universality has been demonstrated for the simpler problem of passive-scalar transport [31] (and references therein), it is still an open issue for nonlinear Navier–Stokes turbulence.
Therefore, in this context, the key question is on whether small-scale statistics in RT turbulence belongs to the same universality class of Navier–Stokes turbulence.

The simplest, and historically first, evidence of intermittency is in the dependence of energy dissipation on Reynolds number [37, 81, 98, 105, 140]. The basic assumption in the K41 theory is that $\epsilon$ should be the only relevant parameter in the cascade process. This hypothesis is reasonable only if the energy transfer (or the energy dissipation) $\epsilon(\boldsymbol{x})$ does not strongly fluctuate by varying $\boldsymbol{x}$ over a scale $r$ which one is looking at. The presence of intermittency, as first pointed out by Landau (see Sec. 6.4 in [60] and references therein), leads to a contradiction in the K41. Indeed, the statitistical law at small scales have to depend not only on $\epsilon$ but also on the fluctuations of $\epsilon(\boldsymbol{x})$; now the velocity increments $\delta_r v$ scale as $(\epsilon_r r)^{1/3}$, where $\epsilon_r$ is the energy dissipation space-averaged over a ball of radius $r$ and centred at the point $\boldsymbol{x}$ [81, 105]. Therefore, the study of the statistics of the dissipation rate becomes interesting and important.
Classical statistical indicators are the flatness $K$ of velocity derivatives (corresponding to $K \simeq \langle\epsilon(\boldsymbol{x})^2\rangle/\langle\epsilon(\boldsymbol{x})\rangle^2$ in terms of energy dissipation) [98, 140, 143], and the variance of the logarithm of kinetic-energy dissipation [81] which is expected to grow with Reynolds number as

$$\sigma^2_{\ln\epsilon} = A + (3\mu/2)\ln\mathcal{R}_\lambda \tag{3.7}$$

where $A$ depends on large-scale motions and $\mathcal{R}_\lambda \equiv (w_{rms})^2/\left[(\partial_z w)_{rms}\,\nu\right]$ is the Reynolds number based on the Taylor scale[4]. The exponent $\mu$ is the key ingredient for the log-normal model of intermittency[5] [81] and its value is determined experimentally [134, 140]

[3] This violation of the dimensional predictions for the scaling laws is referred to as "anomalous scaling".

[4] It is traditional for experimental and numerical data of fully developed turbulence to avoid the use of the Reynolds number based on the integral scale (the scale where the energy is injected), and the r.m.s. velocity, in favour of the Reynolds number based on the Taylor scale (defined as $\lambda \equiv w_{rms}/(\partial_z w)_{rms}$) because it is easier to measure [60].

[5] Following a suggestion of Obukhov [105], Kolmogorov [81] refined his original theory [79, 80] to take into account the fluctuations of the dissipation. He supposed that the $\epsilon_r(\boldsymbol{x})$ is distributed according to a

and numerically [146] to be $\mu \simeq 0.25$. More in general, the moments of local energy dissipation are expected to have a power-law dependence on $\mathcal{R}_\lambda$

$$\langle \epsilon(\boldsymbol{x})^p \rangle \simeq \epsilon^p {\mathcal{R}_\lambda}^{\tau_p} \tag{3.8}$$

where we remember that $\epsilon \equiv \langle \epsilon(\boldsymbol{x}) \rangle$. Moreover the set of exponents $\tau_p$ can be predicted within the multifractal model of turbulence[6] [22,23,60,107,109] in terms of the set of fractal dimensions $D(h)$. Because in RT turbulence the Reynolds number increases with time, it provides a natural framework for a check of (3.7) and (3.8). Figure 3.4 shows the dependence of the variance of $\ln \epsilon$ on $\mathcal{R}_\lambda$ together with the first moments of energy dissipation.

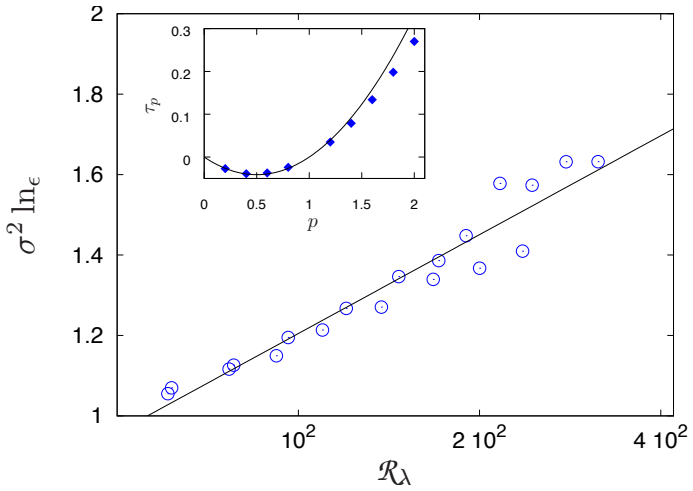


**Figure 3.4:** Scaling of the variance of $\ln_\epsilon$ on Reynolds number defined as $\mathcal{R}_\lambda = (w_{rms})^2 / [(\partial_z w)_{rms}\, \nu]$, obtained from two realisations with white-noise initial perturbation. The line is the best fit corresponding to $\mu = 0.24$ in (3.7). **Inset:** scaling exponents of the moments of local dissipation $\tau_p$ obtained from best fits according to (3.8). The line represents the log-normal approximation $\tau_p = (3/4)\mu(p^2 - p)$.

Despite the limited range of $\mathcal{R}_\lambda$, a clear scaling of $\ln \epsilon$ is observable, even if with some fluctuations. The best fit with (3.7) gives an exponent $\mu \simeq 0.24$, very close to what observed in homogeneous, isotropic turbulence [146].
Scaling exponents $\tau_p$ for the moments of dissipation (3.8) are also shown in Fig. 3.4. We were able to compute moments up to $p = 2$ with statistical significance. The log-normal approximation, which is in general valid for $p \to 0$, is found to be unsatisfactory for larger values of $p$ (see Apps. in [107]). For $p = 2$, which corresponds to the flatness $K$ of velocity derivatives, we find $\tau_2 \simeq 0.27$. This result is consistent with experiments at comparable Reynolds numbers [140] which shows that $K \sim {\mathcal{R}_\lambda}^{0.2}$ for $\mathcal{R}_\lambda < 200$ while an asymptotic exponent $\tau_2 \simeq 0.41$ is reached for $\mathcal{R}_\lambda > 10^3$ only.
In NS turbulence intermittency is also observed in the inertial range of scales as deviations of velocity structure functions $S_p(r) = \langle (\delta_r v)^p \rangle$ from the dimensional prediction (1.19)

lognormal in the inertial range.

[6] The multifractal approach assumes that the velocity has a local scale invariance, that is, there is not a unique scaling exponent $h$ such that $\delta_r v \sim r^h$, but a continuous spectrum of exponents, each of which belonging to a given fractal set with dimension $D(h)$.

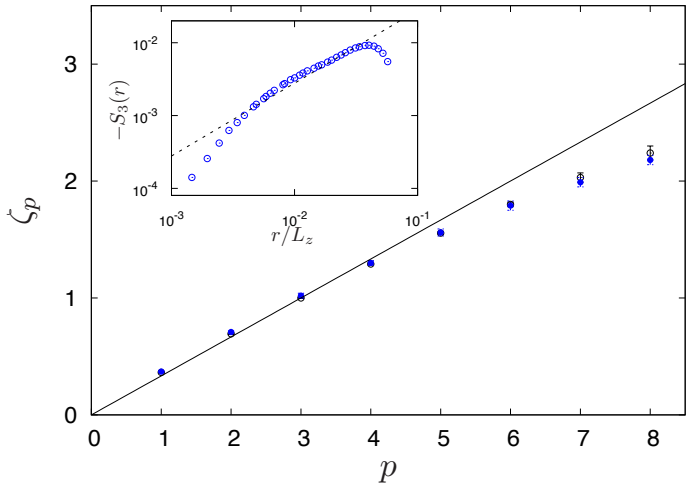


**Figure 3.5:** Scaling exponents of isotropic longitudinal velocity structure functions $S_p(r) = \langle(\delta_r \mathbf{v} \cdot \hat{\mathbf{r}})^p\rangle$ ($\hat{\mathbf{r}} = \mathbf{r}/r$) for the late stage of RT turbulence (open circles). Exponents are computed by compensation of $S_p(r)$ with $S_3(r)$, according to the ESS procedure [10]. Average is performed inside the mixing layer and over all the possible directions to extract the isotropic contribution [16]. Filled circles: scaling exponents from simulations of homogeneous, isotropic turbulence at $R_\lambda = 381$ [66]. The line represents the dimensional prediction $\zeta_p = p/3$. **Inset**: third-order isotropic longitudinal structure function $S_3(r)$. The line represents the Kolmogorov "four-fifths" law $S_3(r) = -(4/5)\epsilon r$.

which corresponds to $S_p(r) \simeq r^{p/3}$ [60]. Anomalous scaling is observed, which corresponds to scaling laws $S_p(r) \simeq r^{\zeta_p}$ with a set of exponents $\zeta_p \neq p/3$. We remind that the constancy of energy flux in the inertial range implies $\zeta_3 = 1$ independently of intermittency, as required by the Kolmogorov "four-fifths" law $S_3(r) = (-4/5)\epsilon r$ [60], which is indeed observed in our simulations (see inset of Fig. 3.5). Figure 3.5 shows first few longitudinal scaling exponents computed from our simulations using the extended self-similarity procedure (ESS)[7] which allows for a precise determination of the exponents at moderate Reynolds numbers [10]. A deviation from the dimensional prediction $\zeta_p = p/3$ is clearly detectable for higher moments. Fig. 3.5 also shows the scaling exponents obtained from a homogeneous and isotropic simulation of NS equations at a comparable $\mathcal{R}_\lambda$ [66]. The two sets agree with each other within the error bars, thus giving further quantitative evidence in favor of the equivalence between RT turbulence and NS turbulence in three dimensions.

## 3.4 Ultimate state of thermal convection

We end by discussing the behaviour of turbulent heat flux and the r.m.s. velocity as a functions of the mean temperature gradient. Our objective is to investigate the presence of the "ultimate state of thermal convection" (see Sec. 2.5 for details). The ultimate-state

[7] The width of the scaling range is usually not large enough to determine the scaling exponents precisely. Extended self-similarity has been exploited to overcome this difficulty. The idea is to measure the scaling exponents of the structure functions when they are plotted against the third-order longitudinal structure function, rather than to use the separation distance. The width of the scaling range is longer than that obtained with the usual method at low and moderate Reynolds numbers.

relations can formally be obtained from kinetic-energy and temperature balance equations [72]. In the context of RT turbulence, they are a simple consequence of the dimensional scaling of the mixing length $L \equiv h \simeq \beta g \Theta t^2$ and of the r.m.s. velocity $v_{rms} \simeq \beta g \Theta t$. As it is evident from the derivation reported in Sec. 2.5 in a two-dimensional study, the ultimate-state relations involve large-scale quantities only, and are therefore independent of the statistics of the inertial range and on the presence of intermittency. Then, in a way similar to the two-dimensional case, the three-dimensional ultimate-state relations are obtained. The only difference is the kinetic-energy dissipation value. Now it is not zero (indeed the kinetic energy flows down to the small scales), and it can be estimated as ${v_{rms}}^3/L \sim (\beta g \Theta)^2 t$. Therefore one again obtains the following relations:

$$\mathcal{N}u \sim \mathcal{P}r^{1/2}\mathcal{R}a^{1/2} \tag{3.9}$$

$$\mathcal{R}e \sim \mathcal{P}r^{-1/2}\mathcal{R}a^{1/2} \tag{3.10}$$

where $\mathcal{P}r = \nu/\kappa$. In the present study $\mathcal{P}r$ is selected equal to 1.
Numerical results shown in Fig. 3.6 confirm the predictions (3.9)-(3.10).

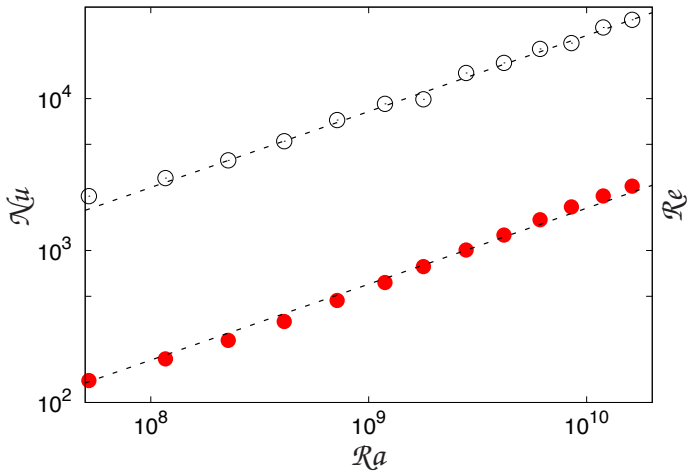


**Figure 3.6:** The scaling of Nusselt number $\mathcal{N}u$ (red filled circles) and Reynolds number $\mathcal{R}e$ (black circles) as functions of Rayleigh number $\mathcal{R}a$. Dashed lines are the ultimate-state prediction $\sim \mathcal{R}a^{1/2}$, relations (3.9) and (3.10).

## 3.5 Conclusions

In this numerical investigation we focus our attention on the three-dimensional miscible RT turbulence. The goal of this work is twofold. From one hand, we give a strong numerical support to the phenomenological theory *à la* Kolmogorov in RT turbulence. On the other hand, the analogy with the usual Navier–Stokes turbulence is push much further: the small-scale velocity fluctuations in RT turbulence are found to belong to the same universality class of Navier–Stokes equation.
Moreover, from both 2D (results described in Sec. 2.5) and 3D investigations, it emerges the elusive Kraichnan scaling in thermal convection, i.e. the "ultimate state of thermal

convection", finds its natural manifestation in RT turbulence which turns out to be an excellent setup for experimental studies in this direction.

# Chapter 4

# Surface tension effect and phase-field approach

*"... Anche il corpo del Gramo ora buttava sangue per tutta l'enorme antica spaccatura: i fendenti dell'uno e dell'altro avevano rotto di nuovo tutte le vene e riaperto la ferita che li aveva divisi, nelle sue due facce. Ora giacevano riversi, e i sangui che già erano stati uno solo ritornavano a mescolarsi per il prato..."*
Il visconte dimezzato by Italo Calvino (1952)

In many of the situations where the RT instability has an important role, the two fluids are immiscible owing to a non negligible surface tension. RT instability of two immiscible fluids in the limit of small Atwood numbers is studied by means of a phase-field model. The essence of this method is that the sharp fluid interface is replaced by a thin, yet finite, transition layer where the interfacial forces vary smoothly. This is achieved by introducing an order parameter (the phase field) continuously varying across the interfacial layers and uniform in the bulk region. The phase-field model obeys a Cahn–Hilliard equation and is two-way coupled to the standard Navier–Stokes equation. Starting from this system of equations we first perform a linear analysis from which we analytically rederive the known gravity-capillary dispersion relation in the limit of vanishing mixing-energy density and capillary width. We perform numerical simulations and identify a region of parameters in which the known properties of the linear phase (both stable and unstable) are reproduced in a very accurate way. This is done both in the case of negligible viscosity and in the case of nonzero viscosity. In the latter situation only upper and lower bounds for the perturbation growth-rate are known. Finally, we also investigate the weakly nonlinear stage of the perturbation evolution and identify a regime characterised by a constant terminal velocity of bubbles/spikes. The measured value of the terminal velocity is in agreement with available theoretical predictions. The phase-field approach thus appears to be a valuable technique for the dynamical description of the stages where hydrodynamic turbulence and wave turbulence enter into play [43].

The chapter is organised as follows. An introduction to the study of binary fluids is given in 4.1. In Sec. 4.2 we introduce the RT problem and discuss the related phase-field approach. A detailed analysis of the energy balance between purely hydrodynamic degrees of freedom and interface degrees of freedom is presented. Finally, the dispersion relation for gravity-capillary waves is obtained by analytical calculations starting from the phase-field equation

coupled to the Navier–Stokes equation.
In Sec. 4.3 the results from the Direct Numerical Simulations are presented and compared with known results for the linear analysis. We focus both on the case of zero viscosity and on that of non-negligible viscosity. Both stable and unstable configurations are considered. Finally, the weakly nonlinear regime is considered and the resulting terminal velocity of bubbles/spikes compared with existing theoretical predictions.
Sec. 4.4 is devoted to some conclusions and perspectives.

## 4.1 Binary flow and interface problem

RT instability and RT turbulence of immiscible fluids appear richer than the corresponding miscible situations [43] (and described in Sec. 1.4.3). The existence of two different cascades poses a serious challenge to numerical investigations of the immiscible RT problems. The emulsion-like phase indeed occurs at very small scales and the energy transfer takes place on the interfaces. These are geometrical objects close to singularities and thus difficult to describe appropriately in a numerical scheme. Accuracy and efficiency are thus fundamental requirements to reproduce the correct statistical features characterising immiscible RT turbulence.
Our aim here is to perform a first step along this direction by focusing on Direct Numerical Simulations of immiscible RT instability. The numerical strategy we exploit here is known as phase-field model [6, 25, 27, 55]. The main idea of the method is to treat the interface between two immiscible fluids as a thin mixing layer across which physical properties vary steeply but continuously. The evolution of the mixing layer is ruled by an order parameter (the phase-field) that obeys a Cahn–Hilliard equation [27]. The method permits to avoid a direct tracking of the interface and easily produces the correct interfacial tension from the mixing layer free-energy.
The phase-field method differs with respect to other standard approaches where, e.g., the interface between two immiscible fluids is modelled as a free boundary that evolves in time with the flow. The resulting equations of motions valid in each fluid domain are supplemented by boundary conditions at the free surface that involve the physical properties of the interface (see, for instance, [39]). Following this latter strategy, in order to handling the moving interface, a mesh with grid points on the interface which deforms according to the flow on both sides of the interface is commonly used. The main limitation of this approach is its inability to handle singular morphological changes such as breakup, coalescence and reconnections (see, [151] and references therein).
These dynamical features can be accurately described by the class of fixed grid methods. According to this technique, the interface is smoothed, a fact that permitted to obtain remarkable results for the quantitative description of deforming interfaces (for the level-set method see, e.g., [126]). Instead of describing the two fluids separately (with the appropriate boundary conditions), these methods represent the interfacial tension as a body force or bulk stress spread over a narrow region covering the interface. Then a single set of governing equations can be written over the entire domain and solved on a fixed grid in a purely Eulerian framework. The phase-field method belongs to this second class. It can be viewed as a physically motivated level-set method where instead of choosing an artificial smoothing

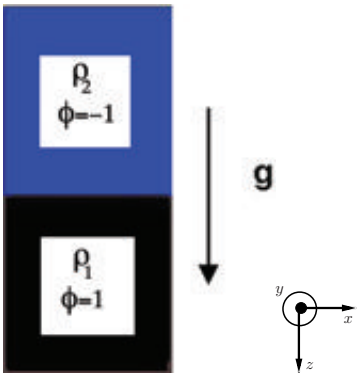


**Figure 4.1:** Fluid configuration corresponding to a heavier fluid of density $\rho_2$ placed above a lighter one of density $\rho_1$ ($< \rho_2$).

function for the interface, which can affect the results in non-trivial ways (see [151] and references therein), the description of the interface is suggested by physics via a mixing energy.

## 4.2 System configuration and phase-field model

The system consists of two immiscible, incompressible fluids (labelled by 1 and 2) having different densities, $\rho_1$ and $\rho_2$ ($> \rho_1$), with the denser fluid placed, e.g., above the less dense one (see Fig. 4.1). Let us start by describing the equilibrium configuration and then pass to the evolution of RT instability.

### 4.2.1 Equilibrium state

Let us consider an equilibrium state where fluid 1 is placed below fluid 2 and they are separated by a sharp interface. The fact that the interface is sharp (i.e. a discontinuity in the fluid properties) poses a serious challenge to numerical simulations. Indeed, for sharp interfaces, the evolution equations are obtained by following fluid 1 and 2 separately with the appropriate boundary condition at interface (see, for instance, [126, 131]). Other approaches follow the interface alone. In this latter case, the movement of the interface is naturally amenable to a Lagrangian description, while the bulk flow is conventionally solved in an Eulerian framework. These approaches employ a mesh that has grid points on the interfaces and deforms according to the flow. A major shortcoming of these approaches is in that they cannot properly handle topological changes such as breakup, coalescence and reconnections (and references therein [151]). In this respect, the phase-field method is, by far and large, more effective, at the expense of a larger number of grid points required.
The idea of the phase-field method is to replace the sharp interface with a diffuse one in such a way that the numerical computation of interface movement and deformation can be carried out on fixed grids [4, 77]. More quantitatively, this amounts to assigning to the system a

Ginzburg–Landau free-energy, $\mathcal{F}$, expressed in term of the order parameter $\phi$ as [25,27,151]:

$$\mathcal{F}[\phi] = \int_\Omega \frac{\Lambda}{2}|\boldsymbol{\partial}\phi(\boldsymbol{x})|^2 + \frac{\Lambda}{4\varepsilon^2}(\phi^2-1)^2 d\boldsymbol{x} \quad , \tag{4.1}$$

where $\Omega$ is the region of space occupied by the system, $\boldsymbol{\partial} \equiv \partial_i$ with $i = 1, \cdots, d$ ($d$ being the space dimensions), and $\varepsilon$ is the capillary width, representative of the interface thickness. In the following we refer to $\Lambda\left[|\boldsymbol{\partial}\phi(\boldsymbol{x})|^2/2 + (\phi^2-1)^2/(4\varepsilon^2)\right]$ as a density of free-energy and to $\Lambda$ as the magnitude of the free-energy. The order parameter $\phi$ is a field which serves to identify fluid 1 and 2. We assume $\phi = 1$ in the region occupied by fluid 1 and $\phi = -1$ in those where fluid 2 is present (see Fig. 4.1).
The equilibrium state is the minimiser of the free-energy $\mathcal{F}$. The mechanism which keeps the system in this configuration is the competition between two effects, due to the two addends in (4.1). The first term favours mixing (i.e. $\Lambda|\boldsymbol{\partial}\phi|^2/2 = 0$ in $\mathcal{F}$, this term being the interface energy contribution) whereas the second one drives the system towards demixing (the associated term in $\mathcal{F}$, the bulk contribution, has indeed a minimum for $\phi = \pm 1$). The nontrivial final equilibrium state is just the result of this competition. More quantitatively, the final state is obtained by minimising the free-energy functional with respect to variations of the function $\phi$, i.e., solving:

$$\mathcal{M} \equiv \delta\mathcal{F}/\delta\phi = 0 \;\Leftrightarrow\; -\partial^2\phi + \frac{\phi^3 - \phi}{\varepsilon^2} = 0 \quad , \tag{4.2}$$

where $\mathcal{M}$ is the so-called chemical potential (see, for instance, [25,27,151]). If one considers an one-dimensional interface, varying along the gravitational direction $z$, one easily finds the solution of Eq. (4.2) as [25, 27, 151]:

$$\phi(z) = \pm \tanh\left(\frac{z}{\sqrt{2}\varepsilon}\right) \quad . \tag{4.3}$$

From the latter expression one immediately realises that the sharp-interface limit is obtained for $\varepsilon \to 0$: in this case $\tanh\left(z/(\sqrt{2}\varepsilon)\right) \to \mathrm{sign}(z)$. Moreover, the surface tension $\sigma$ is equal to the integral of the free-energy density along the interface (see, for example, [88]). For a plane interface, this integral yields [25, 27, 151]:

$$\sigma = \frac{2\sqrt{2}}{3}\frac{\Lambda}{\varepsilon} \quad . \tag{4.4}$$

It is now easy to verify how the sharp interface limit is obtained: it suffices to take the limits $\Lambda$ and $\varepsilon$ to zero keeping $\sigma$ fixed to the value prescribed by surface tension [92].

### 4.2.2 Perturbation evolution

Let us now suppose to impose a small perturbation on the (finite thickness) interface separating the two fluids. Such perturbation will displace the phase-field from the previous equilibrium configuration, which minimised the free-energy $\mathcal{F}$, to a new configuration for which in general, $\mathcal{M} \neq 0$. The system will react so as to try to reach again an equilibrium configuration. In formulae:

$$\partial_t\phi + \boldsymbol{v}\cdot\boldsymbol{\partial}\phi = \gamma\partial^2\mathcal{M} = \gamma\,\Lambda\partial^2\left[-\partial^2\phi + \frac{(\phi^3-\phi)}{\varepsilon^2}\right] \quad , \tag{4.5}$$

$\gamma$ being the so-called mobility (see, for instance, [25, 151]). Notice the presence of the Laplacian operator in front of $\mathcal{M}$ which causes the mass of each fluid to be conserved, as imposed by the physics of the problem under consideration.
The dynamics of the velocity field is governed by the usual Boussinesq Navier–Stokes equation [86] plus an additional stress contribution arising at the interface where the effect of surface tension enters into play [15, 25, 151]. The equations of motion are:

$$(\partial_t v_i + \boldsymbol{v}\cdot\boldsymbol{\partial} v_i) = -\frac{\partial_i p}{\rho_o} + \nu\partial^2 v_i - \frac{\phi}{\rho_o}\partial_i\frac{\delta\mathcal{F}}{\delta\phi} + \frac{\rho'}{\rho_o}\,g_i \tag{4.6}$$

$$\boldsymbol{\partial}\cdot\boldsymbol{v} = 0 \quad . \tag{4.7}$$

In the first equation $\rho_o = (\rho_1+\rho_2)/2$, $\nu$ is the kinematic viscosity and $\mathbf{g}$ is the gravitational acceleration. For the sake of notation we will denote derivatives and velocity (e.g. for $d=3$) as $\boldsymbol{\partial} \equiv (\partial_1,\partial_2,\partial_3) = (\partial_x,\partial_y,\partial_z)$ and $\boldsymbol{v} \equiv (v_1,v_2,v_3) = (u,v,w)$, respectively. The quantity $-\phi\boldsymbol{\partial}(\delta\mathcal{F}/\delta\phi)/\rho_o$ is the coupling term that accounts for capillary forces. It is easy to verify that it can be rewritten as $-\Lambda\left(\partial^2\phi\boldsymbol{\partial}\phi\right)/\rho_o$ plus a gradient term which can be absorbed into the pressure term. Finally, $\rho' g_i/\rho_o$ is the buoyancy contribution, $\rho'$ being the deviation of the actual density, $\rho$, from the mean density $\rho_o$:

$$\rho' = \rho - \rho_o \quad .$$

The buoyancy contribution can be rewritten in terms of $\rho_1$, $\rho_2$ and $\phi$ as:

$$\begin{aligned}\frac{\rho'}{\rho_o}g_i &= \frac{\rho-\rho_o}{\rho_o}g_i = \\ &= \frac{\rho_1\left(\frac{1+\phi}{2}\right)+\rho_2\left(\frac{1-\phi}{2}\right)-\rho_o}{\rho_o}\,g_i \\ &= -\mathcal{A}\phi\,g_i\end{aligned} \tag{4.8}$$

where $\mathcal{A}$ is the Atwood number introduced on page 2.

### 4.2.3 Energetics

Let us define the kinetic energy (per unit volume), $E_K$, and the potential energy (per unit volume), $E_P$, for our system ruled by Eqs. (4.5), (4.6) and (4.7).
By definition of potential energy, one has:

$$\begin{aligned}E_P &= \frac{1}{\Omega}\int\int dx\,dz\,\rho_2\,g\,z\frac{1-\phi}{2} + \frac{1}{\Omega}\int\int dx\,dz\,\rho_1\,g\,z\frac{1+\phi}{2} + E_P^o = \\ &= -\frac{1}{2}\langle z\,\phi\rangle(\rho_2-\rho_1)g = -\rho_o\,\mathcal{A}\,g\,\langle z\,\phi\rangle \quad ,\end{aligned} \tag{4.9}$$

$\Omega$ being the total volume occupied by the fluids and brackets, $\langle\cdots\rangle$, denote spatial averages. In Eq. (4.9) the constant $E_P^o$ is chosen such to set the potential energy to zero for vanishing Atwood number.

In a similar way, one can define the kinetic energy per unit volume as:

$$\begin{aligned} E_K &= \frac{1}{\Omega}\int\int dx\,dz\,\rho_2\,\frac{1-\phi}{2}\,\frac{\boldsymbol{v}^2}{2} + \frac{1}{\Omega}\int\int dx\,dz\,\rho_1\,\frac{1+\phi}{2}\,\frac{\boldsymbol{v}^2}{2} = \\ &= \rho_2\left\langle\left(\frac{1-\phi}{2}\right)\,\frac{\boldsymbol{v}^2}{2}\right\rangle + \rho_1\left\langle\left(\frac{1+\phi}{2}\right)\,\frac{\boldsymbol{v}^2}{2}\right\rangle = \\ &= \rho_o\left\langle\frac{\boldsymbol{v}^2}{2}\right\rangle - \rho_o\,\mathcal{A}\left\langle\phi\,\frac{\boldsymbol{v}^2}{2}\right\rangle \quad . \end{aligned} \tag{4.10}$$

From Eqs. (4.5) and (4.6) we immediately realise that such equations are left invariant under the simultaneous transformation $\boldsymbol{g}\rightarrow-\boldsymbol{g}$, $\phi\rightarrow-\phi$. As a consequence, $\langle\phi\,\boldsymbol{v}^2/2\rangle=0$ and the resulting kinetic energy simply reads:

$$E_K = \rho_o\left\langle\frac{\boldsymbol{v}^2}{2}\right\rangle \quad . \tag{4.11}$$

By defining $E_{\mathcal{F}}\equiv\mathcal{F}/\Omega$ the total energy of the two-fluid system is

$$E = E_P + E_K + E_{\mathcal{F}} \quad .$$

The equation for $E_K$ is obtained by multiplying Eq. (4.6) by $\rho_o v_i$ and then taking spatial average. We easily get:

$$dE_K/dt = \rho_o\partial_t\left\langle\frac{\boldsymbol{v}^2}{2}\right\rangle = -\rho_o\nu\left\langle(\partial_i\,\boldsymbol{v})^2\right\rangle + \rho_o\,\mathcal{A}\,g\,\langle w\phi\rangle - \Lambda\left\langle v_i\,(\partial_i\phi)\,\left(\partial^2\phi\right)\right\rangle \quad . \tag{4.12}$$

Let us now take Eq. (4.5), multiply it by $y$, and take the average. Exploiting translational invariance and Leibniz rule, the following equation can be easily obtained

$$\partial_t\langle z\,\phi\rangle + \langle z\,\partial_z\,(w\phi)\rangle \;=\; \gamma\Lambda\left\langle z\,\partial^2\left(-\partial^2\phi\;+\;\frac{\phi^3-\phi}{\varepsilon^2}\right)\right\rangle = 0 \quad . \tag{4.13}$$

We thus have:

$$dE_P/dt = -\partial_t\left(\rho_o\mathcal{A}g\langle z\,\phi\rangle\right) = -\,\rho_o\mathcal{A}g\langle w\phi\rangle \quad , \tag{4.14}$$

where we have used the fact that $\langle z\partial_z(w\phi)\rangle = -\langle(\partial_z z)w\phi\rangle = -\langle w\phi\rangle$. The free-energy variation is:

$$\begin{aligned} \partial_t\mathcal{F} &= \int\int\frac{\delta\mathcal{F}}{\delta\phi}\partial_t\phi dx\,dz = \\ &= \int\int\frac{\delta\mathcal{F}}{\delta\phi}\left[-\boldsymbol{v}\cdot\boldsymbol{\partial}\phi+\gamma\partial^2\left(\frac{\delta\mathcal{F}}{\delta\phi}\right)\right]dx\,dz = \\ &= -\gamma\left\langle\left[\partial\left(\frac{\delta\mathcal{F}}{\delta\phi}\right)\right]^2\right\rangle\Omega - \int\int\left(\frac{\delta\mathcal{F}}{\delta\phi}\right)v_i\partial_i\phi\,dx\,dz = \\ &= -\gamma\left\langle\left[\partial\left(\frac{\delta\mathcal{F}}{\delta\phi}\right)\right]^2\right\rangle\Omega - \Lambda\int\int\left[(-\partial^2\phi)+\frac{\phi^3-\phi}{\varepsilon^2}\right]v_i\partial_i\phi\,dx\,dz = \\ &= -\gamma\left\langle\left[\partial\left(\frac{\delta\mathcal{F}}{\delta\phi}\right)\right]^2\right\rangle\Omega - \Lambda\,\langle e_{ij}(\partial_i\phi)(\partial_j\phi)\rangle\,\Omega \quad . \end{aligned} \tag{4.15}$$

i.e.,

$$\partial_t E_{\mathcal{F}} = -\gamma \left\langle \left[ \partial_i \left( \frac{\delta \mathcal{F}}{\delta \phi} \right) \right]^2 \right\rangle - \Lambda \left\langle e_{ij} \left( \partial_i \phi \right) \left( \partial_j \phi \right) \right\rangle \quad . \tag{4.16}$$

where we have introduced the strain tensor $e_{ij} \equiv \left( \partial_i v_j + \partial_j v_i \right) / 2$ and assumed boundary conditions suitable to justify integrations by parts.
The energy balance takes then the form:

$$\partial_t (E_K + E_P + E_{\mathcal{F}}) = -\rho_o \nu \left\langle (\partial_i \boldsymbol{v})^2 \right\rangle - \gamma \left\langle \left[ \partial_i \left( \frac{\delta \mathcal{F}}{\delta \phi} \right) \right]^2 \right\rangle \quad . \tag{4.17}$$

The global system in thus intimately dissipative, even for a vanishing kinetic viscosity.
It is worth emphasising the cancellation of $\Lambda \langle e_{ij} (\partial_i \phi) (\partial_j \phi) \rangle$ by the kinetic and the free-energy contributions, due to exchanges between the velocity field and the interface.

### 4.2.4 Dispersion relation for the phase-field model

The aim of this section is to show that the well-known dispersion relation for gravity-capillary waves [39] can be easily obtained within the phase-field formalism. To do that, let us concentrate our attention on a two-dimensional problem and indicate by $z$ the gravity direction. Moreover, we will assume heavier fluid to be placed below the lighter one, in a way to have a stable situation. For a given perturbation imposed to the interface, the problem is to determine how the perturbation evolves in time.
Denoting by $h(x,t)$ a small perturbation imposed to a planar interface, we can rewrite $\phi$ as:

$$\phi = f \left( \frac{z - h(x,t)}{\varepsilon} \right) \quad , \tag{4.18}$$

where $h$ can be larger than $\varepsilon$, yet it has to be smaller than the scale of variation of $h$ (small amplitudes).
From the condition of local equilibrium one gets:

$$f'' = V'(f) \quad , \tag{4.19}$$

where $V(\phi) = (\phi^2 - 1)^2 / 4\varepsilon^2$. Under the above conditions the expression for the chemical potential $\mathcal{M}$ is:

$$\mathcal{M} = -\Lambda \frac{\partial^2 f}{\partial x^2} = \frac{\Lambda}{\varepsilon} \left[ f' \frac{\partial^2 h}{\partial x^2} - \frac{f''}{\varepsilon} \left( \frac{\partial h}{\partial x} \right)^2 \right] \quad . \tag{4.20}$$

Linearizing Eq. (4.6) for small interface velocity we have, neglecting the viscous term:

$$\rho_o \partial_t w = -\partial_z p - \phi \partial_z \mathcal{M} - \mathcal{A} g \rho_o \phi \quad . \tag{4.21}$$

The integration in the vertical direction interpreted in the principle value sense:

$$q_z \equiv \lim_{L \uparrow \infty} \int_{-L}^{L} w \, dz \quad , \tag{4.22}$$

$$\rho_o \partial_t q_z \equiv \lim_{L \uparrow \infty} \left\{ \frac{\Lambda}{\varepsilon} \int_{-L}^{L} \left[ f f'' \frac{\partial^2 h}{\partial x^2} - \frac{1}{\varepsilon} f f''' \left( \frac{\partial h}{\partial x} \right)^2 \right] d(z/\varepsilon) - \mathcal{A} g \rho_o \int_{-L}^{L} f dz \right\} \tag{4.23}$$

yields:

$$\rho_o \partial_t q_z = \sigma \frac{\partial^2 h}{\partial x^2} - 2\mathcal{A} g \rho_o h \quad . \tag{4.24}$$

having used the relations $\int (f')^2 dz = 2\sqrt{2}/3$, $\int f f''' dz = 0$ and

$$\lim_{L \uparrow \infty} \int_{-L}^{+L} f dz = +2h \quad . \tag{4.25}$$

The height variation of the interface has to match the vertical fluid velocity, thus giving:

$$\partial_t h = w(x, h(x,t), t) \equiv w^{(int)}(x,t) \quad . \tag{4.26}$$

The last step is to relate the velocity at the interface with the integral $q_z$. This is done by restricting to potential flows:

$$\boldsymbol{v} = \boldsymbol{\partial} \psi \qquad \partial^2 \psi = 0 \quad . \tag{4.27}$$

For $z > 0$, denoting with "$\hat{}$" the Fourier Transform, we have:

$$\psi(x,z,t) = \int_0^\infty e^{-kz+ikx} \hat{\psi}(k,t) dk + \text{c.c.} \tag{4.28}$$

$$w(x,z,t) = -\int_0^\infty k e^{-kz+ikx} \hat{\psi}(k,t) dk + \text{c.c.} \tag{4.29}$$

$$q_z(x,t) = -2\int_0^\infty e^{ikx} \hat{\psi}(k,t) dk + \text{c.c.} \tag{4.30}$$

$$w^{(int)} = -\int_0^\infty k e^{ikx} \hat{\psi}(k,t) dk + \text{c.c.} \quad . \tag{4.31}$$

Therefore:

$$\hat{w}^{(int)} = \frac{k \hat{q}_z}{2} \quad . \tag{4.32}$$

so that in $k-$space we have:

$$\partial_t \hat{h} = \frac{k \hat{q}_z}{2} \qquad \rho_o \partial_t \hat{q}_z = (-\sigma k^2 - 2\mathcal{A} g \rho_o) \hat{h} \quad . \tag{4.33}$$

From these two equations one immediately gets:

$$\partial_t^2 \hat{h} + \omega^2 \hat{h} = 0 \quad , \tag{4.34}$$

with:

$$\omega^2(k) = \mathcal{A} g k + \frac{\sigma}{2\rho_o} k^3 \tag{4.35}$$

that is the expected dispersion relation [39]. For the stable configuration we have, for all values of $\sigma$: $\mathcal{A} g k + \sigma / (2\rho_o) k^3 > 0$, i.e. any initially imposed perturbation will not grow indefinitely.
From Eq. (4.34) and the initial condition:

$$\partial_t \hat{h}(k,t) = 0 \quad \text{at } t = 0 \quad , \tag{4.36}$$

we immediately have:

$$\hat{h}(k,t) = \hat{h}(k,0)\cos(\omega t) \quad , \tag{4.37}$$

and the velocity at the interface reads:

$$\hat{w}^{int}(k,t) = -\hat{h}(k,0)\omega\sin(\omega t) \quad . \tag{4.38}$$

Assuming an initial perturbation of the form $h(x,0) = h_0\cos(\bar{k}x)$ from Eqs. (4.31) and (4.38) we obtain:

$$\hat{\psi}(\bar{k},t) = \frac{1}{\bar{k}}\hat{h}(\bar{k},0)\omega\sin(\omega t) \quad , \tag{4.39}$$

and the velocity components, for $z > 0$:

$$w^{\uparrow}(x,z,t) \equiv w(x,z,t) = -\cos(\bar{k}x)e^{-\bar{k}z}h_o\omega\sin(\omega t) \tag{4.40}$$

$$u^{\uparrow}(x,z,t) \equiv u(x,z,t) = \sin(\bar{k}x)e^{-\bar{k}z}h_o\omega\sin(\omega t) \quad , \tag{4.41}$$

where we used the relation $h_0 = 2\hat{h}(k,0)$.
For $z < 0$, in a similar way we obtain the velocity field components:

$$w^{\downarrow}(x,z,t) \equiv w(x,z,t) = -\cos(\bar{k}x)e^{+\bar{k}z}h_o\omega\sin(\omega t) \tag{4.42}$$

$$u^{\downarrow}(x,z,t) \equiv u(x,z,t) = -\sin(\bar{k}x)e^{+\bar{k}z}h_o\omega\sin(\omega t) \quad . \tag{4.43}$$

When in the initial configuration the heavier fluid placed above the lighter one, the dispersion relation (4.35) transforms in:

$$\omega^2(\bar{k}) = -\mathcal{A}g\bar{k} + \frac{\sigma}{2\rho_o}\bar{k}^3 \quad , \tag{4.44}$$

which is readily obtained by flipping the sign of $g$. For $\sigma < \sigma_c \equiv 2\rho_o/(\mathcal{A}g\bar{k}^2)$ surface tension is not able to contrast gravity-induced vertical motion with the final result that amplitude perturbations grows exponentially: the flow is unstable. More precisely, from relation (4.44) and for $\sigma < \sigma_c$ we have:

$$\omega(\bar{k}) = \sqrt{-\mathcal{A}g\bar{k} + \frac{\sigma}{2\rho_o}\bar{k}^3} \equiv i\,n(\bar{k}) \quad , \tag{4.45}$$

and Eqs. (4.40)-(4.43) transform in:

$$w^{\uparrow}(x,z,t) \equiv w(x,z,t) = \cos(\bar{k}x)e^{-\bar{k}z}h_0\,n\,\sinh(n\,t) \tag{4.46}$$

$$u^{\uparrow}(x,z,t) \equiv u(x,z,t) = -\sin(\bar{k}x)e^{-\bar{k}z}h_0\,n\,\sinh(n\,t) \quad , \tag{4.47}$$

for $z > 0$, and:

$$w^{\downarrow}(x,z,t) \equiv w(x,z,t) = \cos(\bar{k}x)e^{+\bar{k}z}h_0\,n\,\sinh(n\,t) \tag{4.48}$$

$$u^{\downarrow}(x,z,t) \equiv u(x,z,t) = \sin(\bar{k}x)e^{+\bar{k}z}h_0\,n\,\sinh(n\,t) \quad , \tag{4.49}$$

for $z < 0$.

## 4.3 Numerical investigation

In this section we report the results obtained exploiting Direct Numerical Simulations (see page 13) of the phase-field model for the Rayleigh–Taylor problem described in the preceding sections. Our attention is focused both on the linear phase of the perturbation evolution and on the weakly nonlinear regime governed by plumes, for $\mathcal{A} \ll 1$.
In the present study, as for the investigation of miscible configuration (see Chap. 2) we consider initial perturbations imposed to the interface varying along one of the horizontal directions, say the $x$ axis, and invariant along the other horizontal direction, say the $y$ axis. The perturbation is thus intimately two-dimensional a fact that allows our to solve the original Navier–Stokes equation coupled to the phase-field in two dimensions. This clearly permits to obtain high accuracy and thus to properly test the phase-field approach against known results for both the linear and the nonlinear evolution stage.
For a two-dimensional flow it is convenient to introduce the vorticity field $\omega$ [$\omega = (\boldsymbol{\partial} \times \boldsymbol{v})_y$] and study the equations:

$$\partial_t \omega + \boldsymbol{v} \cdot \boldsymbol{\partial} \omega = \nu \partial^2 \omega - \frac{\Lambda}{\rho_o} \boldsymbol{\partial} \times \left( \partial^2 \phi \, \boldsymbol{\partial} \boldsymbol{\phi} \right) - \mathcal{A} \left( \boldsymbol{\partial} \phi \right) \times \boldsymbol{g} \tag{4.50}$$

$$\partial_t \phi + \boldsymbol{v} \cdot \boldsymbol{\partial} \phi = \gamma \partial^2 \mathcal{M} = \gamma \, \Lambda \partial^2 \left[ -\partial^2 \phi + \frac{\left( \phi^3 - \phi \right)}{\varepsilon^2} \right] \quad . \tag{4.51}$$

By exploiting a pseudospectral method (see, for details App. B) periodic buondary conditions have to be assumed along the two directions. Along the vertical direction this choice deserves some comments. As initial condition we started from the hyperbolic-tangent profile, Eq. (4.3), for $\phi$ with the interface placed in the middle of the domain. The fact that we have periodic boundary conditions along $y$ simply means that far from the middle of the domain the hyperbolic-tangent profile has to be distorted in order to satisfy periodic boundary conditions. However, both in the linear and in the weakly nonlinear regimes the amplitude of the interface perturbation is always much smaller than the vertical size of the box, so that the actual choice of boundary conditions at the top and bottom can be safely neglected. More quantitatively, as the perturbation grows, here we use the empirical criterion in according to which the ratio of bubble/spike height to the vertical dimension of the domain is always smaller than $\sim 0.2$. Test cases with smaller ratios do not produce appreciable differences in the results we are going to discuss (for the weakly nonlinear case see Fig. 4.7).
The box has a horizontal to vertical aspect ratio $L_x/L_z = 1$ for the linear analysis stage and $L_x/L_z = 1/2$ for the weakly nonlinear evolution ($L_x/L_z = 1/4$ for the test case reported in Fig. 4.7). In the weakly nonlinear case, we take a smaller aspect ratio owing to the fact that the perturbation can reach a higher amplitude (with respect to the case of the linear analysis).
As far as the resolution is concerned, it is $1024 \times 1024$ collocation points for the case $L_x/L_z = 1$ and $1024 \times 2048$ for $L_x/L_z = 1/2$. We need such a high resolution (despite the fact that we focus on a linear and weakly nonlinear study) in order to have a well described interface separating the two phases. In our simulations the mixing width ($\sim 4\,\varepsilon$) is 6 mesh points.
The physically relevant parameters in the present problem are the kinematic viscosity $\nu$, the buoyancy intensity $\mathcal{A}g$ and the surface tension $\sigma$. Both $\mathcal{A}g$ and $\nu$ will be varied in our study,

while $\sigma$ will be kept fixed to a fixed value (see below). The surface tension is related to the ratio $\Lambda/\varepsilon$ with $\varepsilon$ (and thus $\Lambda$) sufficiently small in order to have a finite value for the surface tension and, at the same time, to reproduce the correct sharp-interface limit. Finally, the parameter $\gamma$ appearing in the relaxation term in Eq. (4.51) must satisfy the requirement that $\gamma\Lambda$ be small, so as to enforce 'instantaneous' local equilibrium between flow and interface. Here we used the value (model units) $\gamma\Lambda = 10^{-8}$.

All simulations presented here start from an initial condition corresponding to an equilibrium configuration: velocity identically zero and hyperbolic tangent profile for the phase-field $\phi$, expressed by the relation of the form: $\tanh\left((z - h(x, t = 0))/\sqrt{2}\varepsilon\right)$ with

$$h(x, \mathrm{t} = 0) = h_0 \sin(k\, x) \quad .$$

For a given $k$ we choose the initial amplitude $h_0$ in a way that $h_0 \,/\, \lambda$ (where $\lambda \equiv 2\pi/k$) is sufficiently small to fall in the linear phase (i.e. $h_0 \,/\, \lambda \ll 1$) and $h_0$ is sufficiently large for the wave disturbance to see an almost infinitesimal mixing width (i.e. $h_0 \,/\, \varepsilon \gg 1$). Specific numerical values are reported in the next sections.
On page 46 a qualitative idea of time evolution of phase field is shown.

### 4.3.1 Linear instability for negligible viscosity

The aim of this section is to verify the growth-rate (4.45) which holds in the linear phase when the viscosity is negligible.
In order to do so, we take a small value of $\nu$ ($\nu = 10^{-5}$ in the model units) and vary $k$ (up to $k_c \equiv (2\mathcal{A}g\rho_o/\sigma)^{1/2}$, the critical wave-number separating unstable from stable wave-modes) and $Ag$ and take a fixed value of $\sigma$. The ratio $h_0 \,/\, \lambda = 0.06$ while $h_0 \,/\, \varepsilon$ ranges from $\sim 10$ to $\sim 40$ in the range of $k$ considered.
The behaviour of the square growth-rate $n^2$ (see Eq. (4.45)) is shown in dimensionless form in Fig. 4.2 as a function of $k$ for three different values of $k_c$ (obtained by varying $Ag$) and in Fig. 4.3 by varying $Ag$ for three different values of $k < k_c$. In both figures, symbols refer to the numerical results and the dashed line is the theoretical expectation given by (4.45).
The numerical data in Figs. 4.2 and 4.3 have been obtained via best-fit of $\langle w^2 \rangle$, the spatial average of $w^2$ as a function of time. The latter average is computed over a horizontal strip containing the interface (placed in the middle of the computational domain) and having an extension of $a_z$ above and below the interface. This has been done to avoid spurious contaminations coming from the upper and lower domain regions affected by the boundary conditions. In formulae:

$$\begin{aligned}\langle w^2 \rangle = \frac{1}{2a_z}\frac{1}{L_x}\int_{-a_z}^{0} dz \int_0^{L_x} dx \left(w^{\downarrow}\right)^2 + \frac{1}{2a_z}\frac{1}{L_x}\int_0^{a_z} dz \int_0^{L_x} dx \left(w^{\uparrow}\right)^2 \\ = \frac{1}{2\,a_z\,k}\left[-e^{-2\,k\,a_z} + 1\right] n^2 h_0^2 \sinh^2(n\,t) \quad , \quad (4.52)\end{aligned}$$

where we used the expression (4.46) and (4.48) for $w^{\uparrow}$ and $w^{\downarrow}$, respectively.
The best fit has been done with $n$ as unique free parameter and its high accuracy can be verified in Fig. 4.4 where we show the time evolution of $\langle w^2 \rangle$ for $k_c = 4.7$ (solid triangles in Fig. 4.2) and for four values of $k$ smaller than $k_c$. At $t\,n > 1.5$ nonlinear effects start

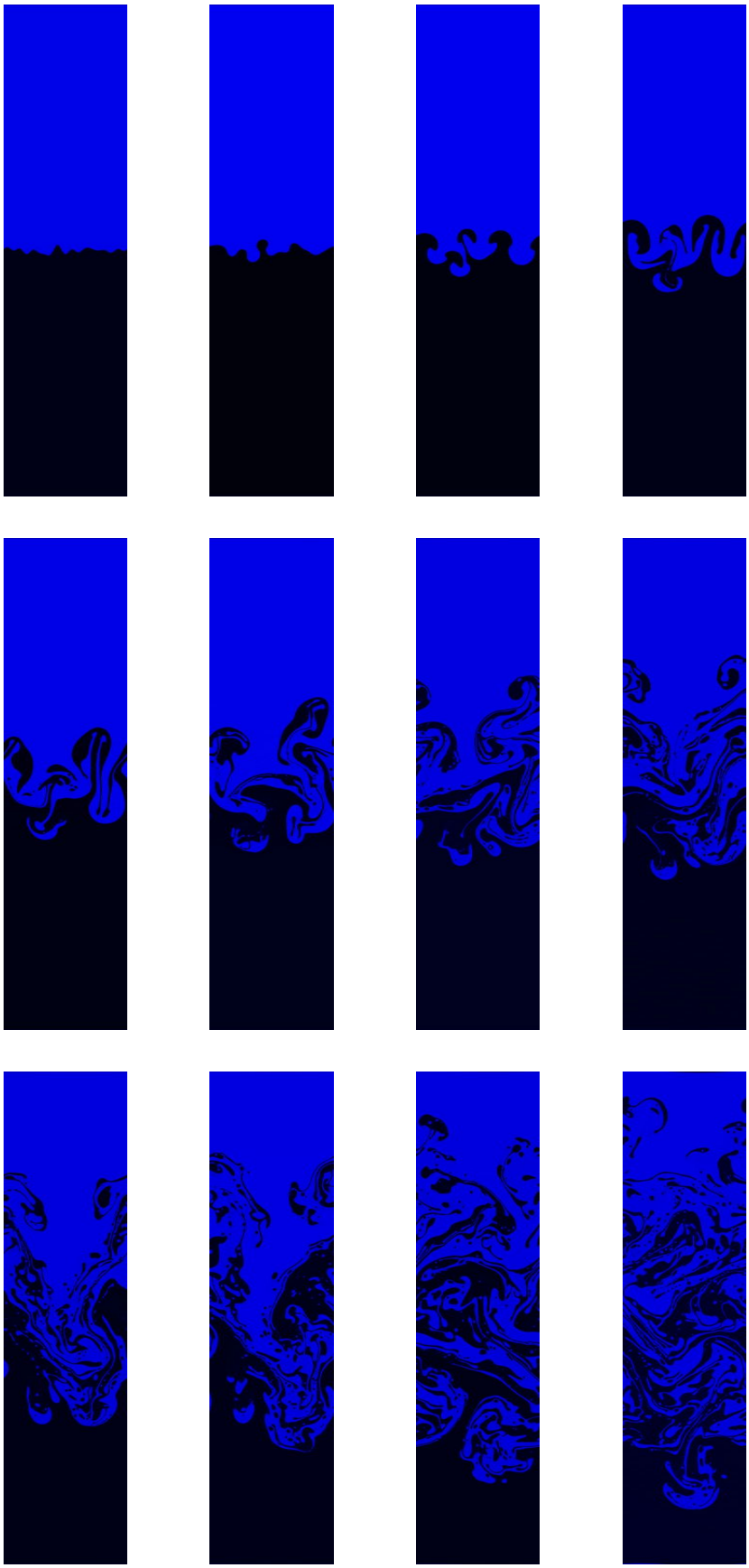

**Table 4.1:** Time evolution of immiscible Rayleigh–Taylor instability. A phase-field snapshots: blue (black) corresponds to $\phi = -1$ ($\phi = 1$).

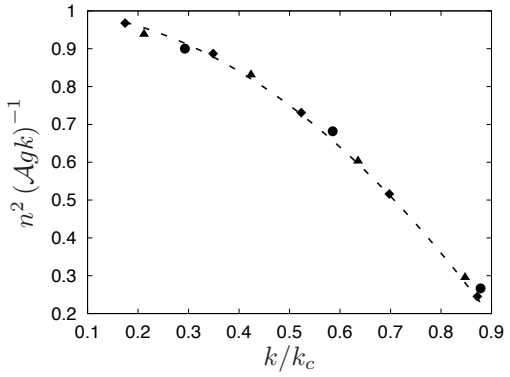


**Figure 4.2:** The square growth-rate $n^2$ (see Eq. (4.45)) for three different values of $\mathcal{A}g$ corresponding to three different values of the critical wave number $k_c \equiv (2\mathcal{A}g\rho_o/\sigma)^{1/2}$: $k_c = 3.4$ (solid circles), $k_c = 4.7$ (solid triangles) and $k_c = 5.7$ (solid rhombus). The dashed line is the linear-theory prediction expressed by the relation (4.45).

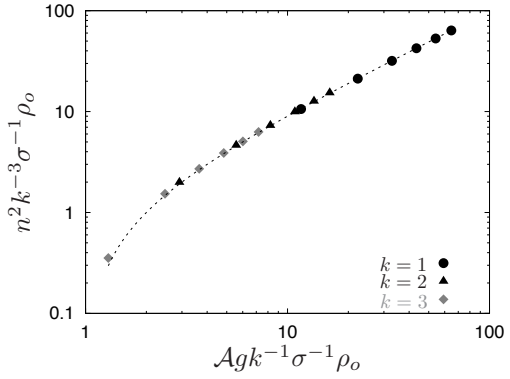


**Figure 4.3:** The square growth-rate $n^2$ (see Eq. (4.45)) for $k = 1$ (solid circles), $k = 2$ (solid triangles) and $k = 3$ (solid rhombus), all smaller than $k_c$, for six different values of $\mathcal{A}g$ ranging from $0.11$ to $0.61$. The dashed line corresponds to the linear-theory prediction.

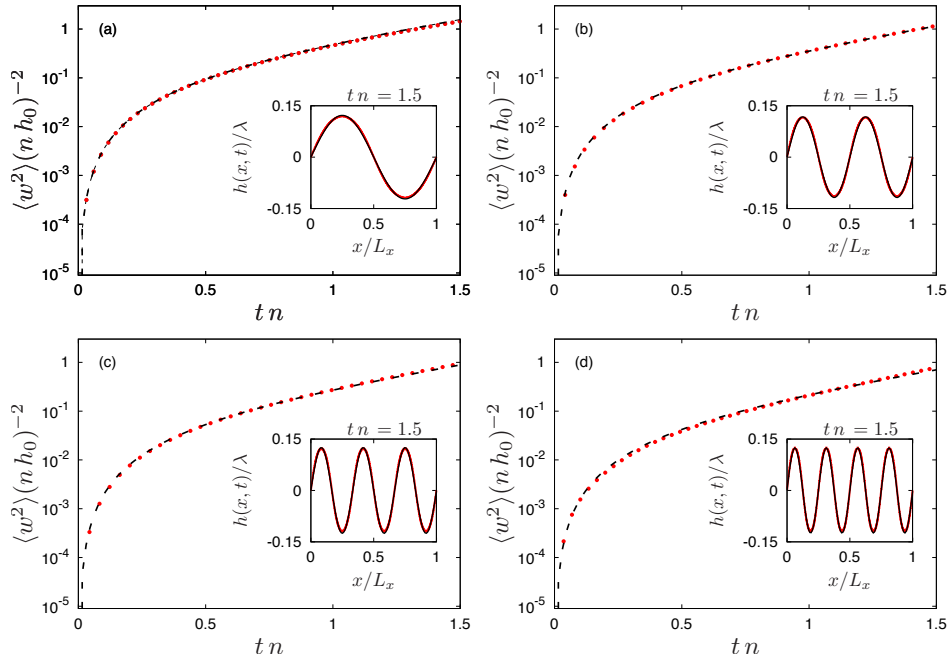


**Figure 4.4:** Time behaviour of $\langle w^2 \rangle$ for $k_c = 4.7$ (in Fig. 4.2 corresponding to the solid triangle) and for four values of $k < k_c$. (a) $k = 1$, (b) $k = 2$, (c) $k = 3$ and (d) $k = 4$. The numerical results (symbols) are compared with the corresponding best fit expressions (see the text for details). In the insets the interface perturbation, $h(x,t)$, is plotted at $t\,n = 1.5$ revealing a very accurate linear analysis prediction.

to enter into play giving rise to corrections to the linear analysis (see Sec. 4.3.4). Up to that time, linear theory is very accurate as one can also realise by looking at the insets of Fig. 4.2 where the sinusoidal form of $h(x,t)$ is reported for $t\,n = 1.5$. For testing purposes, for $k = 2$ we have performed a simulation having a computational domain twice (and the same for the resolution along the vertical) the one considered in Fig. 4.4. The results turned out to be indistinguishable with respect to that reported in Fig. 4.4.

### 4.3.2 Linear instability for finite viscosity

The aim of this section is to investigate numerically how the growth-rate, $n$ appearing in Eqs. (4.46)-(4.49), is modified by viscosity. As discussed in Sec. 1.2.1, both an upper and a lower bound for the perturbation growth-rate are known (see Eqs. (1.6) and (1.7)) and we want to assess how the actual growth-rates compare with those.

For such purpose, we choose a surface tension, $\sigma$, and $\mathcal{A}g$ in such a way to obtain instability for few (unstable) wavenumbers. Our choice was $k_c = 5.7$ (see Sec. 4.3.1) thus corresponding to 5 unstable wavenumbers.

As far as the initial perturbation is concerned, we report here the case corresponding to $k = 1$. Initial perturbations with a larger wavenumber simply need an initial smaller amplitude (and eventually a larger numerical resolution) in order to satisfy $h_0 \gg \varepsilon$ and $h_0 \ll \lambda$. Here, we have $h_0/\lambda = 0.03$ and $h_0/\varepsilon \sim 20$. Such ratios turned out to be sufficiently 'asymptotic' to produce accurate results. The effect of viscosity is studied by considering twelve values of viscosity in the range $10^{-5} \leq \nu \leq 5\ 10^{-2}$ (model units).

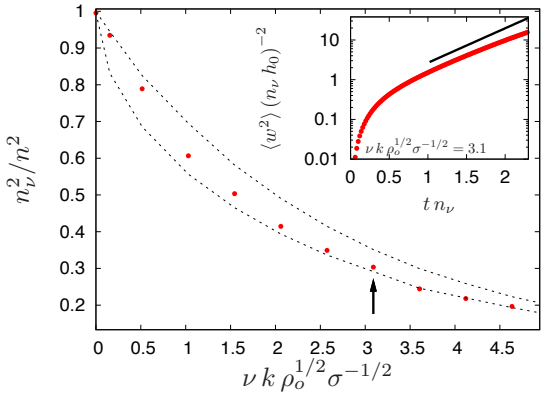


**Figure 4.5:** Behaviour of the dimensionless perturbation growth-rate, $n_\nu$, for $k = 1$ and $\mathcal{A}g$ corresponding to $k_c = 5.7$. Dotted lines correspond to upper and lower bounds for the growth-rate (see Eqs. (1.7) and (1.6)). The arrow selects a value of the viscosity for which the time evolution of $\langle w^2\rangle$ is reported in the inset. The continuous line is the best fit slope (see text).

The results of our simulations are summarised in Fig. 4.5 where the behaviour of the square perturbation growth-rate, $n_\nu^2$, is shown as a function of viscosity. The numerical predictions have been compared with the available theoretical bounds (dashed lines).
Note that the numerical points are always in between the two bounds and also how the relative differences between the upper bound and the numerical values are $< 11\%$. This latter fact is compatible, for example, with the results of [99].
The value of the growth-rates have been obtained via best of $\langle w^2\rangle$ (see Eq. (4.52)). Unlike what we did in previous section, here we perform the fit within the exponential region. The reason is that the non-asymptotic form of the perturbation time-evolution is unknown in the present case.

The fit accuracy can be appreciated in the inset of Fig. 4.5 where the temporal evolution of the perturbation for $\nu = 0.3$ (model units) is shown together with the best fit slope (dashed line) from which $n_\nu$ is determined. Error bars, estimated by looking at the fit sensitivity by varying the length of the fit interval, are of the order of the symbol sizes.

### 4.3.3 Stable configuration: gravity-capillary waves

The performance of the phase-field approach in the unstable regime predicted by linear theory both in the presence and in the absence of viscosity proved to be very good. As discussed in Sec. 4.2.4, for sufficiently large surface tensions and/or sufficiently small differences between fluids density, a perturbation initially imposed to the fluid interface may maintain its initial amplitude giving rise to the dispersion relation (4.35). The waves resulting from the balance between gravity and surface tension are known as gravity-capillary waves. Our aim here is to verify their dispersion relation.
To do that, we have fixed the parameters to obtain a critical wavenumber of order one. For $\mathcal{A}g = 0.008$ (model units) and the same $\sigma$ as in the unstable case, one has $k_c = 0.9$. The first accessible wavenumber is thus stable and the disturbance should evolve in time according to (4.37). However, the geometrical/computational configuration used in the unstable case

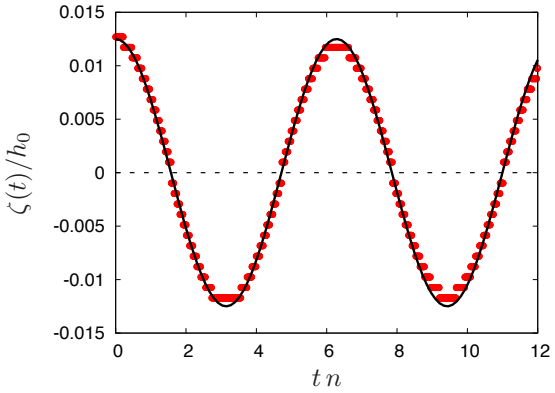


**Figure 4.6:** Time behaviour of the perturbation maximum, $\zeta(t)$, for $k = 1$ and $h_0/\lambda = 0.012$. The critical wave number is $k_c = 0.9$. Numerical results (symbols) are compared with the prediction from linear theory.

did not produce sufficiently accurate results. In particular, using the same domain aspect ratio $L_x/L_z = 1$ and the same ratio between perturbation amplitude and perturbation wave-length we found a dynamics too dissipative with respect to what is expected. In the absence of viscosity, dissipation arises in the phase-field formulation due to the sole contribution proportional to $\gamma$ in Eq. (4.17). The latter parameter has been taken sufficiently small to ensure a negligible effects inside a period of oscillation. The specific value was $\gamma = 6.25 \times 10^{-5}$. To avoid spurious dissipation, as that induced by nonlinear effects, we reduced the amplitude of the initial perturbation with respect to the unstable case. Also, we increased the size of the periodicity box along the gravitational direction in a way to reduce possible spurious contribution arising from the upper/lower part of the computational domain where instabilities, not present in the unstable case, might now develop. The above choice on the amplitude of the initial perturbation implies a consequent reduction of $\varepsilon$. The following set of parameters have been used: $\varepsilon = 0.008$ , $L_x/L_z = 1/4$ and a resolution $Nx \times Nz$ of $256 \times 4096$. For an initial perturbation on $k = 1$, its initial amplitude $h_0$ has been chosen to have $h_0/\lambda = 0.012$ and $h_0/\varepsilon \sim 10$. The behaviour of the maximum, $\zeta(t)$, of the initial perturbation is shown as a function of time in Fig. 4.6. The continuous line is relative to a sinusoidal with pulsation $\omega$ obtained from (4.35). The agreement between theory and numerics is satisfactory both for the amplitude and for the pulsation. Note the small reduction of $\zeta(t)$, in one oscillation period: only 1 grid box over 4096.

### 4.3.4 Weakly nonlinear stage

In this section we investigate the early stages of the nonlinear dynamics. We focus on the rising/falling velocity of plumes in the limit of small Atwood numbers when spikes and bubbles are known to coincide. The theoretical prediction for the terminal velocity is reported in Sec. 1.3. Our aim here is both to verify the existence of a regime characterised by a constant 'terminal' velocity and, secondly, to compare the prediction (1.9) for such terminal velocity with our numerical data.

The physical parameters are chosen to magnify the effect of the surface tension on the terminal velocity. This happens when the wavenumber $k$ of the initial perturbation (still supposed unimodal) is slightly below $k_c$. Here we choose $\mathcal{A}g$ and $\sigma$ such that $k_c = 4.004$

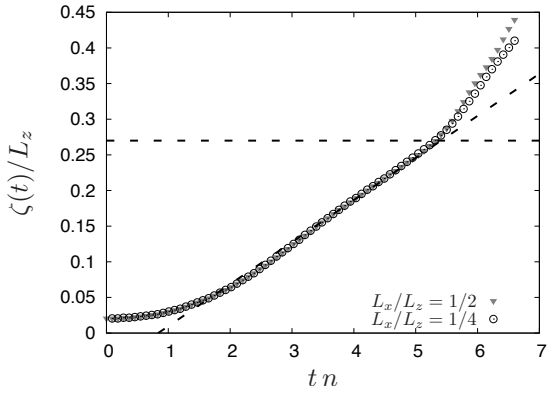


**Figure 4.7:** Time evolution of amplitude perturbation $\zeta(t)$. Symbols are our numerical results for two different domain heights (with the same horizontal extension $L_x = 2\pi$): gray triangles correspond to $L_z = 4\pi$; black circles to $L_y = 8\pi$. $\zeta(t)$ is made dimensionless with the smallest $L_y$. Dashed lines are the theoretical slope given by Eq. (1.9) and the value $\zeta(t)/L_z = 27\%$ respectively. Note the agreement between the two numerical results up to $\zeta(t)/L_z \sim 27\%$.

and thus look at the dynamics associated to the wavenumber $k = 3$. The initial perturbation has an amplitude $h_0/\lambda = 0.06$; the initial dynamics is thus linear. Although we are interested to investigate the case of zero viscosity, in order to prevent numerical instabilities we add a small viscosity $\nu = 2 \times 10^{-5}$ (model units). In Fig. 4.7 the perturbation amplitude is shown as a function of time: symbols correspond to our numerical data (for two different domain heights) and dashed lines are the theoretical slope given by (1.9) and the value $\zeta/L_z = 0.27$ respectively. A good agreement is found between numerics and theory in the range $3 < t\,n < 5$. At larger times, neighbouring plumes start to interact and the arguments leading to (1.9) do not apply any longer. Notice also as up to $t\,n \sim 5$ (corresponding to $\zeta/L_z \sim 0.27$) the numerical results obtained with two different domain heights are almost indistinguishable. This is a strong evidence of smallness of the effect played by periodic boundary conditions along the vertical. In Fig. 4.8 we show some snapshots of the time evolution of the two fluids within the weakly nonlinear stage. Figures are equally spaced in time in the interval $3 < t\,n < 5$. Black corresponds to $\phi = -1$; white to $\phi = 1$. Their shape is similar to that experimentally observed by [141] (see Fig. 1.4). Note the aforementioned spike/bubble symmetry corresponding to the up-down symmetry of our original evolution equations.

## 4.4 Conclusions and perspectives

In this chapter we show that the phase-field model provides a valuable numerical instrument for the study of immiscible, convective hydrodynamics. As a testground for this model, we consider the RT instability. Numerical results compare very well with known analytical results both for the linearly stable and unstable cases, and for the weakly nonlinear stages of the latter. All these results are very encouraging in view of the next important step that is the numerical simulations of immiscible RT turbulence. There, the interplay of all the fundamental mechanisms that we illustrate here (instabilities and wave propagation) is expected to give rise to a small-scale emulsion-like phase dominated by gravity-capillary waves

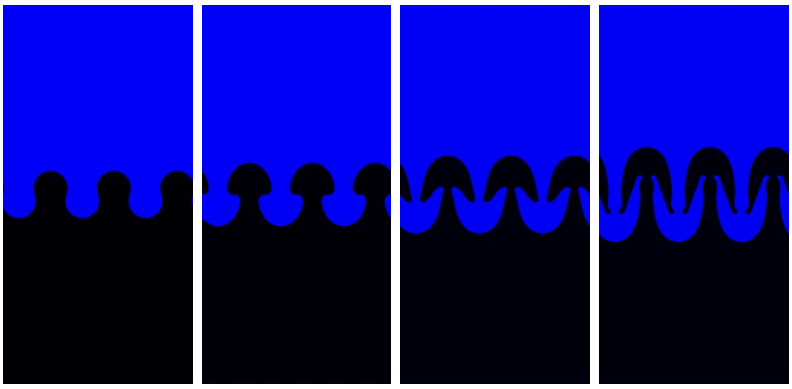

**Figure 4.8:** A phase-field snapshot: blue (black) corresponds to $\phi = -1$ ($\phi = 1$). Frames (corresponding to the domain height $L_y = 4\pi$) are equally spaced in time in the interval $3 < t\,n\, < 5$ (see also Fig. 4.7).

and by a large-scale hydrodynamic range of scales where classical Kolmogorov turbulence should appear. This theoretical suggestion still awaits numerical confirmation, and the phase-field model provides the appropriate method to pursue this goal.

# Chapter 5

# Viscoelastic Rayleigh–Taylor instability

*"... Dr. Breed was mistaken about at least one thing: there was such a thing as ice-nine. And ice-nine was on earth..."*

Cat's Cradle by Kurt Vonnegut (1963)

In this chapter we consider the effect of viscoelasticity on the early stage of RT instability. Here, viscoelasticity is generated by adding polymers to the original Newtonian fluid in a way to obtain a very dilute (few parts per million in mass) viscoelastic solution. It is a well-known fact that polymers are able to strongly modify the stability of laminar flows. By virtue of the fact that the control of instability in RT system is an issue of paramount importance, we address here the question on whether or not polymers act to increase the efficiency of the mixing. This analysis is motivated both from a purely fundamental point of view (related to the basic mechanisms of interaction between fluid and polymers) and from more applied ones related to find out efficient ways to produce mixing of different fluids.

This chapter is organised as follows. Introductory Sec. 5.1 recalls the main features of polymers. At first, we summarise the main phenomena in the presence of polymers. Afterwards the basic dynamics of polymers in fluids is introduced: starting from a microscopic description in terms of single polymer dynamics, full hydrodynamics models that are typically used to describe viscoelastic solutions are constructed. For an introduction see, for instance, [13, 102].
In the following sections, we add the polymer to the RT system and we show our preliminary results about the addition effects on the instability evolution. In Sec. 5.2 the immiscible configuration is considered and the equations ruling the fluid evolution are introduced. Sec. 5.2.1 is focused on the linear-growth rate by analytical calculation in the phase-field formulation (introduced in Chap. 4). Regarding the linear regime, the first preliminary numerical results are showed in Sec. 5.2.1.1. Finally, in Sec 5.3 we mention to our future investigations.

## 5.1 Polymer solutions: a brief introduction

Polymers are molecules composed by a large number of repeating units, the monomers, joined by chemical bonds to form a long chain. Both natural and synthetic polymers exist.

**(a)** **(b)**

**Figure 5.1:** Two phenomena which give an idea of the different response of Newtonian and viscoelastic fluids. **(a)** Weissenberg effect. When a Newtonian fluid is put in rotation, it is pushed away from the centre by a centrifugal force and a dip appears on the free surface, which takes the shape of a paraboloid. On the contrary, when a rotating rod is inserted in a tank filled with a viscoelastic fluid, the fluid tends to climb up the rod. See, for instance, `http://www.youtube.com/watch?v=npZzlgKjs0I&NR=1`. **(b)** Non-dilute solution of polymers: water and cornstarch. The solution approximately behaves as a Newtonian fluid, if the stress applied on its surface is slow, otherwise as a solid, if the stress applied on its surface is impulsive. As a consequence, it is possible to jump on the surface, as shown in the photo! (Courtesy of Marco Tizzi). See also `http://www.youtube.com/watch?v=IRlBuZsScho`.

Examples of the first type are DNA, proteins, starches, cellulose, latex. Synthetic polymers are commercially produced for a huge variety of uses; among these, we find all the materials commonly called plastics.

It is known since the 1940's that the addition of small amounts of polymers to fluid can produce dramatic changes of its properties. A solution of polymers manifests in a variety of spectacular phenomena. Some examples are shown in Fig. 5.1.

The ability of polymers to considerably change to large-scale statistics of the advecting flow has important practical applications, drag reduction being one of the most relevant ones. Since the work of the chemist Toms [139] in 1949, it is know, and actually exploited for industrial purposes (like oil transport in submarine ducts), that adding small quantities of polymers (few parts per million in mass) can reduce the turbulent drag up to $80\%$. Many theories have been proposed to explain what is the basic physical mechanism of the drag reduction phenomenon [11, 50, 94, 95, 137] and experimental investigations have been carried out [2, 73, 135]. Despite the considerable number of studies, a quantitative fully satisfactory explanation of drag reduction is still lacking, and the phenomenological theory are not universally accepted [135]. It is interesting to note that most studies focused on dilute polymer solutions in channel or pipe geometry, where boundary effects are important, but recent experimental [2] and numerical [14, 19, 20] works have shown that polymers affect the turbulent flow even far from (or in the absence of) boundaries.

Besides, a remarkable phenomenon of recent experimental discovery [68–71] is the onset of elastic turbulence. This effect appears in the limit of vanishing Reynolds number. The

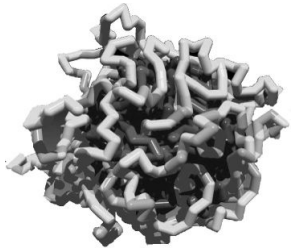

**Figure 5.2:** Sketch of the coiled equilibrium configuration of a polymer.

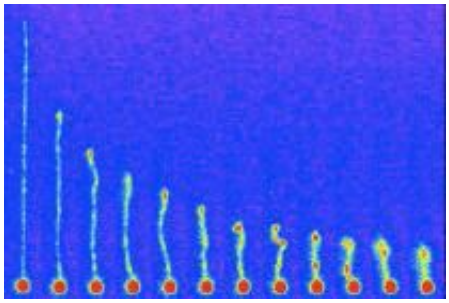

**Figure 5.3:** Single DNA molecule ($40\ \mu\mathrm{m}$) relaxing to the coiled state. In this experiment a latex bead ($1\ \mu\mathrm{m}$) is tethered to an end of the molecule. The DNA, coloured with a fluorescent dye, is stretched by a uniform flow and successively let free to relax. Images are taken at $5\ \mathrm{s}$ time intervals, from left to right [111].

presence of polymers modifies the stability of a laminar flow. Indeed, when stretched by a a primary shear flow, polymers can trigger elastic instability and finally, give rise to a state which displays features typical of turbulent flows, such as spatial and temporal irregular behaviour, with a broad range of active scales. The possibility of achieving turbulent states for arbitrarily small Reynolds numbers is clearly very important for mixing related to applications in microchannel flows [5, 70, 71], where mixing efficiency is limited by the practical difficulty of reaching large Reynolds number. Despite its wide technological interest, elastic turbulence is still poorly understood from a theoretical point of view.

The mechanism by which dilute polymer solutions can influence turbulent flows is the extreme extensibility of polymers. Polymers at equilibrium are coiled in a ball of radius $R_0$ of the order of $1\ \mu\mathrm{m}$, as sketched in Fig. 5.2.

In the presence of a non-homogeneous flow, the molecule is deformed in an elongated structure characterised by its end-to-end distance $R$ which can be significantly larger than $R_0$. The deformation of molecules is the result of the competition between the stretching induced by differences of velocities and the entropic relaxation of polymers to their equilibrium configuration. Experiments with DNA molecules (see Fig. 5.3) show that this relaxation is linear, provided that the elongation is small compared with the maximal extension $R \ll R_{max}$, and can be characterised by a typical relaxation time $\tau_\mathrm{p}$ [75].

A model which is very often used for its simplicity is the Dumbbell model [75], where the complex structure of the polymer molecule is replaced by a couple of beads of negligible mass, connected by a harmonic spring. The elastic constant of the spring is inversely proportional

to the typical polymer relaxation time $\tau_\mathrm{p}$ [17]. The evolution of the Dumbbell end-to-end vector $\boldsymbol{R} = \boldsymbol{x}_2 - \boldsymbol{x}_1$ is determined by different contributions: the hydrodynamic drag force, thermal noise, and the elastic restoring force of the spring. Moreover, in a non-homogeneous flow, polymers can also get stretched, because of different velocities of the two beads (see Fig. 5.4). Since in applications the typical size of polymers is smaller than the viscous scale of turbulence, as a good approximation stretching is due to velocity gradients. The equation of motion for the end-to-end polymer distance, $\boldsymbol{R}$, can be written as follows:

$$\frac{d\boldsymbol{R}}{dt} = (\boldsymbol{R}\cdot\boldsymbol{\partial})\boldsymbol{v} - \frac{1}{\tau_\mathrm{p}}\boldsymbol{R} + \sqrt{\frac{2R_0^2}{\tau_\mathrm{p}}}\boldsymbol{\xi} \quad . \tag{5.1}$$

On the r.-h.s., the first term is the stretching term, originating from the spatial variation of the flow experienced at $\boldsymbol{R}$, the second one is a relaxation contribution and $\boldsymbol{\xi}$ is a Brownian process with correlation $\langle \xi_i(t)\xi_j(t')\rangle = \delta_{ij}\delta(t-t')$ mimicking thermal noise effect on the polymer.

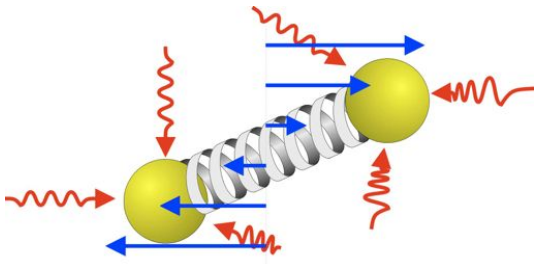

**Figure 5.4:** Sketch of the Dumbbell model. In this model a polymer is described as two beads connected by a spring. The beads represent the ends of the molecule and their separation is a measure of the extension. A non-homogeneous flow induces polymer deformation (blue arrows). Moreover the polymer experiences an elastic force due to the spring connection the two beads and a Brownian force due to thermal fluctuations (red arrows).

The relative importance between polymer relaxation and stretching is measured by the Weissenberg number $\mathcal{Wi}$, defined as the product of $\tau_\mathrm{p}$ and the characteristic velocity gradient. When $\mathcal{Wi} \ll 1$, relaxation is fast compared to the stretching time and polymers remain in the coiled state. For $\mathcal{Wi} \gg 1$, on the contrary, polymers are substantially elongated. The transition point is called the coil-stretch transition and occurs at $\mathcal{Wi} = O(1)$.
In the case of dilute solutions for which the polymer concentration $m$ satisfies $mR_0^3 \ll 1$, the influence of polymers in the coiled state on the fluid is negligible. Above the coil-stretch transition, polymers start to affect the flow. A simple linear viscoelastic model is the widely used Oldroyd-B model[1] [17], based on the Dumbbell model.

[1]The linear Oldroyd-B model is based on the assumption that polymers can be modelled as harmonic springs and, consequently, it allows infinite extension of polymer molecules. This is clearly unphysical because the polymer end-to-end separation $R$ is bounded by the maximum length $R_{max}$. When $R$ approaches $R_{max}$ elastic nonlinearities become important and the linear approximation fails. A more refined, but still conceptually simple description is the FENE-P model [17]. This model is able to reproduce features of polymer solutions not captured by Oldroyd-B model, like the shear thinning, i.e., the decrease of viscosity at increasing shear rates.

The transition from the microscopic behaviour of the single molecule to a macroscopic hydrodynamical description requires to get rid of the microscopic degrees of freedom such as the thermal noise. The macroscopic polymer behaviour can be described in term of the conformation tensor $\mathbb{S}$:

$$\mathbb{S}_{ij} = \frac{\langle R_i R_j \rangle}{R_0^2} \quad ,$$

where the average is taken over the thermal noise, or, equivalently, over a small volume containing a large number of molecules. By construction $\mathbb{S}$ is symmetric, positive definite, and its trace, $tr\mathbb{S}$, is a measure of the polymer elongation. The following evolution equation for $\mathbb{S}$ can be easily obtained:

$$\partial_t \mathbb{S} + \boldsymbol{v} \cdot \boldsymbol{\partial} \mathbb{S} = (\boldsymbol{\partial v})^T \cdot \mathbb{S} + \mathbb{S} \cdot (\boldsymbol{\partial v}) - \frac{2}{\tau_{\mathrm{p}}} (\mathbb{S} - \mathbb{1}) \quad , \tag{5.2}$$

where the matrix of velocity gradients is defined as $(\boldsymbol{\partial v})_{ij} \equiv \partial_i v_j$ and $\mathbb{1}$ denotes the unity tensor. The terms $(\boldsymbol{\partial v})^T \cdot \mathbb{S} + \mathbb{S} \cdot (\boldsymbol{\partial v})$ represent the stretching due to the velocity field and $2(\mathbb{S} - \mathbb{1})/\tau_{\mathrm{p}}$ the relaxation to the equilibrium configuration, i.e., $\mathbb{1}$.
Eq. (5.2) must be supplemented by the evolution equation for the velocity field, which is derived from momentum conservation law (see Sec. A.1 in appendix):

$$\frac{Dv_i}{Dt} = f_i + \frac{1}{\rho} \partial_j \mathbb{T}_{ij} \tag{5.3}$$

where $\rho$ is the constant fluid density, $\boldsymbol{f}$ the sum of body forces driving the flow and $\mathbb{T}$ the stress tensor of the fluid. In the case of a viscoelastic solution, the stress tensor is given by the sum of the Newtonian stress tensor $\mathbb{T}_{\mathrm{N}}$ (see Sec. A.1), and the elastic stress tensor $\mathbb{T}_{\mathrm{p}}$, which takes into account elastic forces due to the presence of polymers and is given by $(\mathbb{T}_{\mathrm{p}})_{ij} = (2\eta_{\mathrm{p}} \nu_o \rho / \tau_{\mathrm{p}}) \mathbb{S}_{ij}$, where $\nu_o$ is the solvent viscosity and $\eta_{\mathrm{p}}$ (proportional to polymer concentration) represents the zero-shear contribution of polymers to the total solution viscosity. The Navier–Stokes equation for the incompressible velocity field $\boldsymbol{v}(\boldsymbol{x}, t)$ thus becomes:

$$\partial_t \boldsymbol{v} + \boldsymbol{v} \cdot \boldsymbol{\partial v} = \boldsymbol{\partial} p + \nu_o \partial^2 \boldsymbol{v} + \frac{2\eta_{\mathrm{p}} \nu_o}{\tau_{\mathrm{p}}} \boldsymbol{\partial} \cdot (\mathbb{S} - \mathbb{1}) + \boldsymbol{f} \tag{5.4}$$

where $p$ is the pressure. In the limit $\tau_{\mathrm{p}} \to 0$, the elastic force originated from thermal motion keeps the molecules near their equilibrium configuration, and the polymer solution is expected to behave like a Newtonian fluid. Nevertheless, the presence of polymers affects fluid properties also in the Newtonian limit, because the fluid is partially trapped in the coiled polymers, producing a change of the total viscosity of the solution as $\nu = \nu_o (1 + \eta_{\mathrm{p}})$.

## 5.2 Rayleigh–Taylor instability and polymers

Let us consider the Rayleigh–Taylor instability in the presence of the surface-tension effect. As discussed in Chap 4, the time evolution is well described by using the phase-field approach. Now, let us suppose to add a small amount of polymers in a way to obtain a dilute solution (few parts per million in mass). Let us consider the most general case of different viscosities

for two fluids. The following coupled differential equations rule the time evolution of the binary fluids with polymers:

$$\begin{aligned}
\rho_o\left(\partial_t \boldsymbol{v} + \boldsymbol{v}\cdot\boldsymbol{\partial}\boldsymbol{v}\right) &= -\boldsymbol{\partial}p + \boldsymbol{\partial}\cdot(2\mu_o(\phi)\boldsymbol{e}) - \phi\boldsymbol{\partial}\mathcal{M} + \rho_o\mathcal{A}\boldsymbol{g}\phi + \frac{2\eta_{\rm p}\mu_o}{\tau_{\rm p}}\boldsymbol{\partial}\cdot(\mathbb{S}-\mathbb{1}) \quad (5.5)\\
\partial_t\phi + \boldsymbol{v}\cdot\boldsymbol{\partial}\phi &= \gamma\partial^2\mathcal{M} \quad (5.6)\\
\partial_t\mathbb{S} + \boldsymbol{v}\cdot\boldsymbol{\partial}\mathbb{S} &= (\boldsymbol{\partial}\boldsymbol{v})^T\cdot\mathbb{S} + \mathbb{S}\cdot\boldsymbol{\partial}\boldsymbol{v} - \frac{2}{\tau_{\rm p}}(\mathbb{S}-\mathbb{1}) \quad (5.7)
\end{aligned}$$

where $\rho_o = (\rho_1+\rho_2)/2$, $\mu_o(\phi)$ is the dynamical viscosity dependent of fluids, $e_{ij} \equiv (\partial_i v_j + \partial_j v_i)/2$ is the strain tensor, and $\boldsymbol{g}$ is selected, as usual, along the $z$-axis. Regarding the viscosity, the two fluids are assumed to have dynamical viscosities $\mu_1$ and $\mu_2$ in a way that the global dynamical viscosity, $\mu_o(\phi)$, has the form [92]:

$$\frac{1}{\mu_o} = \frac{1+\phi}{2\mu_1} + \frac{1-\phi}{2\mu_2} \quad . \quad (5.8)$$

As far as polymers are concerned, we assume $\eta_{\rm p} \ll 1$ to be fluid dependent in a way to have $\eta_{\rm p}\mu_o$ constant.
It is easy to verify that the total energy

$$E = \mathcal{F} + \int dx\,dy\,dz\,\left(\frac{\rho_o}{2}|\boldsymbol{v}|^2 + \rho_o\mathcal{A}gz\phi + \frac{\eta_{\rm p}\mu_o}{\tau_{\rm p}}Tr(\mathbb{S}-\mathbb{1})\right) \quad (5.9)$$

obeys the balance

$$\frac{dE}{dt} = -\mu_o|\boldsymbol{\partial}\boldsymbol{v}|^2 - \gamma|\boldsymbol{\partial}\mathcal{M}|^2 - \frac{2\eta_{\rm p}\mu_o}{\tau_{\rm p}^2}Tr(\mathbb{S}-\mathbb{1}) \quad . \quad (5.10)$$

The equilibrium solution is given by

$$\begin{aligned}
\boldsymbol{v} &= \boldsymbol{0}\\
\phi(z) &= \tanh\left(\frac{z}{\sqrt{2}\varepsilon}\right) \quad (5.11)\\
\mathbb{S} &= \mathbb{1}
\end{aligned}$$

corresponding to a planar interface of width $\varepsilon$ with polymers having their equilibrium length.

### 5.2.1 Linear stage: speed-up induced by polymers

The aim of this section is to investigate the polymer effect on the first stage of RT instability. The following strategy is similar to that exploited in Sec 4.2.4, to derive the dispersion relation for the phase field.
For a given disturbance on the interface, the question is in which way the polymers affect the initial time evolution of the instability.
Without loss of generality, we focus on the case of disturbance imposed to the interface as varying along the $x$ axis, and invariant along the other horizontal direction, the $y$ axis. For sake of notation, we denote derivatives and velocity as $\boldsymbol{\partial} \equiv (\partial_1,\partial_2,\partial_3) = (\partial_x,\partial_y,\partial_z)$ and

$\boldsymbol{v} \equiv (v_1, 0, v_3) = (u, 0, w)$, respectively. Moreover we define $(\boldsymbol{\partial v})_{ij} \equiv \partial_i v_j$ .
Denoting by $h(x,t)$ a small disturbance, let us consider an almost planar interface:

$$\phi = f\left(\frac{z - h(t,x)}{\varepsilon}\right) \quad , \tag{5.12}$$

where $h$ can be larger than $\varepsilon$, yet it has to be smaller than the scale of variation of $h$ (small amplitudes). We also have the constraint $\varepsilon \ll R_0$.
From the local equilibrium of the interface, expressed by (4.19), and in the limit of small interface velocity, the following equation for the vertical component of velocity $w$ is easily obtained:

$$\rho_o \partial_t w = -\partial_z p - \phi \partial_z \mathcal{M} - \mathcal{A} g \rho_o \phi + \frac{2\eta_{\rm p}\nu\rho_o}{\tau_{\rm p}} \partial_i \zeta_{i3} + \mu_o \left(\partial_x^2 w + \partial_z^2 w\right) + 2(\partial_z w)\partial_z \mu_o \tag{5.13}$$

where $\boldsymbol{\zeta}$ is the perturbation at the equilibrium of the conformation tensor.
Let us introduce:

$$q_z \equiv \lim_{L\uparrow\infty} \int_{-L}^{+L} w \, dz \quad . \tag{5.14}$$

Integrating along the vertical direction, and performing an integration by parts one gets the following equation for $q_z$:

$$\begin{aligned}\rho_o \partial_t q_z = \lim_{L\uparrow\infty} \Bigg\{ \frac{\Lambda}{\varepsilon} \int_{-L}^{+L} \left[ f f'' \frac{\partial^2 h}{\partial x^2} - \frac{1}{\varepsilon} f f''' \Big(\frac{\partial h}{\partial x}\Big)^2 \right] d(z/\varepsilon) - \mathcal{A} g \rho_o \int_{-L}^{+L} f dz + \\ + \frac{2\eta_{\rm p}\mu_o}{\tau_{\rm p}} \int_{-L}^{+L} \partial_x \zeta_{13} \, dz + \int_{-L}^{+L} \mu_o \frac{\partial^2 w}{\partial x^2} \, dz - \int_{-L}^{+L} \mu_o \frac{\partial^2 w}{\partial z^2} \, dz \Bigg\}\end{aligned} \tag{5.15}$$

that is

$$\rho_o \partial_t q_z = \sigma \frac{\partial^2 h}{\partial x^2} + 2\mathcal{A} g \rho_o h + \frac{2\eta_{\rm p}\mu_o}{\tau_{\rm p}} \Sigma + \int_{-\infty}^{+\infty} \mu_o \frac{\partial^2 w}{\partial x^2} \, dz - \int_{-\infty}^{+\infty} \mu_o \frac{\partial^2 w}{\partial z^2} \, dz \tag{5.16}$$

where we have defined $\Sigma \equiv \lim_{L\uparrow\infty} \int_{-L}^{+L} \partial_x \zeta_{13} \, dz$ and we have performed the integration by parts exploiting the relations $\int (f')^2 dz = 2\sqrt{2}/3$, $\int f f''' dz = 0$, $\int f dz = -2h$.
Notice how, unlike what happens in the inviscid case ($\mu_1 = \mu_2 = 0$), the above equation does not involve solely the field $q_z$ but also second order derivatives of $w$. Eq. (5.16) is thus not closed. To circumvent the problem let us resort to a potential-flow description proposed in [100]. The idea is to evaluate

$$Q \equiv \lim_{L\uparrow\infty} \left\{ \int_{-L}^{+L} \mu_o \frac{\partial^2 w}{\partial x^2} \, dz - \int_{-L}^{+L} \mu_o \frac{\partial^2 w}{\partial z^2} \, dz \right\} \tag{5.17}$$

for a potential flow $w$ (thus defining $Q^{pot}$) and then to assume $Q = Q^{pot}$ and plug the resulting expression into Eq. (5.16).
The approximation is justified when viscosity is sufficiently small and its dynamical effects confined in a narrow band around the interface. Consistency conditions at the end of the calculation will fix quantitatively the range of validity of the above approximation.

By assuming a potential flow, we can easily relate the velocity at interface $w^{(int)}$ with the integral $q_z$ (see Eq. (4.27) and following ones). The final result in Fourier space is:

$$\hat{w}^{(int)}(x,t) = \partial_t \hat{h} = \frac{k\hat{q}_z}{2} \tag{5.18}$$

where "$\hat{\cdot}$" denotes the Fourier transform. Moreover we obtain:

$$Q^{pot} = 2 \lim_{L\uparrow\infty} \int_{-L}^{+L} \mu_o \frac{\partial^2 w}{\partial x^2}\, dz = (\mu_1+\mu_2)\frac{\partial^2 q_z}{\partial x^2} \quad . \tag{5.19}$$

As we have anticipated, we now assume $Q = Q^{pot}$ and plug it into (5.16). The final result reads:

$$\rho_o \partial_t q_z = \sigma \frac{\partial^2 h}{\partial x^2} + 2\mathcal{A} g \rho_o h + \frac{2\eta_{\rm p}\mu_o}{\tau_{\rm p}}\Sigma + (\mu_1+\mu_2)\frac{\partial^2 q_z}{\partial x^2} \quad . \tag{5.20}$$

The last step to perform is to find out the equation for $\Sigma$. To do that, we start from the equation for $\zeta_{ij}$. It easily follows from the original equation for $\mathbb{S}$:

$$\partial_t \zeta_{ij} = \partial_i v_j + \partial_i v_j - \frac{2}{\tau_{\rm p}}\zeta_{ij} \quad . \tag{5.21}$$

From this equation we get:

$$\partial_t \partial_x \zeta_{13} = \partial_x(\partial_z u + \partial_x w) - \frac{2}{\tau_{\rm p}}\partial_x \zeta_{13} \tag{5.22}$$

or, exploiting incompressibility ($\partial_i v_i = 0$):

$$\partial_t \partial_x \zeta_{13} = -\partial_z^2 w + \partial_x^2 w - \frac{2}{\tau_{\rm p}}\partial_x \zeta_{13} \quad . \tag{5.23}$$

Finally, exploiting again the potential flow description to recast $-\partial_z^2 w + \partial_x^2 w$ and integrating along $z$ we arrive to the equation for $\Sigma$:

$$\partial_t \Sigma = -\frac{2}{\tau_{\rm p}}\Sigma + 2\,\partial_x^2 q_z \quad . \tag{5.24}$$

To summarize, our problem in Fourier space is reduced to solve the following set of differential equations:

$$\partial_t \hat{q}_z = -\frac{\sigma}{\rho_o}k^2\hat{h} + 2\mathcal{A}g\hat{h} + \frac{2\eta_{\rm p}\nu_o}{\tau_{\rm p}}\hat{\Sigma} - 2\nu_o k^2 \hat{q}_z \tag{5.25}$$

$$\partial_t \hat{h} = \frac{k\hat{q}_z}{2} \tag{5.26}$$

$$\partial_t \hat{\Sigma} = -\frac{2}{\tau_{\rm p}}\hat{\Sigma} - 2\,k^2\hat{q}_z \quad , \tag{5.27}$$

where the kinematic viscosity $\nu_o \equiv (\mu_1+\mu_2)/(\rho_1+\rho_2)$ has been introduced. For the sake of simplicity, let us assume $\mu_1 = \mu_2 = \mu_o$ (and thus $\nu_o = \mu_o/\rho_o$). Regarding the time dependence of unknown fields, we impose an exponential form, $e^{n_{\rm p}t}$. The condition to have

nontrivial solution of the resulting algebraic linear system yields to the cubic equation for the growth rate $n_{\rm p}$:

$$2\,\rho_o\,{n_{\rm p}}^3\tau_{\rm p}+\left(4\,\rho_o+4\,\nu_o\,k^2\rho_o\,\tau_{\rm p}\right)n_{\rm p}^2+ \\ +\left(\sigma\,k^3\tau_{\rm p}+8\,\rho_o\,\nu_o\,k^2+8\,\eta_{\rm p}\,\rho_o\,\nu_o\,k^2+\right. \\ \left.-2\,k\mathcal{A}\rho_o\,g\tau_{\rm p}\right)n_{\rm p}-4\,k\mathcal{A}\rho_o\,g+2\,\sigma\,k^3=0 \quad (5.28)$$

that can be recast in the form:

$$(n_{\rm p}\,\tau_{\rm p})^3+2\,(n_{\rm p}\,\tau_{\rm p})^2(1+\nu_o\,k^2\,\tau_{\rm p})+ \\ -n_{\rm p}\,\tau_{\rm p}\left[n^2\,\tau_{\rm p}^2-4\,\nu_o\,(\eta_{\rm p}+1)\,k^2\,\tau_{\rm p}\right]-2\,\left(n^2\,\tau_{\rm p}\right)^2=0 \quad , \quad (5.29)$$

where we have defined as

$$n^2(k)\equiv\mathcal{A}gk-\frac{\sigma}{2\rho_o}k^3 \quad (5.30)$$

the square growth rate of the perturbation in the absence of polymers and for zero viscosity. The following remarks make Eq. (5.29) more tractable. Let us define the Weissenberg number referring to the inviscid ($\nu_o=0$) case and in the absence of polymers, as $\mathcal{W}i\equiv n\tau_{\rm p}$. Moreover we let us define the Reynolds number as $\mathcal{R}e_{\nu_o}\equiv n/(\nu_o k^2)$. In order to be consistent with the potential description we necessarily have to impose $\mathcal{R}e_{\nu_o}\gg 1$ which corresponds to consider that the viscous typical time is larger than the typical time of perturbation. Moreover, assuming that polymers cause a small correction to the perturbation evolution we have $\mathcal{W}i\ll 1$ and, as a consequence, also $n_{\rm p}\tau_{\rm p}\ll 1$. By virtue of these latter assumptions, we can safely neglect the term $(n_{\rm p}\,\tau_{\rm p})^3$ in (5.29), the solution of which is now easily obtained as:

$$n_{\rm p}\,\tau_{\rm p}=\frac{\frac{n^2\,\tau_{\rm p}^2}{4}-(\eta_{\rm p}+1)\nu_o\,k^2\,\tau_{\rm p}+\sqrt{\frac{n^4\,\tau_{\rm p}^4}{16}+\frac{n^2\,\tau_{\rm p}^3\,\nu_o\,(1-\eta_{\rm p})\,k^2}{2}+n^2\,\tau_{\rm p}^2+[\nu_o\,(\eta_{\rm p}+1)\,k^2]^2\,\tau_{\rm p}^2}}{1+\nu_o\,k^2\tau_{\rm p}} \quad . \quad (5.31)$$

In terms of $\mathcal{W}i$, $\mathcal{R}e_{\nu_o}$ and the elasticity $\mathcal{E}\equiv\mathcal{W}i/\mathcal{R}e_{\nu_o}$, the above solution has the following structure (omitting prefactors of order unity)

$$n_{\rm p}\tau_{\rm p}\sim\mathcal{W}i^4+\mathcal{E}+\sqrt{\mathcal{W}i^4+\mathcal{W}i^2\mathcal{E}+\mathcal{W}i^2+\mathcal{E}^2} \quad . \quad (5.32)$$

In the previous relation, the terms proportional to $\mathcal{W}i^4$ can be neglected and our final expression becomes:

$$n_{\rm p}=-(\eta_{\rm p}+1)\nu_o\,k^2+\sqrt{n^2\left(1+\frac{\tau_{\rm p}\,\nu_o\,(1-\eta_{\rm p})\,k^2}{2}\right)+[\nu_o\,(\eta_{\rm p}+1)\,k^2]^2} \quad . \quad (5.33)$$

We infer that polymers increase the growth rate of perturbation via renormalisation of both the inviscid growth rate and (as expected) the solvent viscosity.
It is worth noting that in the limit of $\tau_{\rm p}\to 0$ we recover the following limit

$$n_{\rm p}=-(\eta_{\rm p}+1)\nu_o\,k^2+\sqrt{n^2+[\nu_o\,(\eta_{\rm p}+1)\,k^2]^2} \qquad \text{for} \qquad \tau_{\rm p}\to 0 \quad , \quad (5.34)$$

which corresponds to the upper bound for the linear growth rate in the case of non-negligible viscosity effect, Eq. (1.8). The sole difference is the renormalisation of viscosity for effect of polymers. Finding the upper bound is not surprising, indeed in the preceding derivation we have analysed the limit of small viscosity in order to be able to consider the hypothesis of potential flow approximately true.

#### 5.2.1.1 Numerical investigation: preliminary results

The aim of this section is to describe our preliminary numerical results concerning the polymer effects on the linear regime of instability, referring to the growth-rate expression (5.33). We focus on the immiscible two-dimensional case. This choice makes allow us to single out the effects of polymers. Indeed we compare the results with previous ones showed in Sec. 4.3.2.
By means of Direct Numerical Simulations (see page 13) we integrate the evolution equations introduced in the preceding section, Eqs. (5.5)-(5.6)-(5.7). The integration is exploited on a doubly periodic domain of horizontal-vertical aspect-ratio $L_x : L_z = 1 : 1$ and resolution $1024 \times 1024$.
All simulations start from an initial condition corresponding to an equilibrium configuration: zero velocity, conformation tensor equal to the unity tensor and hyperbolic tangent profile for the phase field, expressed as $\tanh\left((z - h(x, t = 0))/\sqrt{2}\varepsilon\right)$ with $h(x, t = 0) = h_0 \sin(x)$. The initial disturbance amplitude is selected in a way to satisfy both limits of small disturbance, $h_0/\lambda = 0.015$, and infinitesimal capillary mixing width, $h_0/\varepsilon = 10$. The Reynolds number $\mathcal{Re}_{\nu_o}$, defined in previous section, is fixed to the value 1.8. Except for the polymer presence, the configuration is the same as the one of Sec. 4.3.2.
In order to capture the effects of polymers we performed different runs at different values of relaxation time $\tau_{\mathrm{p}}$. Our results are summarised in Fig. 5.5 where the growth-rate $n_{\mathrm{p}}$ is shown as a function of the relaxation time in dimensionless form. The growth-rate values are obtained via best fit of $h(x, t)$.
In Fig 5.5 the growth-rate $n_{\mathrm{p}}$ are compared with the growth-rate $n_\nu$ corresponding to the Newtonian case with viscosity equal to 0.39 (model units). This value corresponds to the renormalised viscosity $\nu = \nu_o(\eta_{\mathrm{p}} + 1)$ (introduced on pag. 57).

Some remarks are worth emphasising. Firstly, for finite $\mathcal{Wi}$ the role of polymers in the linear phase of the growth process confirms the analytical results obtained in previous section for small $\mathcal{Wi}$: polymers speed up the mixing process with respect to the Newtonian case. Secondly, their effect tends to saturate for sufficiently large $\mathcal{Wi}$. The physical explanation of that can be found in the fact that polymers, at least at level of linear analysis, react weakly on the flow. This amounts to saying that $\boldsymbol{\partial} \cdot (\mathbb{S} - \mathbb{1})$ in the polymer stress term in Eq. (5.5), remains finite for increasing $\tau_{\mathrm{p}}$ thus giving a vanishing stress contribution in the asymptotic limit $\mathcal{Wi} \to \infty$.
Whether or not this tendency to increase the mixing properties in the weakly nonlinear phase and in the fully developed turbulence stage will be subject of intensive future research.

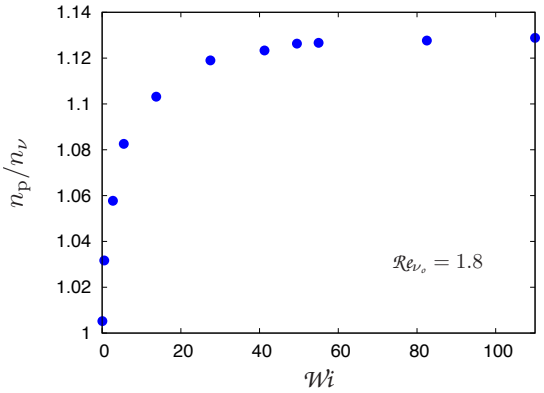


**Figure 5.5:** Growth-rate $n_{\rm p}$ as a function of the Weissenberg number $\mathcal{W}i \equiv \tau_{\rm p} n$ with $n$ the growth rate referring to the case without both polymers and viscosity (see, Eq. 1.4). The growth-rate $n_{\rm p}$ is divided by $n_\nu$ which is the growth rate in the Newtonian case with viscosity equal to 0.39 (model units).

## 5.3 Conclusions and Perspectives

The key question of the analysis presented in this chapter is on whether the addition of a small amount of polymers into the RT system modify its instability properties. Our preliminary results, regarding the first regime, highlight how polymers change the growth rate of perturbation: the linear instability becomes faster (with respect to the case without polymers and viscosity equal to the renormalised one). The next step is to understand the effects on the turbulent mixing layer and specifically, on the global quantities (i.e., the behaviour in time of Reynolds, Nusselt and Rayleigh numbers). From simple mean-field arguments we expect that polymers start to affect the dynamics of the turbulent cascade at the scale, the so-called Lumley scale, at which the eddy turnover time is of the same order of the relaxation time (see for an investigation of small-scale statistics of viscoelastic turbulence, for instance, [14]). At this scale there is an interplay between the hydrodynamics and elastic degrees of freedom. The scenario appears to be similar to that described in Sec. 1.4.3 in the case of the immiscible configuration: the energy flux at the Lumley scale feeds, instead of the capillary waves on drop surface, the polymer deformation.
Moreover the viscoelastic system, unlike the Newtonian case, appears to be strongly sensitive to the spatial dimensions. By means of classical mean field arguments it is possible to see that the Lumley scale goes to zero in two dimensions (2D) while this is not in the three-dimensional (3D) case. We thus expect transient effects in the 2D case and, conversely, robust effects in 3D.
All these issues will be the subject of deep investigations during my post-doc activity.

# Appendix A

# Introduction to turbulence

"NEWTON: *I simply can't stand disorder. Really it was my love of order that made me become a physicist to interpret the apparent disorder of Nature in the light of a more sublime order...*"
English translation of Die Physiker by Friedrich Dürrenmatt (1962)

Turbulence is a state of a physical system with many degrees of freedom strongly deviating from equilibrium. The first obstacle to its understanding stems from the large number of degrees of freedom actively involved in the problem. The scale of injection, where the turbulence is excited, usually differs strongly from the scale of damping, where dissipation takes place. Nonlinear interactions strongly couple the degrees of freedom by transferring excitations from the injection to the damping scale throughout the so-called inertial range of scales. The ensuing complicated and irregular dynamics calls for a statistical description. The main physical problem is to understand to what extent the statistics in the inertial range is universal, that is, independent of the conditions of excitation and dissipation. From the standpoint of theoretical physics, turbulence is a non-equilibrium field-theoretical problem with many strongly interacting degrees of freedom. The second deeply rooted obstacle to its understanding is that far from equilibrium we do not possess any general guiding rule. Indeed, to describe the single-time statistics of equilibrium systems, the only thing we need is the knowledge of dynamic integrals of motion. Dynamically conserved quantities play an important role in turbulence description, as they flow throughout the inertial range in a cascade-like process. However, the conserved quantity alone does not allow to describe the whole statistics but only a single correlation function which corresponds to its flow. The major problem is to obtain the rest of the statistics.
The complexity of turbulence has attracted for centuries the interest of scientists, philosophers and poets. Images and metaphors of turbulence of impetuous rivers and stormy seas are ubiquitous in literature, and the drawings and scripts of Leonardo da Vinci can be considered the earliest scientific studies on turbulence, which grasped some realistic details of the problem.
On the other hand, the interest for turbulence is clearly understandable because of its practical relevance in applications ranging from naval and aeronautical engineering to climate studies and weather forecast.
In the last century the works of L. Euler, L. M. H. Navier, G. G. Stokes, O. Reynolds have given the basis of a research field which is still open nowadays. Even if the equations which rule the turbulent behaviour are well known, a complete understanding of the matter is still

lacking.

In this chapter a short introduction to the basic concepts and phenomenology of the theory of statistically-stationary turbulence is presented. The two-dimensional turbulence is also presented, Sec. A.3, stressing the differences and similarities with the three-dimensional case. Moreover the issue of scalar turbulence is introduced, Sec A.4.
The aim is not to provide a review of the matter which can be found in [8, 12, 60, 101], but just to introduce, for the sake of self-consistency, the terms and concepts that are used in the thesis.

## A.1 Navier–Stokes equation

The dynamics of an incompressible Newtonian fluid is determined by the celebrated Navier–Stokes equation (1823), supplemented by the incompressibility condition:

$$\partial_t \boldsymbol{v} + \boldsymbol{v} \cdot \boldsymbol{\partial} \boldsymbol{v} = -\frac{\boldsymbol{\partial} p}{\rho} + \nu \partial^2 \boldsymbol{v} + \boldsymbol{f} \tag{A.1}$$

$$\boldsymbol{\partial} \cdot \boldsymbol{v} = 0 \tag{A.2}$$

where $p$ is the pressure, $\rho$ is the density of the fluid, $\nu = \mu/\rho$ is its kinematic viscosity (and $\mu$ its dynamical viscosity), and $\boldsymbol{f}$ represents the sum of the external forces per unit mass which sustain the motion.
Let us briefly describe the different terms in Navier–Stokes equation:

- $\boldsymbol{v} \cdot \boldsymbol{\partial} \boldsymbol{v}$ the inertial, or nonlinear term which characterises Navier–Stokes equation, and is responsible for the transfer of kinetic energy in the turbulent cascade.
- $-\boldsymbol{\partial} p/\rho$ the pressure gradients which guarantee the incompressibility of the flow. In absence of external forces they are determined by the Poisson equation

  $$\partial^2 p = -\rho \partial_i \partial_j v_i v_j \tag{A.3}$$

  which is obtained taking the divergence of Eq. (A.1).
- $\nu \partial^2 \boldsymbol{v}$ the dissipative viscous term. It is originated by the Reynolds stresses of the Newtonian fluid, and it is proportional to the viscosity. It is the dominant term in the laminar regime.

The origin of Eqs. (A.1)-(A.2) is just the conservation of mass and momentum per unit volume:

$$\frac{\partial \rho}{\partial t} + \boldsymbol{\partial} \cdot (\rho \boldsymbol{v}) = 0 \tag{A.4}$$

$$\frac{D u_i}{D t} = f_i + \frac{1}{\rho} \frac{\partial \mathbb{T}_{ij}}{\partial x_j} \tag{A.5}$$

where $\mathbb{T}$ is the stress tensor of the fluid, which for a Newtonian fluid is linear in the deformation tensor $e_{ij} = (\partial_j v_i + \partial_i v_j)/2$, and is given by [86]:

$$\mathbb{T}^N_{ij} = -p \delta_{ij} + \mu \left[ \frac{1}{2} (\partial_j v_i + \partial_i v_j) - \frac{2}{3} \partial_k v_k \delta_{ij} \right] . \tag{A.6}$$

The incompressibility assumption is consistent when velocities smaller than speed of sound $c_s$ in the fluid are considered. Since eventual density fluctuations are swept away exactly as sound waves, for small value of the Mach number, which measures the ratio between the typical velocities and the speed of sound in the considered fluid, the density can be assumed to be constant in time and space $\rho(\boldsymbol{x}, t) = \rho$ and the mass conservation (A.4) leads to the divergence-less condition on the velocity field $\boldsymbol{\partial} \cdot \boldsymbol{v} = 0$. It is common to assume the constant density to be equal to unity, or equivalently to consider dynamical quantities per unit mass of fluid. As an example we will often refer to the square modulus of velocity as kinetic energy.
Because of the presence of a nonlinear term in Navier–Stokes equation, the space of its solutions does not have an affine structure, and consequently a generic solution cannot be obtained as linear superposition of basic solutions. Moreover, a typical feature of turbulence is the presence of chaos, i.e. the Navier–Stokes equation displays a strong sensitivity to initial conditions, which drastically reduces the interest for their exact solutions. For this reason the theory of turbulence has a statistical approach, trying to predict the statistical properties of the flow instead of searching a peculiar analytic solution.

### A.1.1 Reynolds number

A measure of the nonlinearity of Navier–Stokes equation is given by the Reynolds number

$$\mathcal{R}e = \frac{UL}{\nu} \tag{A.7}$$

where $L$ and $U$ are respectively the typical length scale and velocity of the fluid, e.g., in a pipe flow $L$ is the diameter of the pipe and $U$ the mean velocity. It was introduced by Osborne Reynolds, who showed that a transition between laminar and turbulent flow occurs when the $\mathcal{R}e$ number reaches a critical value [122] (Fig. A.1).
Different geometries of the flow may change the critical $\mathcal{R}e$ number, but the transition is universally controlled by this adimensional parameter. The Reynolds number plays a fundamental role in turbulence, since it gives a dimensional estimate of the relative weight between the inertial term $\boldsymbol{v} \cdot \boldsymbol{\partial v}$ and the viscous term $\nu \partial^2 \boldsymbol{v}$:

$$\frac{[\boldsymbol{v} \cdot \boldsymbol{\partial v}]}{[\nu \partial^2 \boldsymbol{v}]} \sim \frac{UL}{\nu} \quad . \tag{A.8}$$

Because of its definition, the limit $\mathcal{R}e \to \infty$, in which fully developed turbulence is achieved, can be rephrased as the zero-viscosity limit $\nu \to 0$.

### A.1.2 Energy balance

The energy balance in the absence of external forcing for Navier–Stokes equation follows from Eqs. (A.1)-(A.2). The total kinetic energy of the fluid is

$$E = \int d^3 r \frac{1}{2} \rho |\boldsymbol{v}|^2 \tag{A.9}$$

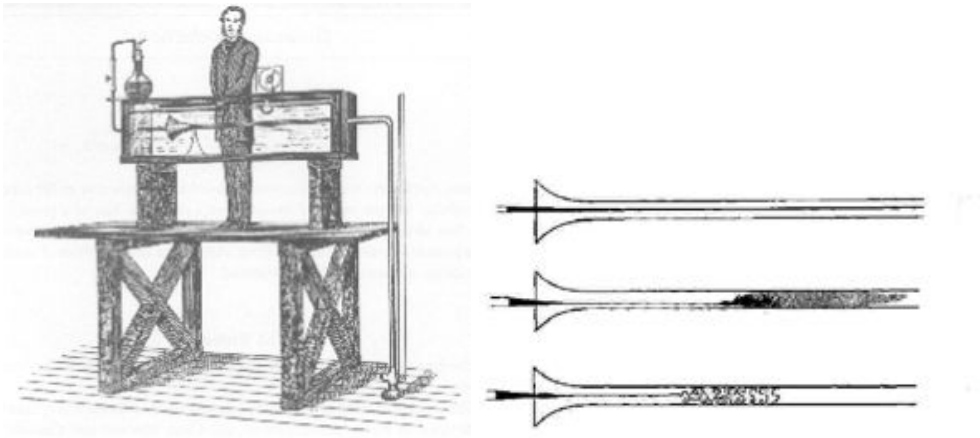

**(a)** **(b)**

**Figure A.1: (a)** Experimental setup of the experiment performed by Reynolds [122]. Reynolds focused on the transition between laminar and turbulent in the pressure-driven flow through a straight pipe of circular cross section. In his experiment, water flows from a tank through a horizontally oriented glass pipe. In addition a streak of dyed water enters the tube together with the clear water and allows to visualise the flow. **(b)** Original sketches by Reynolds [122]. From top to bottom, Reynolds number increases. Reynolds in his experiments showed that the spatio-temporal behaviour of the flow depends on a single dimensionless parameter, that is, the Reynolds number.

and its temporal variation is

$$\begin{aligned} \frac{dE}{dt} &= \int d^3r\, \rho\, \boldsymbol{v} \cdot \frac{\partial \boldsymbol{v}}{\partial t} \\ &= \int d^3r\, \rho\, [-v_i v_j \partial_j v_i - v_i \partial_i p + \nu v_i \partial_j \partial_j v_i] \quad . \end{aligned} \tag{A.10}$$

Assuming periodic boundary conditions on a cubic volume of size $L$

$$\boldsymbol{v}(x + nL, y + mL, z + qL) = \boldsymbol{v}(x, y, z) \quad \forall x, y, z \in \mathbb{R}\, \forall n, m, q \in \mathbb{Z} \tag{A.11}$$

or null boundary conditions on a volume $V$

$$\boldsymbol{v}\,|_{\,\partial V} = 0 \tag{A.12}$$

the first two terms in the integral vanish, and using the identity

$$\begin{aligned} (\boldsymbol{\partial} \times \boldsymbol{v}) \cdot (\boldsymbol{\partial} \times \boldsymbol{v}) &= (\epsilon_{ijk} \partial_j v_k)(\epsilon_{ilm} \partial_l v_m) \\ &= \partial_j (v_k \partial_j v_k) - \partial_j \partial_k (v_j v_k) - v_k \partial_j \partial_j v_k \end{aligned} \tag{A.13}$$

one gets

$$\frac{dE}{dt} = \nu \int d^3r\, \rho\, \boldsymbol{v} \partial^2 \boldsymbol{v} = -\nu \int d^3r\, \rho (\boldsymbol{\partial} \times \boldsymbol{v})^2 = -\nu \int d^3r\, \rho |\boldsymbol{\omega}|^2 \tag{A.14}$$

where we have have introduced the *vorticity* of the fluid $\boldsymbol{\omega} = \boldsymbol{\partial} \times \boldsymbol{v}$. Defining the total *e*nstrophy as

$$Z = \int d^3r\, \frac{1}{2} \rho |\boldsymbol{\partial} \times \boldsymbol{v}|^2 \tag{A.15}$$

the energy balance reads:

$$\frac{dE}{dt} = -2\nu Z \tag{A.16}$$

which shows that in the absence of external forcing and for $\nu = 0$ the kinetic energy is conserved by the dynamics, i.e. it is an inviscid invariant. On the contrary in the limit $\nu \to 0$ the energy dissipation rate does not vanish, but reaches a constant value [136]:

$$\lim_{\nu \to 0} 2\nu Z \equiv \epsilon \quad . \tag{A.17}$$

This phenomenon is known as *dissipative anomaly*, and implies that in the limit $\nu \to 0$ the total enstrophy must grow as $Z \sim \nu^{-1}$ to compensate the decreasing viscosity. The unbounded growth of enstrophy in three dimensions is the physical origin of the dissipative anomaly, and it is possible because of the *vortex stretching*, which produces diverging velocity gradient in the limit $\mathcal{R}e \to \infty$.

### A.1.3 Energy transfer

As shown by the global energy balance Eq. (A.16) the nonlinear term in Navier–Stokes equation does not change the total kinetic energy. Nevertheless it plays a fundamental role in turbulence, because it is responsible for the energy transfer between different modes which is the origin of the turbulent cascade. To describe how it is involved in the energy transfer it is worthwhile to consider the energy balance in Fourier space. For the sake of simplicity we will consider the infinite-volume limit, in which the fluid is supposed to fill the entire space, and the Fourier transform reads

$$\hat{v}_\alpha(\boldsymbol{k}) = \frac{1}{(2\pi)^3} \int d^3x e^{-i\boldsymbol{k}\cdot\boldsymbol{x}} v_\alpha(\boldsymbol{x}) \tag{A.18}$$

and its inverse is

$$v_\alpha(\boldsymbol{x}) = \int d^3k \, e^{i\boldsymbol{k}\cdot\boldsymbol{x}} \hat{v}_\alpha(\boldsymbol{k}) \quad . \tag{A.19}$$

The reality condition on the velocity fields $v^*_\alpha(\boldsymbol{x}) = v_\alpha(\boldsymbol{x})$ in Fourier space reads $\hat{v}^*_\alpha(\boldsymbol{k}) = \hat{v}_\alpha(-\boldsymbol{k})$, and the derivatives become multiplicative operators ($\boldsymbol{\partial} \to i\boldsymbol{k}$), thus the incompressibility assumption is written as $\boldsymbol{k} \cdot \hat{\boldsymbol{v}} = 0$. In Fourier space Navier–Stokes equation has the form:

$$\begin{aligned} \frac{\partial \hat{v}_\alpha(\boldsymbol{k})}{\partial t} \quad = \quad & -i \int d^3p \, (k_\beta - p_\beta) \hat{v}_\beta(\boldsymbol{p}) \hat{v}_\alpha(\boldsymbol{k} - \boldsymbol{p}) + \\ & + i \frac{k_\alpha}{k^2} \int d^3p \, \hat{p}_\gamma (k_\beta - p_\beta) \hat{v}_\beta(\boldsymbol{p}) \hat{v}_\gamma(\boldsymbol{k} - \boldsymbol{p}) + \\ & - \nu k^2 \hat{v}_\alpha(\boldsymbol{k}) \end{aligned} \tag{A.20}$$

where it is still possible to distinguish the inertial term, the pressure term and dissipative term, while the forcing has been omitted. The constant density has been fixed to $\rho = 1$. Using the incompressibility and the symmetry of the integrals for $(\boldsymbol{p}, \boldsymbol{k} - \boldsymbol{p}) \to (\boldsymbol{p} - \boldsymbol{k}, \boldsymbol{p})$ it is possible to rewrite Eq. (A.20) as

$$\left( \frac{\partial}{\partial t} + \nu k^2 \right) \hat{v}_\alpha(\boldsymbol{k}) = -i \left( k_\beta \delta_{\alpha\gamma} - \frac{k_\alpha k_\beta k_\gamma}{k^2} \right) \int d^3p \, \hat{v}_\beta(\boldsymbol{p}) \hat{v}_\gamma(\boldsymbol{k} - \boldsymbol{p}) \quad . \tag{A.21}$$

Introducing the tensors

$$P_{\alpha\beta}(\boldsymbol{k}) = \delta_{\alpha\beta} - \frac{k_\alpha k_\beta}{k^2} \tag{A.22}$$

$$P_{\alpha\beta\gamma}(\boldsymbol{k}) = k_\beta P_{\alpha\gamma}(\boldsymbol{k}) + k_\gamma P_{\alpha\beta}(\boldsymbol{k}) \tag{A.23}$$

Navier–Stokes equation can be written in Fourier space as:

$$\left(\frac{\partial}{\partial t} + \nu k^2\right) \hat{v}_\alpha(\boldsymbol{k}) = -\frac{i}{2} P_{\alpha\beta\gamma}(\boldsymbol{k}) \int d^3p\, \hat{v}_\beta(\boldsymbol{p}) \hat{v}_\gamma(\boldsymbol{k}-\boldsymbol{p}) \quad . \tag{A.24}$$

Let us now introduce some notations. The two-point correlation function is defined as

$$Q_{\alpha\beta}(\boldsymbol{r}) = \langle v_\alpha(\boldsymbol{x}) v_\beta(\boldsymbol{x}+\boldsymbol{r}) \rangle \tag{A.25}$$

where $\langle \ldots \rangle$ stands for the average over the volume $V$ $\langle f(\boldsymbol{x}) \rangle = \frac{1}{V} \int_V d^3x\, f(\boldsymbol{x})$. Its Fourier transform is

$$S_{\alpha\beta}(\boldsymbol{k}) = \frac{1}{(2\pi)^3} \int d^3r\, e^{-i\boldsymbol{k}\cdot\boldsymbol{r}} Q_{\alpha\beta}(\boldsymbol{r}) \tag{A.26}$$

and the correlation function in Fourier space reads

$$\langle \hat{v}_\alpha(\boldsymbol{k}) \hat{v}_\beta(\boldsymbol{k}') \rangle = \delta(\boldsymbol{k}+\boldsymbol{k}') S_{\alpha\beta}(\boldsymbol{k}) \quad . \tag{A.27}$$

The assumption of isotropy imposes for the tensor $S_{\alpha\beta}$ the form

$$S_{\alpha\beta}(\boldsymbol{k}) = A(k) k_\alpha k_\beta + B(k) \delta_{\alpha\beta} \quad , \tag{A.28}$$

where $A$ and $B$ are functions of the modulus $k = |\boldsymbol{k}|$. Multiplying Eq. (A.27) by $k_\beta$ and using incompressibility one gets $B(k) = -k^2 A(k)$, which substituted in Eq. (A.28) leads to

$$S_{\alpha\beta}(\boldsymbol{k}) = P_{\alpha\beta}(\boldsymbol{k}) B(k) \quad . \tag{A.29}$$

The energy spectrum is defined as the integral of the square modulus of velocity over a shell with fixed modulus $k$ in Fourier space:

$$E(k) = \frac{1}{2} \int k^2 d\Omega_k |\hat{\boldsymbol{v}}(\boldsymbol{k})|^2 \quad , \tag{A.30}$$

and the total energy is its integral $E = \int_0^\infty dk\, E(k)$. By definition $S_{\alpha\alpha}(\boldsymbol{k}) = \langle |\hat{\boldsymbol{v}}(\boldsymbol{k})|^2 \rangle$, but from Eq. (A.29) $S_{\alpha\alpha}(\boldsymbol{k}) = 2B(k)$, thus the following relation holds

$$B(k) = \frac{1}{4\pi k^2} E(k) \tag{A.31}$$

which gives the relation between the energy spectrum and the Fourier transform of two-point correlation function:

$$S_{\alpha\beta}(\boldsymbol{k}) = \frac{E(k)}{4\pi k^2} P_{\alpha\beta}(\boldsymbol{k}) \quad . \tag{A.32}$$

The temporal derivative of the two-point correlation function is obtained from Navier–Stokes equation as

$$\begin{aligned} \left(\frac{\partial}{\partial t} + 2\nu k^2\right) S_{\alpha\beta}(\boldsymbol{k}) \;&=\; -\frac{i}{2} P_{\alpha\rho\sigma}(\boldsymbol{k}) \int d^3p\; T_{\beta\rho\sigma}(-\boldsymbol{k}, \boldsymbol{p}) \\ &\quad -\frac{i}{2} P_{\beta\rho\sigma}(-\boldsymbol{k}) \int d^3p\; T_{\alpha\rho\sigma}(\boldsymbol{k}, \boldsymbol{p}) \quad , \end{aligned} \tag{A.33}$$

where the three-point correlation function has been introduced

$$\langle \hat{v}_\alpha(\boldsymbol{k})\hat{v}_\beta(\boldsymbol{k}')\hat{v}_\gamma(\boldsymbol{k}'')\rangle = \delta(\boldsymbol{k}+\boldsymbol{k}'+\boldsymbol{k}'')T_{\alpha\beta\gamma}(\boldsymbol{k},\boldsymbol{k}') \quad . \tag{A.34}$$

The energy balance is obtained from Eq. (A.33) remembering the relation (A.32) between the energy spectrum and the two-point correlation function. Using the antisymmetry $P_{\alpha\beta\gamma}(-\boldsymbol{k}) = -P_{\alpha\beta\gamma}(\boldsymbol{k})$ and the reality condition $T_{\alpha\beta\gamma}(-\boldsymbol{k},\boldsymbol{p}) = T^*_{\alpha\beta\gamma}(\boldsymbol{k},-\boldsymbol{p})$ one gets

$$\left(\frac{\partial}{\partial t} + 2\nu k^2\right) E(k) = T(k) \tag{A.35}$$

where the *energy transfer* $T(k)$ has been introduced:

$$T(k) = -4\pi k^2 k_\rho Im\left\{\int d^3p\, T_{\sigma\rho\sigma}(\boldsymbol{k},\boldsymbol{p})\right\} \quad . \tag{A.36}$$

Defining the *enstrophy spectrum* as:

$$Z(k) = \frac{1}{2}\int k^2 d\Omega_k |\hat{\boldsymbol{\omega}}(\boldsymbol{k})|^2 = k^2 E(k) \tag{A.37}$$

and restoring the external force $\boldsymbol{f}$ in Navier–Stokes equation, the energy balance can be rewritten as

$$\partial_t E(k) = -2\nu Z(k) + T(k) + F(k) \tag{A.38}$$

where $F(k)$ is the injection energy spectrum:

$$F(k) = \int k^2 d\Omega_k \hat{\boldsymbol{v}}(\boldsymbol{k})\cdot\hat{\boldsymbol{f}}(\boldsymbol{k}) \quad . \tag{A.39}$$

If the external forcing is a Gaussian process $\delta$-correlated in time, whose statistics is determined by the correlation $\langle f_i(\boldsymbol{x},t)f_j(\boldsymbol{x}',t')\rangle = F(|\boldsymbol{x}-\boldsymbol{x}'|)\delta_{ij}\delta(t-t')$, the input of energy is flow independent, i.e., the injection energy spectrum $F(k)$ is uniquely determined by the statistics of the forcing. In the case of a large-scale forcing, with a forcing correlation length $L$ such that

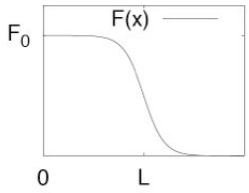


$$F(x) \simeq F_0 \quad for \quad x < L \tag{A.40}$$

$$F(x) \simeq 0 \quad for \quad x > L \tag{A.41}$$

the injection spectrum will dominate the energy balance at small wave-numbers $k \sim k_f \sim 1/L$. On the contrary the viscous dissipation, being proportional to $\nu Z(k) = \nu k^2 E(k)$, will give strong contribution at large wave-numbers, where $k^2$ is large. In the intermediate range of wave-numbers, where both injection and dissipation of energy are negligible, the dominant term in Eq. (A.38) is the energy transfer $T(k)$. In this *inertial range* the energy is conserved and transferred by triadic interaction between modes with wave-numbers such that $\boldsymbol{k}+\boldsymbol{k}'+\boldsymbol{k}'' \simeq 0$.

## A.2 Phenomenology of turbulence

In the previous section the role of the nonlinear term in Navier–Stokes equation is shown to be responsible for the production of small scales and to correspond to an energy transfer in Fourier space between modes in the inertial range.
A different approach bringing the same results is the phenomenological one. This substantially consists in dimensional arguments, able to catch some essential features of turbulence.

### A.2.1 Turbulent cascade

The basic phenomenology of turbulence can be recovered by using the picture of the *turbulent cascade* proposed by Richardson [123].
The kinetic energy is supposed to be injected by an external forcing which sustains the motion of large-scale eddies. These structures are deformed and stretched by the fluid dynamics, until they break into smaller eddies, and the process is repeated so that energy is transported to smaller and smaller structures. Finally, at small scales the kinetic energy is dissipated in the form of heat by the action of viscosity. The whole process (sketched in Fig. A.2) of energy transfer from the large scale of injection to the small dissipative scale, through the hierarchy of eddies, is known as turbulent cascade. It is worthwhile to remember that the eddies must not be thought of as real vortices, but just as a metaphoric description of the triadic interaction between modes which has been formally derived in the previous section.

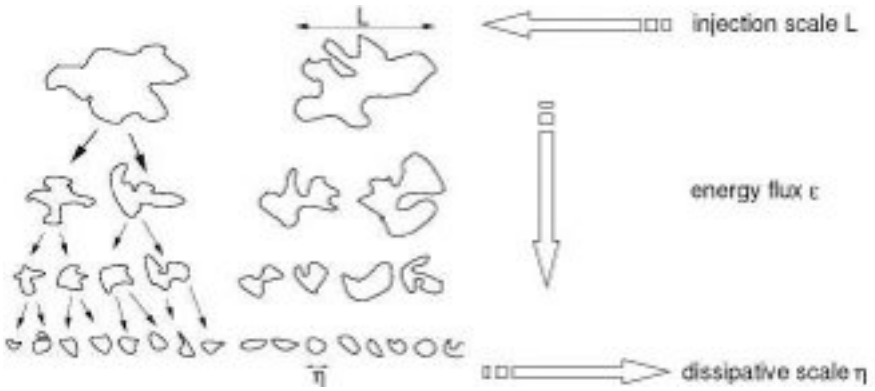


**Figure A.2:** Turbulent cascade à la Richardson. About the cascade process, a poem by Richardson [123]: *"Big whorls have little whorls that feed on their velocity, and little whorls have lesser whorls and so on to viscosity."*.

Let $v_r$ be the r.m.s. velocity at scale $r$ and $\tau_r \sim r/v_r$ the time required to transfer energy from scales of order $r$ to smaller ones.
Dimensional analysis of the different terms in Navier–Stokes equation allows to identify three different ranges of scales:

**Injective range** which corresponds to the large scales where the forcing injects the energy.

**Inertial range** where the time required for energy transfer is shorter than the dissipative time $\tau_r << \tau_r^{diss}$ and the energy is thus conserved and transported to smaller scales.

**Dissipative range** where the energy dissipation overcomes the transfer and the cascade is stopped.

The hypothesis of a statistically steady state for the turbulent cascade requires a constant energy flux $\Pi(r)$ in the inertial range, i.e. a constant rate of energy transfer that must be equal to the energy dissipation rate $\epsilon$:

$$\Pi(r) \sim \frac{E(r)}{\tau_r} \sim v_r^2 \frac{v_r}{r} = \epsilon \quad . \tag{A.42}$$

The above relation determines the Kolmogorov scaling for characteristic velocities and times:

$$v_r \sim \epsilon^{1/3} r^{1/3} \tag{A.43}$$
$$\tau_r \sim \epsilon^{-1/3} r^{2/3} \quad . \tag{A.44}$$

The border between the inertial and dissipative range is identified by the *Kolmogorov scale* $\eta$, where the dissipative and transfer times are equal $\tau_r = \tau_r^{diss}$:

$$\eta \sim \epsilon^{-1/4} \nu^{3/4} \quad . \tag{A.45}$$

Below the Kolmogorov scale, the viscous linear term dominates the evolution of the fluid, and the resulting velocity field is smooth and differentiable.

### A.2.2 The Kolmogorov theory (K41)

There is no fully deductive theory which starts from the Navier–Stokes equation and explains the basic experimental observation of finite energy dissipation rate and power-law spectrum of exponent $-5/3$, in the limit of very large Reynolds number. Nevertheless, it is possible to make assumptions compatible with these laws and leading to further predictions. In Kolmogorov 1941 theory (K41) [79, 80], hypotheses are formulated as to reproduce the experimental behaviour of the energy spectrum. If $\delta v_r(\boldsymbol{x}) \equiv [\boldsymbol{v}(\boldsymbol{x}+\boldsymbol{r}) - \boldsymbol{v}(\boldsymbol{r})] \cdot \boldsymbol{r}/|\boldsymbol{r}|$ is the longitudinal velocity increment, then the $p$th moment of its distribution:

$$S_p(r) \equiv \langle (\delta_r v)^p \rangle \tag{A.46}$$

is called longitudinal *structure function* of order $p$.
The basic assumption of the Kolmogorov theory is the *Similarity Hypothesis*. The Kolmogorov hypothesis assumes that if the inertial range is large enough, the influence of the large scale forcing and the small-scale viscous dissipation can be neglected, and the scale invariance of Navier–Stokes equation in the inviscid limit:

$$t, \boldsymbol{r}, \boldsymbol{v} \mapsto \lambda^{1-h} t, \lambda \boldsymbol{r}, \lambda^h \boldsymbol{v} \quad \lambda \in \mathbb{R}_+, h \in \mathbb{R} \tag{A.47}$$

is recovered by the turbulent velocity field in a statistical sense. The velocity fluctuations at a scale $r$ within the inertial range are supposed to be self-similar

$$\delta v_{\lambda r} \sim \lambda^h \delta v_r \tag{A.48}$$

i.e., their probability distributions are supposed to be identical once they are rescaled according to the scaling exponent $h$, and the structure functions in the limit $\mathcal{R}e \to \infty$ are expected to display a power-law behaviour as

$$S_p(r) = \langle (\delta v_r)^p \rangle \sim r^{hp} \quad . \tag{A.49}$$

Starting from the Karman-Howarth-Monin relation [101] Kolmogorov derived an exact result for the third-order structure function, the famous

**four-fifths law** *In the limit of infinite Reynolds number, the third-order (longitudinal) structure function of homogeneous isotropic turbulence, evaluated for increments $r$ small compared to the integral scale, is given in terms of the mean energy dissipation per unit mass $\epsilon$ by*

$$S_3(r) \equiv \langle (\delta v_r)^3 \rangle = -\frac{4}{5}\epsilon r \quad . \tag{A.50}$$

The four-fifths law allows to fix the value of the scaling exponent $h = 1/3$ and together with the scaling hypothesis for the structure functions leads to the Kolmogorov scaling law:

$$S_p(r) = C_p \epsilon^{p/3} r^{p/3} \tag{A.51}$$

where $C_p$ is a dimensionless constants not known, except for the universal value $C_3 = -4/5$. An interesting case corresponds to $p = 2$. The scaling of second-order structure function implies the following power-law energy spectrum

$$E(k) \equiv 2\pi k \langle |\hat{\boldsymbol{v}}(\boldsymbol{k})|^2 \rangle = C_2 \epsilon^{2/3} k^{5/3} \quad . \tag{A.52}$$

Spectra, as the previous prediction, have been observed in many different physical situations, from the experiments in tidal channel [67] which gave the first confirmations of the Kolmogorov theory, to more recent measurements in wind-tunnel experiments [30] (see Fig. A.3) and in low-temperature helium gas flows between counter-rotating cylinders [97].

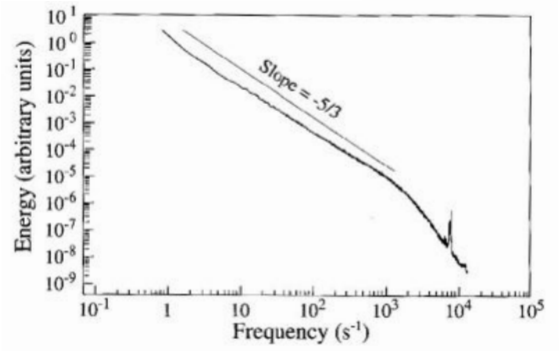


**Figure A.3:** Turbulent spectra for data from the S1 wind tunnel ONERA [30].

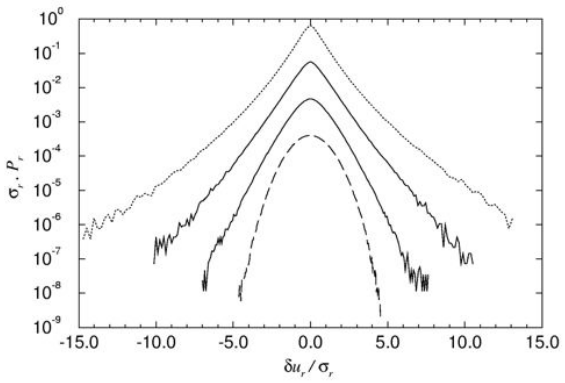


**Figure A.4:** Probability distributions, normalised with their standard deviations $\sigma_r = \langle(\delta_r v)^2\rangle^{1/2}$, of velocity increments in a turbulent air jet for different separations: in correspondence of viscous scale (dotted line), large scale which is shifted of three decades (long dashed line), and intermediate scales (solid lines) [96].

### A.2.3 Intermittency

The basic assumption of Kolmogorov K41 theory is the self-similarity of the turbulent flow in the inertial range. Nevertheless, experimental turbulent signals, once high-pass filtered, typically reveal intermittent features: their activity is restricted to only a fraction of the time, which decreases with the time scale under consideration. In other words, the velocity field can be thought of as a random alternation of quiet periods and chaotic bursts of intense fluctuations.

These intermittent features are reflected in the shape of the probability distribution function (PDF) of velocity increments (see, for instance, Fig. A.4). Experimental data (for example, [74, 96]) show that the obtained PDFs have different shapes. Indeed, it is essentially Gaussian at large scales but, as the scale gets smaller, it develops higher and higher tails accounting for larger and larger probabilities of strong fluctuations. Near the Kolmogorov dissipative scale, the PDF takes the shape of a stretched exponential. Therefore, the PDF of the velocity increments at various scales cannot be collapsed onto one another by simple rescaling. The statistical properties of the velocity at a certain scale cannot be obtained by a simple rescaling of the statistics at another scale. This behaviour means that the statistics is not scale invariant.

More precisely, the measurements of high-order structure functions [133], because they supply information on the distribution tails, allowed to detect the intermittent nature of the turbulent velocity field. The results suggest that the structure functions follow power laws in the inertial range:

$$S_p(r) = \langle(\delta v_r)^p\rangle \sim r^{\zeta_p} \quad , \tag{A.53}$$

but the scaling exponents differ from the dimensional $K41$ prediction $\zeta_p = p/3$ and they are a nonlinear concave function of the order $p$. The violation of the dimensional predictions for the scaling laws is referred to as *anomalous scaling*, because it reflects a symmetry rupture of the statistics[1].

The intermittency introduces some issues: what are the physical mechanisms ruling the

[1] In order to describe the intermittency, phenomenological models have been formulated. For a review on this subject, see Chap. 8 in [60].

intermittency? What is really universal in the inertial-interval statistics? Universality means independency of the conditions of excitations and dissipation.
The analysis is complicated by the non-equilibrium nature of turbulence. An important step in general understanding of turbulence has been made by investigating the problem of the passive scalar (see Sec. A.4.1).

## A.3 Two-dimensional turbulence

**Figure A.5:** Two-dimensional turbulence. Photograph of experiment carried out with a soap film (from `http://maartenrutgers.org`). A soap film is a solution of water and a liquid detergent. In this Figure the gravity is from top to bottom. The film is bounded by two vertical nylon wires, and originates about one meter above the photographed area from a bottle of soap solution. At the top of the photograph a comb punctures the film. For a review, also see [78].

Two-dimensional turbulence describes the behaviour of high-Reynolds-number solutions of Navier–Stokes equation which depends only on two Cartesian coordinates, for instance $(x, y)$. In this case, the third component of the velocity satisfies an advection-diffusion equation without back-reaction on the horizontal $(x, y)$ flow. Hence, without loss of generality, one may assume that the velocity has only two components.
The study of two-dimensional incompressible flows at high Reynolds numbers presents several reasons of interest. A principal reason is provided by its relevance for geophysics. Indeed, the intermediate-scale dynamics of oceans and atmosphere, because of the combined effects of their stratification and the earth rotation, can be roughly described as a two-dimensional flow. Another reason comes from plasma physics, where the presence of a strong mean magnetic field can confine the turbulent motions of plasma in the plane perpendicular to the magnetic field, and again the dynamics can be described by two-dimensional magneto-hydrodynamics (2D MHD) [18].
The classical theory of two-dimensional turbulence originates from the works of Batchelor, Kraichnan and Leith [9, 83] and [85] (see also references therein), which showed that the conservation of vorticity along the streamlines, which occurs in two dimensions, produces

radical changes in the behaviour of turbulence.
Far from being a simplified version of the three-dimensional problem, two-dimensional turbulence presents a rich panorama of new phenomena, like the formation of coherent vortices from an initially disordered "sea" of vorticity, which have attracted a large interest.
Finally, Navier–Stokes equation in two dimensions has the appealing feature to be less demanding on a computational level than the three-dimensional case, allowing to reach relatively high $\mathcal{Re}$ numbers in Direct Numerical Simulations.
A recent review on the two-dimensional turbulence is offered in [136].

### A.3.1 Vorticity equation in two dimensions

In two dimensions, the incompressible velocity field $\boldsymbol{v}$ can be expressed in terms of the *stream function* $\psi$ as:

$$\boldsymbol{v} = (\partial_y \psi, -\partial_x \psi) \quad . \tag{A.54}$$

The vorticity field, defined as the curl of velocity, $\boldsymbol{\omega} = \boldsymbol{\partial} \times \boldsymbol{v}$, in two dimensions has only one non-zero component which is orthogonal to the plane of velocity and is related to the stream-function by

$$\omega = -\partial^2 \psi \quad . \tag{A.55}$$

Thus instead of giving a description of the flow in term of the two components of velocity, which are not independent because of the incompressibility condition, it is convenient to rewrite the two-dimensional Navier–Stokes equation in terms of the vorticity scalar field:

$$\frac{\partial \omega}{\partial t} + \boldsymbol{v} \cdot \nabla \omega = \nu \nabla^2 \omega + f_\omega \quad . \tag{A.56}$$

The term $f_\omega$ represents the external source of energy acting on the largest scales – e.g. stirring. This term counteracts the dissipation by viscosity $\nu$ and allows to obtain a statistically steady state.
To solve Eq. (A.56) it is necessary to specify a set of boundary conditions which are required to solve the Poisson equation (A.55) for the stream function. In most studies on two-dimensional turbulence, periodic boundary conditions are assumed in both the two directions. The presence of realistic no-slip boundaries gives origin to a source of vorticity fluctuations.

### A.3.2 Inviscid invariants and cascades

The main difference with the three-dimensional case is the conservation of vorticity along fluid trajectories when viscosity and external forcing are ignored.
The origin of this phenomenon is due to the vanishing in two dimensions of the so-called "vortex stretching term" $(\boldsymbol{\omega} \cdot \boldsymbol{\partial})\boldsymbol{v}$ that appears as a forcing term in the evolution equation for vorticity in the three-dimensional case where it is responsible for the unbounded growth of enstrophy in the limit $\mathcal{Re} \to \infty$.
In the inviscid limit $\nu = 0$ and in the absence of external forcing and friction, the vorticity equation simply states that the derivative of the vorticity along the fluid trajectories vanishes

$$\frac{D\omega}{Dt} = \frac{\partial \omega}{\partial t} + \boldsymbol{v} \cdot \boldsymbol{\partial} \omega = 0 \tag{A.57}$$

which means that since the vortex stretching is absent the vorticity of a fluid parcel is conserved. Moreover, in two dimensions the enstrophy is bounded by the energy balance equation, which is obtained from Eq. (A.56) in the absence of external forcing $f = 0$, and assuming periodic boundary conditions:

$$\frac{dZ}{dt} = -\nu \int d^2x \, \rho |\boldsymbol{\partial}\omega|^2 \quad . \tag{A.58}$$

Therefore, at variance with the three-dimensional case, in two-dimensional turbulence the viscous dissipation of energy vanishes in the limit $\nu \to 0$

$$\lim_{\nu \to 0} \frac{dE}{dt} = \lim_{\nu \to 0} -2\nu Z = 0 \quad . \tag{A.59}$$

Since the viscous energy dissipation vanishes in the limit $\mathcal{R}e \to \infty$, in fully developed two-dimensional turbulence, it is impossible to have a cascade of energy with constant flux toward small scales.

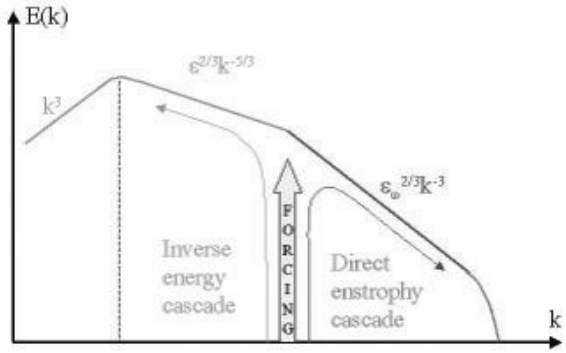


**Figure A.6:** Schematic double cascading spectrum of forced two-dimensional turbulence

In the sixties, two contributions, given independently by Kraichnan and Batchelor, stimulated comprehension of the two-dimensional turbulence and research in this field. Batchelor proposed that cascades may develop in the plane, in a way analogous to the direct energy cascade in three dimensions, with the enstrophy playing the role of the energy [9]. In 1967, Kraichnan [83], discovered the double cascade process. In two-dimensional turbulence the enstrophy is mainly transferred to high wavenumbers where it is dissipated by viscosity, giving rise to the *direct enstrophy cascade*. On the contrary, the energy is transported to lower wavenumbers in the *inverse energy cascade* (see Fig. A.6).
The scaling laws in both cascades can be obtained from dimensional analysis of Navier–Stokes equation as well as in the three-dimensional case.
For the inverse energy cascade, the assumption of constant energy flux $\Pi(r) = -\epsilon$ towards large scales reproduces 3D-like scaling laws for velocities:

$$\delta_r v \sim \epsilon^{1/3} r^{1/3} \quad . \tag{A.60}$$

This means that the velocity field in the inverse cascade is rough, with scaling exponents $h = 1/3$, exactly as the three dimensional case. The prediction for the energy spectrum is:

$$E(k) \sim \epsilon^{2/3} k^{-5/3} \quad . \tag{A.61}$$

In the absence of large-scale sink of energy, the energy cascade can only be quasi-steady because the peak of the energy spectrum keeps moving down to lower and lower wavenumbers[2]. Then, if the energy input is turned on for a sufficiently long time, the cascade can eventually reach the integral scale and begins to accumulate at the lowest wavenumber. In such a situation, the way the energy is eventually burned depends on the system. In practice, in physical experiments, energy is dissipated by friction along the walls limiting the system (see [136] and references therein). This corresponds to a constant Ekman friction term $-\alpha\omega$ added to the r.h.s. of Eq. (A.56). As a consequence, in the spectrum, a $k^{-3}$ range is observed at largest scales[3]. Physically, the inverse cascade is an aggregation process, driving the formation of large clusters of like-sign vortices, which sustain large eddies conveying the energy towards larger scales. Vortices are continuously nucleated by the forcing; these vortices have sizes of the injection scale. Soon after they are formed, they wander in the plane, get distorted and strained by the action of neighboring vortices, and thus tend, on average, to aggregate with other vortices.
The analogue of the K41 energy cascade towards small scales, in the sense that the transfer develops at constant rate across the scales, is an enstrophy cascade [9, 83]. In the range of scales defined as the inertial range of the problem, the energy and the enstrophy spectra, dimensionally constrained, have the following expression:

$$E(k) \sim \epsilon_\omega^{2/3} k^{-3} \tag{A.62}$$
$$Z(k) \sim \epsilon_\omega^{2/3} k^{-1} \quad , \tag{A.63}$$

where $\epsilon_\omega$ is the enstrophy flux. On physical grounds, the process prevailing in the cascade is essentially the elongation of the vorticity patches (see also [60, 136]).
At variance with the three-dimensional case, where the dimensional prediction for the scaling exponents is modified by the presence of small-scale intermittency, the statistics of velocity fluctuations at different scales $r$, in the scaling range of the inverse energy cascade, are found to be roughly self-similar [21, 108], with small deviations from Gaussianity.

## A.4 Scalar turbulence

A substance advected by a turbulent flow exhibits a complex, chaotically evolving structure over a broad range of space and time scales. The turbulent advection is encountered in many natural phenomena [110] and engineering problems ranging from atmospheric physics and combustion [52] to the transport and amplification of magnetic fields in astrophysical fluids [154].
Matematically, these substances can be described as a scalar field. Generally, according to its coupling with the flow, a scalar field can be classified into two categories: *passive* and *active* scalar. A passive scalar is a quantity that is advected by a flow without back-reacting on it. There is a variety of real transport problems that can be described through the passive-scalar

[2] Kraichnan compared this phenomenon to the Bose–Einstein condensation, a terminology which remains. The analogy is justified: in Bose–Einstein condensation, below a certain temperature, the system collapses onto a fundamental state, compatible with the boundaries of the system. In the phenomenon we discuss here, in Fourier space, the energy piles up onto the smallest wavenumbers, compatible with the boundaries. There are several observations of the condensation process (see, for instance, [130]).

[3] The scaling $k^{-3}$ corresponds to a balance of nonlinear transfer with friction.

scheme. This happens every time the reaction of some particular quantity on the carrying flow can be disregarded, like for dilute dyes, pollutants dispersed in a fluid or temperature in the case where buoyancy forces are negligible. Conversely, when the scalar field can influence the velocity field, this is dubbed active scalar field. This is the case, for instance, of the temperature field that acts on velocity field through buoyancy force.
Although active and passive scalars are governed by the same advection-diffusion equation,

$$\partial_t T + \boldsymbol{v} \cdot \boldsymbol{\partial} T = \kappa \partial^2 T + f_T \tag{A.64}$$

(where $\kappa$ is the molecular diffusivity and $f_T$ an external forcing) their nature is radically different. Passive scalars belong to the realm of linear problems, despite being highly non-trivial. However, in respect of the issue of universality and scaling, the passive-scalar problem is essentially understood. On the contrary, for active fields, the presence of the feedback which couples the velocity with the transported scalar, makes the problem fully nonlinear. The active problem is a challenging open problem. For a review see [31].

In the following sections we briefly recall the phenomenology of both the passive scalar and the active scalar in the case of two-dimensional thermal convection.

### A.4.1 Passive scalar

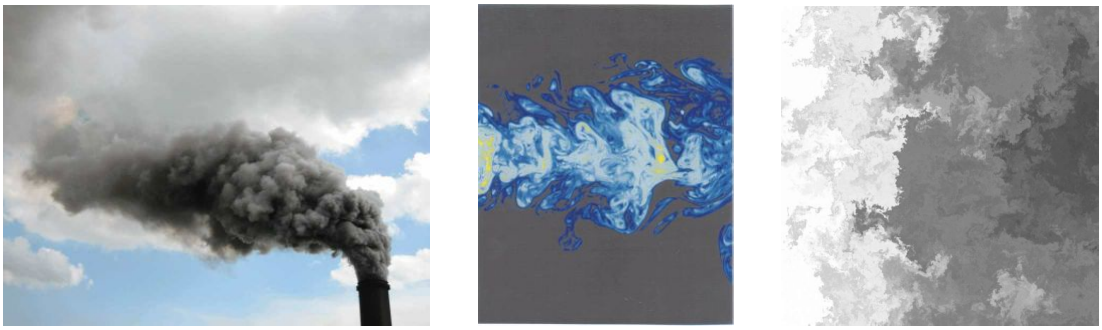

**(a)** **(b)** **(c)**

**Figure A.7:** Some examples of passive scalar. **(a)** Instances of real scalar turbulence, and **(b)** as obtained by experiments of a fluorescent dye in a turbulent jet [132]. **(c)** Snapshot of temperature field as obtained by means of Direct Numerical Simulations. The scalar field is advected by a two-dimensional Navier–Stokes turbulence in the inverse cascade regime. Moreover the scalar turbulence is maintained by a fixed temperature gradient directed from right to left. Colours are coded according to the intensity of the scalar field: white corresponds to large positive values, black to large negative values [33].

Let us consider passive-scalar transport by a turbulent incompressible carrier flow $\boldsymbol{v}$, ruled by the advection-diffusion equation (A.64).
The scalar dynamics and the three-dimensional Navier–Stokes present a very similar behaviour. In the absence of injection and dissipation, the variance of scalar density $\langle T^2/2 \rangle$ is conserved. In their presence, a steady state might be established. Typically, the forcing

$f_T$ injects scalar fluctuations at a certain spatial scale $L_T$, dramatically separated from the scale $\eta_T$, where diffusion processes are active. In this case, the advection term $\boldsymbol{v}\cdot\boldsymbol{\partial}T$, in Eq. (A.64), provides a small-scale cascade process that does not modify the input-output balance between injection and dissipation, but only transfer scalar fluctuations from large scales to small scales [4]. The interval between the injection and the diffusive scales is called *convective range*. The turbulent cascades of the conserved quantities $\langle|\boldsymbol{v}|^2/2\rangle$ and $\langle T^2/2\rangle$ take place in the so-called *inertial-convective* range of scales, where research has focused its main interest. In this range of scales, the Kolmogorov argument was extended to the passive scalar by Obukhov and Corrsin ( [101] and references therein). Under the hypothesis of scale invariance, dimensional predictions give:

$$(\delta_r v)^p \sim \epsilon^{p/3} r^{p/3} \tag{A.65}$$

$$(\delta_r T)^p \sim \epsilon_T^{p/2}\epsilon^{-p/6} r^{p/3} \quad , \tag{A.66}$$

where $\epsilon_T \equiv \kappa\langle|\boldsymbol{\partial}T|^2\rangle$ is the rate of scalar-energy dissipation.
Together with a cascade, a peculiar phenomenology appears with a breakdown of scale invariance, that is, the intermittency phenomenon (see, for instance, [128, 142]). This manifests itself in the presence of a quasi-discontinuous spatial structure for the scalar field: it presents strong variations across tiny regions, the so-called fronts, separated by large regions where scalar fluctuations are weak [32, 33, 132, 142] (see, for instance, Fig. A.7).
The anomalous scaling exponents are found to be universal with respect to the details of the energy injection [31] (and references therein). The observation that the passive scalar and the velocity dynamics are similar strongly suggested that research could obtain information on Navier–Stokes by studying the simpler problem of passive-scalar transport. A great advancement in this sense was achieved with the introduction of the Kraichnan model of passive advection [84]. The key point of passive-scalar success is the observation that its intermittency is much more pronounced than the intermittency of the velocity field. This hints to the possibility that the scalar field could be intermittent in the absence of any intermittency of the carrier flow. The Kraichnan model studies the evolution of a passive scalar advected by an incompressible, random,Gaussian, scale-invariant, $\delta$-correlated-in-time flow. This particular choice allows for a thorough analytical investigation of the model. The result is that, despite the absence of any intermittency of the carrier flow, this problem displays scalar intermittency. Most importantly, the anomalous scaling has been traced to the existence of statistical integrals of motion that can be found as zero modes of partial differential operators [36, 42, 58, 63].

### A.4.2 Two-dimensional thermal convection: Bolgiano–Obukhov theory

An interesting problem in the context of turbulent transport is the advection of inhomogeneous temperature field in a gravitational field. Temperature fluctuations induce density fluctuations, which in turn, via buoyancy forces, affect the velocity field: hence the temperature field is an active scalar [101, 129]. The equations ruling the fluid evolution are

[4] Yaglom (1949) [145] derived the following relation for the flux of the density scalar energy:

$$\langle\{[\boldsymbol{v}(\boldsymbol{r}+\boldsymbol{x},t)-\boldsymbol{v}(\boldsymbol{x},t)]\cdot\boldsymbol{r}/|\boldsymbol{r}|\}\,[T(\boldsymbol{r}+\boldsymbol{x},t)-T(\boldsymbol{x},t)]^2\rangle = -\frac{4}{3}\epsilon_T\, r \quad ,$$

where $\epsilon_T \equiv \kappa\langle|\boldsymbol{\partial}T|^2\rangle$ is the scalar dissipation.

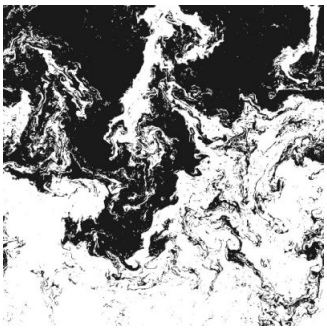

**Figure A.8:** Two-colour coded image of the temperature field. Black (white) regions represent cold (warm) fluid. The gravity points from top to bottom. A linear mean profile is assumed, with a large-scale gradient pointing downward as the gravity. Two-dimensional Direct Numerical Simulations from [35].

the advection-diffusion equation (A.64) and the Navier–Stokes equation in the Boussinesq approximation (see, for instance, [86]): the velocity is forced by the buoyancy term $-\beta \boldsymbol{g} T$, where $\beta$ is the thermal-expansion coefficient and $\boldsymbol{g}$ the gravity acceleration.
Let us briefly recall the phenomenology of two-dimensional convection (for the three - dimensional case, see e.g. [129]). The balance of buoyancy and inertial terms introduces the Bolgiano length scale $r_B$ (see [101] and references therein). At small scales $r \ll r_B$, the inertial term is larger than buoyancy forces and the temperature is basically a passive scalar. At larger scales $r \gg r_B$, buoyancy dominates and affects the velocity, which performs an inverse energy cascade in two dimensions. However, at variance with the usual two-dimensional Navier–Stokes turbulence, the kinetic-energy input rate $\epsilon$ depends here on the scale, and is not restricted to small scales. Indeed, the energy input rate $\epsilon(r) = \beta \boldsymbol{g} \cdot \langle \boldsymbol{v}(\boldsymbol{r}+\boldsymbol{x},t) T(\boldsymbol{x},t) \rangle$ grows with the scale as $\epsilon(r) \sim r^{4/5}$. In that range, the temperature fluctuations cascade, at a constant rate $\epsilon_T$, towards the small scales where they are eventually dissipated by thermal diffusivity. Dimensional arguments, based on this phenomenological picture, would lead to the Bolgiano–Obukhov scaling (see, i.e., [101] and references therein):

$$(\delta_r v)^p \sim (\epsilon(r)\, r)^{p/3} \sim r^{3p/5} \tag{A.67}$$

$$(\delta_r T)^p \sim \epsilon_T^{p/2} \epsilon(r)^{-p/6} r^{p/3} \sim r^{p/5} \quad . \tag{A.68}$$

Actually, due to the presence of structures of warm-rising or cold-descending fluid, i.e., the thermal plumes (see Fig. A.8), the statistics of temperature increments exhibits a nontrivial scale dependence. Indeed the moments of temperature increments display a scaling behaviour characterised by exponents deviating from the dimensional expectations. Conversely, the moments of velocity increments do not show measurable deviations from dimensional scaling [34, 35]. Recently, all the numerical evidences converge to the following global picture of scaling and universality in two-dimensional turbulent convection. Velocity statistics is strongly universal with respect to the temperature external driving $f_T$. Temperature statistics shows anomalous scaling exponents that are universal and coincide with those of a passive scalar evolving in the same flow [31, 34] (and references therein). However, the equivalence of the statistics of an active scalar, such as temperature, to that of a passive scalar depends crucially on the universality of the whole velocity statistics found and the equivalence appears to be a non generic situation [31].

# Appendix B

# The pseudo-spectral method

*"... said the little technician earnestly, ≪... Now seven times three is twenty-one.≫*
*≪And how do you know that?≫asked the congressman.*
*≪I just remember it. It's always twenty-one on the computer. I've checked it any number of times..."*
Feeling of Power by Isaac Asimov (novel 1957)

The aim of this appendix is to briefly explain the use of the pseudo-spectral code to numerically integrate the Navier–Stokes equation in a spatial region with periodic boundary conditions. Hence, the set of PDE that must be integrated are:

$$\begin{cases} \partial_t \boldsymbol{v} + \boldsymbol{v} \cdot \boldsymbol{\partial} \boldsymbol{v} = -\boldsymbol{\partial} p + \nu \partial^2 \boldsymbol{v} + \boldsymbol{f} \\ \boldsymbol{\partial} \cdot \boldsymbol{v} = 0 \end{cases} \tag{B.1}$$

where $p$ is the pressure, $\nu$ is the kinematic viscosity and $\boldsymbol{f}$ represents an external forcing. The solution of the problem requires to specify:

- boundary conditions
- initial conditions.

For what concerns the former point, periodic boundary conditions, i.e. $v_i(x + L) = v_i(x)$, are assumed. This choice is convenient both for physical reasons (in a homogeneous flow far from boundaries one can look for universal behaviour) and for numerical reasons (simple and efficient code). Assuming periodic boundary conditions fixes the discretization (uniform) and the Fourier representation of the velocity field.

Useful textbooks are [29, 115].

## B.1 Fourier transforms and FFT

Let us consider for simplicity a scalar field $v$ discretized on $N$ points $x_i = i\delta x$ with $\delta x = L/N$ and $i = 0, \ldots, N-1$. The direct and inverse Fourier transforms are

$$v_n = \sum_{k=-N/2}^{N/2} \hat{v}_k e^{i\frac{2\pi}{N}nk} \tag{B.2}$$

$$\hat{v}_k = \frac{1}{N} \sum_{n=0}^{N-1} v_n e^{-i\frac{2\pi}{N}nk} \tag{B.3}$$

where $v_n = v(x_n)$ and $\hat{v}_k$ is the Fourier component at wavenumber $k$. Because of the discretization one has $\hat{v}_{N-k} = \hat{v}_{-k}$ and the Nyquist frequency (i.e., the highest representable frequency ) is $k = N/2$ [38].
With the normalisation factors in (B.3), the Parseval identity is written as

$$\sum_{n=0}^{N-1} |v_n|^2 = N \sum_{k=1}^{N-1} |\hat{v}_k|^2 \tag{B.4}$$

and thus, introducing the average as $\langle v \rangle \equiv \frac{1}{L}\int_0^L dx v(x)$, the kinetic energy can be written as

$$E \equiv \frac{1}{2}\langle v^2 \rangle = \frac{1}{2} \sum_{k=1}^{N-1} |\hat{v}_k|^2 \quad . \tag{B.5}$$

In the case of a real field $v \in \mathbb{R}$, from (B.3) one has the reality conditions $\hat{v}_{-k} = \hat{v}_k^*$ and thus the Fourier representation only requires the positive wavenumbers. Observing that both $\hat{v}_0$ and $\hat{v}_{N/2}$ are obviously real, the actual number of independent real variables is only $N$, as expected.
In the three-dimensional case the Fourier transform $\hat{v}(k_x, k_y, k_z)$ involves in general $N^3$ complex components. If $v \in \mathbb{R}$ one can again reduce the components by a factor 2. For simplicity, most of the multidimensional Fourier transforms consider the following wavenumbers

$$k_y, k_z \in \left[-\frac{N}{2} - 1, \ldots, 0, \ldots, \frac{N}{2}\right] \tag{B.6}$$

$$k_x \in \left[0, \ldots, \frac{N}{2}\right] \tag{B.7}$$

thus, for a total of $N^2(N+2)$ real numbers. This representation thus uses more memory than what is necessary ($N^3$ real numbers) but the resulting code is much simpler, as the codification of the Fourier transform in $N^3$ real numbers is much more complex than in the $1D$ case.

### B.1.1 Fast Fourier Transform

Let us come back to the one-dimensional transform (B.3). The evaluation of the Fourier transform $\hat{v}_k$ for all the values of $k$ requires $N^2$ operations (essentially the two "do" cycles

on $k$ and $n$). This is numerically very expensive, especially when $N$ is large or in more dimensions.
The idea of FFT is to drastically reduce the number of operations. The idea was already discovered by Gauss (1805) and then developed by by Danielson & Lanczos in 1942 [49]. The method became popular after the work of Cooley & Tuket in 1965 [47]. In the following we will illustrate the basic idea following Danielson & Lanczos. Let us write the Fourier series in (B.3) as a sum of two terms, one corresponding to odd $n$ and the other to even $n$:

$$\hat{v}_k = \sum_{n=0}^{N/2-1} e^{i\frac{2\pi}{N}k(2n)} v_{2n} + \sum_{n=0}^{N/2-1} e^{i\frac{2\pi}{N}k(2n+1)} v_{2n+1} = \tag{B.8}$$

$$= \sum_{n=0}^{N/2-1} e^{i\frac{2\pi}{\frac{N}{2}}kn} v_{2n} + e^{i\frac{2\pi}{N}k} \sum_{n=0}^{N/2-1} e^{i\frac{2\pi}{\frac{N}{2}}kn} v_{2n+1} = \tag{B.9}$$

$$= \hat{v}_k^{(\mathsf{even})} + e^{i\frac{2\pi}{N}k} \hat{v}_k^{(\mathsf{odd})} \quad . \tag{B.10}$$

In this way one has reduced the original Fourier transform on $N$ points to two Fourier transforms on $N/2$ points. But, because the number of operations is proportional to the number of points square, in the latter case one has to perform only $O(N^2/2)$ operations and thus a factor two is gained.
The idea of FFT is to repeat this splitting procedure recursively. If the number of points is a power of two, $N = 2^r$, after repeating $r$ times the procedure one obtains, with a symbolic notation:

$$\hat{v}(N) \to \left\{ \hat{v}^{(\mathsf{e})}\left(\frac{N}{2}\right), \hat{v}^{(\mathsf{o})}\left(\frac{N}{2}\right) \right\} \tag{B.11}$$

$$\to \left\{ \hat{v}^{(\mathsf{e,e})}\left(\frac{N}{4}\right), \hat{v}^{(\mathsf{e,o})}\left(\frac{N}{4}\right), \hat{v}^{(\mathsf{o,e})}\left(\frac{N}{4}\right), \hat{v}^{(\mathsf{o,o})}\left(\frac{N}{4}\right) \right\} \to \dots \tag{B.12}$$

$$\to \left\{ \dots, \hat{v}^{(\alpha_1 \dots \alpha_r)}(1), \dots \right\} \tag{B.13}$$

and hence the computation of the FFT on N points involves $O(N \ln N)$ operations.

### B.1.2 Derivatives and products

The idea of using Fourier representation on a periodic grid is that derivatives and integrals become simple multiplicative operations. From the definition (B.3), the exact Fourier representation of $\partial_x v(x)$ is simply $(2\pi/L)ik\hat{v}_k$. For simplicity, in the following we will take $L = 2\pi$. The enormous advantage of Fourier representation became evident for more complex operations such as, for example, the inversion of a Laplacian (an operation required for integrating the Navier–Stokes equation):

$$\widehat{(\nabla^{-2} v)}_k = -\hat{v}_k / k^2 \quad . \tag{B.14}$$

The drawback of Fourier representation are the nonlinear terms that become convolutions involving $O(N^2)$ operations. For example

$$v\partial_x v \overset{F}{\longmapsto} \sum_p \hat{v}(k-p) ip \hat{v}(p) \quad . \tag{B.15}$$

The idea of the pseudo-spectral method is to perform linear operations (derivatives) in Fourier space and to calculate the products of nonlinear terms in physical space. For example, the scheme for computing the term (B.15) is

$$\begin{array}{ccccc} \hat{v}(k) & \overset{FFT^{-1}}{\longmapsto} & v(x) & \searrow & \\ & & & & v\partial_x v \overset{FFT}{\longmapsto} \widehat{v\partial_x v} \\ ik\hat{v}(k) & \overset{FFT^{-1}}{\longmapsto} & \partial_x v(x) & \nearrow & \end{array} \tag{B.16}$$

and thus requires $3$ Fourier transforms. By means of efficient FFT this method is much faster than the direct evaluation of the convolution (this is indeed the usual numerical way to compute convolutions).
I conclude this section with a remark concerning efficiency. Although the computation of FFT is much faster than the direct evaluation of convolution, it is by far the most time consuming part of the numerical code. As a consequence one does not need to optimise the rest of the code for speed.

### B.1.3 Aliasing and dealiasing

The critical sampling of a sine wave is two sample points per cycle. The corresponding critical frequency is called Nyquist frequency, which is relevant for two different reasons:

- if a continuous function $v(t)$, sampled at an interval $\Delta t$, happens to be bandwidth limited to frequencies smaller in magnitude than $f_c$, i.e. if $\hat{v}(f) = 0$ for all $|f| \geq f_c$, then the function $v(t)$ is completely determined by its samples $v_n = v(n\Delta t)$. In fact $v(t)$ is given explicitly by the formula:

$$v(t) = \Delta t \sum_{n=-\infty}^{+\infty} v_n \frac{\sin 2\pi f_c(t - n\Delta t)}{\pi(t - n\Delta t)} \tag{B.17}$$

- In the case that the function $\hat{v}(f)$ is not bandwidth limited in the range $[-f_c, f_c]$ then when one performs a discrete Fourier transform the power spectral density in frequencies $|f| \geq f_c$ is spuriously moved into that range. This phenomenon is called *aliasing*.

In the Navier–Stokes jargon one can rephrase this problem in this way: the nonlinear terms generate modes that are not contained in the wavenumbers grid, and these modes are aliased (i.e. falsely translated) in the considered range. The energy related to these modes typically creates numerical instabilities.
The aliasing effect was first observed by Phillips who developed the first General Circulation Model in 1956 [112]. He observed that the code developed an instability and blew up after about $20$ days of integration, independently on the integration step. Phillips realised that his problem was due to aliasing and in 1959 proposed as a solution to filter out modes with $|k| > N/4$ [113]. Indeed, the mode $N/4$ may activate, through nonlinear terms, the maximal mode $k = N/2$ resolved by the code.
In 1971 Orszag [106] realised that the problem could be treated by dropping out less than $N/4$ modes. He suggested to filter at $N/3$: in fact the nonlinear interactions can activate

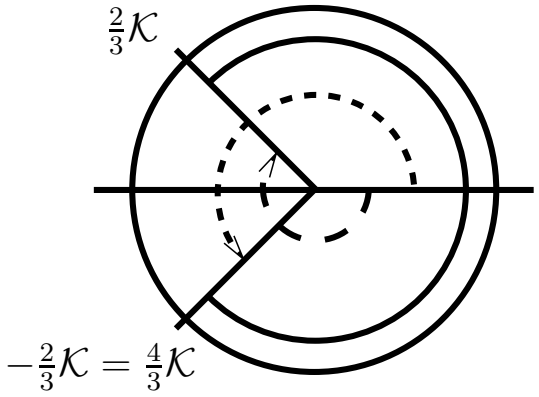


**Figure B.1:** The aliasing wheel.

modes up to $2N/3$ modes which are out of the range considered, but it can be shown that the energy of these modes does not influence the modes $k < N/3$.

In order to explain this result, let us consider the "aliasing wheel" shown in Fig.B.1 where $\mathcal{K} = N/2$ represents the maximum mode in the Fourier representation and where I indicate the lines of the filter with continuous lines. If one considers $k \in \left[-\frac{2}{3}\mathcal{K}, \frac{2}{3}\mathcal{K}\right]$, that is filtering at such $k$ that correspond to $N/3$, one obtains a possible range of modes $\left[-\frac{4}{3}\mathcal{K}, \frac{4}{3}\mathcal{K}\right]$. This interval could be splitted into three subintervals: $\left[-\frac{4}{3}\mathcal{K}, -\frac{2}{3}\mathcal{K}\right]$, $\left[-\frac{2}{3}\mathcal{K}, \frac{2}{3}\mathcal{K}\right]$, $\left[\frac{2}{3}\mathcal{K}, \frac{4}{3}\mathcal{K}\right]$. The first and the third ones are dropped out by the filter, and hence one could keep the modes that have originated them. The second one is unaltered by the filter and hence is taken into account.

I conclude this Section by recalling that in practice if the viscosity is strong one can neglect aliasing: this is motivated by the fact that the Kolmogorov dissipative scale $\eta = \left(\nu^3/\epsilon\right)^{1/4}$, is large, and the corresponding wavenumber $k_\eta = 1/\eta$ can be much smaller than $N/3$.

## B.2 Temporal discretization

We now consider some possible numerical schemes for integrating a generic ODE. Let us consider the ODE:

$$\dot{x}(t) = F(x) \quad . \tag{B.18}$$

A series of schemes, known as *implicit*, requires the knowledge of the function $F$ evaluated at the present point $t$ and also at some point in the future, such as $t + \Delta t$. Methods of this kind are normally quite efficient and precise but rather a bit complicated and therefore will not be considered here.

Among the *explicit* integration schemes, the simplest one is the Euler method which is based on the first-order Taylor expansion (and therefore is not very accurate):

$$x(t + \Delta t) = x(t) + \Delta t\, \dot{x}(t) + O(\Delta t^2) = x(t) + \Delta t F(x(t)) + O(\Delta t^2) \quad . \tag{B.19}$$

It is simple to realise that the Euler scheme is already inappropriate to integrate a simple linear equation such as $\dot{x} = -x$ as it produces oscillations around $x = 0$ and therefore non-physical negative values. While the first-order scheme is essentially unique, increasing the

order there is more freedom and several numerical algorithms can be used. In the following the so-called Runge–Kutta scheme is considered, which exists for a general order $n$ in time, and which is a good compromise between simplicity and efficience.
The second-order schemes are based on a second-order expansion:

$$x(t+\Delta t) = x(t) + \Delta t\, \dot{x}(t) + \frac{1}{2}\Delta t^2 \ddot{x}(t) + O(\Delta t^3) \quad . \tag{B.20}$$

The evaluation of the last term $\ddot{x} = (\partial F/\partial x)\, F$ differentiates among the different schemes. In the case of second-order Runge–Kutta (RK2) this is done by observing that

$$F[x + \frac{\Delta t}{2} F(x(t))] \simeq F(x) + \frac{\Delta t}{2}\frac{\partial F}{\partial x} F \tag{B.21}$$

and hence:

$$\ddot{x} \simeq \frac{2}{\Delta t}\left\{ F[x + \frac{\Delta t}{2} F(x(t))] - F(x) \right\} \tag{B.22}$$

which plugged into the (B.20) yields:

$$x(t+\Delta t) \simeq x(t) + \Delta t F[x + \frac{\Delta t}{2} F(x(t))] \quad . \tag{B.23}$$

The RK2 consists therefore in making this sequence of operations:

$$x(t) \rightarrow F(x(t)) \rightarrow \dot{x} = x + \frac{\Delta t}{2} F(x(t)) \tag{B.24}$$

$$\Rightarrow x(t+\Delta t) = x(t) + \Delta t F(\dot{x}) \quad . \tag{B.25}$$

One observes that the increase in accuracy is paid by the fact that one needs to evaluate the r.-h.s. of Eq. (B.18) twice. In general, increasing the order of the scheme requires an increasing number of calls to the function $F$, thus resulting in a slower procedure (and in a larger memory usage). The optimum is to be in an equilibrium between the rapidity and the precision of the algorithm. Note that by increasing the order of the method one can use a larger temporal step $\Delta t$.

Making a further step in Navier–Stokes direction one notes that indeed the Navier–Stokes equation is better represented by:

$$\dot{x}(t) = F(x) + Ax \tag{B.26}$$

where $A$ does not depend on $x$ and hence the second term on the right-hand side is linear. In Navier–Stokes equation this term corresponds to the viscous term, while the nonlinear term corresponds to the advection term. In this case a new variable $y$ can be introduced:

$$x(t) = y(t)\mathrm{e}^{At} \tag{B.27}$$

for which the Eq. (B.26) becomes

$$\dot{y}(t) = \mathrm{e}^{-At} F(y\mathrm{e}^{At}) \quad . \tag{B.28}$$

For illustrative purpose the Euler scheme is now applied to this equation

$$y(t+\Delta t) \simeq y(t) + \mathrm{e}^{-At} F(y\mathrm{e}^{At})\Delta t \tag{B.29}$$

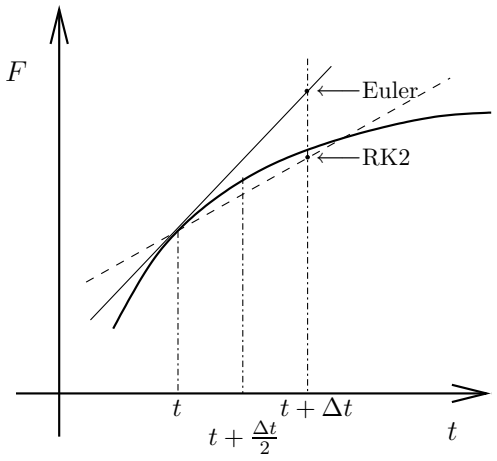


**Figure B.2:** The geometric representation of the Euler and RK2 methods. In RK2 the value of $F$ at $t+\Delta t$ is found following the tangent in the midpoint (RK2 is also called Midpoint Derivative Method).

and thus, going back to $x(t)$

$$x(t+\Delta t)\mathrm{e}^{-A(t+\Delta t)} \simeq y(t) + \mathrm{e}^{-At}F(x)\Delta t = \mathrm{e}^{-At}x(t) + \mathrm{e}^{-At}F(x)\Delta t \tag{B.30}$$

from which the following scheme (exact in the linear part, Euler in the nonlinear part) is given:

$$x(t+\Delta t) = \mathrm{e}^{A\Delta t}\left(x(t) + F(x)\Delta t\right) \quad . \tag{B.31}$$

In the case of a RK2 integrator, the above approach leads to the following second-order scheme:

$$x(t+\Delta t) = e^{A\Delta t}x(t) + \mathrm{e}^{A\frac{\Delta t}{2}}\Delta t F\left[e^{A\frac{\Delta t}{2}}\left(x + \frac{\Delta t}{2}F(x)\right)\right] \quad . \tag{B.32}$$

In the case of Navier–Stokes simulations, the viscous scales, where the dissipative linear term is relevant, are also the faster ones and require a small time step. The use of an exact scheme for the dissipative term is thus very convenient.

Another temporal scheme which is implemented on some versions of the code is the so-called Adams–Bashforth scheme which makes use of previous evaluations of the r.-h.s. This scheme is faster than RK2 (as it requires the evaluation of the r.-h.s. only once), but is more memory demanding and typically less accurate. The second-order version is (with the exact linear part)

$$x(t+\Delta t) = \mathrm{e}^{A\Delta t}\left[x(t) + \frac{\Delta t}{2}\left(3F(x) - \mathrm{e}^{A\Delta t}F(x(t-\Delta t))\right)\right] \quad . \tag{B.33}$$

### B.2.1 Which is the best way to integrate in time?

It is evident that, if one goes beyond first-order methods, there is a great freedom in discretizing differential equations, i.e., many discrete equations correspond to a single PDE. Among

these discrete schemes, it is important to choose a method which compromises among efficiency, memory and accuracy. In the following some simple considerations on accuracy and stability criteria are introduced.
Let us consider the linear PDE

$$\partial_t v + c\partial_x v = 0 \quad . \tag{B.34}$$

The simplest scheme is (first-order both in space and time):

$$\begin{cases} \partial_t v \to \frac{v_j^{n+1} - v_j^n}{\Delta t} \\ \partial_x v \to \frac{1}{2}\left[\frac{v_{j+1}^n - v_j^n}{\Delta x} + \frac{v_j^n - v_{j-1}^n}{\Delta x}\right] = \frac{v_{j+1}^n - v_{j-1}^n}{2\Delta x} \end{cases} \tag{B.35}$$

which yields the discrete equation:

$$v_j^{n+1} = v_j^n - \frac{c\Delta t}{2\Delta x}\left(v_{j+1}^n - v_{j-1}^n\right) \quad . \tag{B.36}$$

This explicit scheme is called Forward Time Centred Space (FTCS). Following the considerations first developed by von Neumann, it is simple to show that this discrete scheme is unstable. Let us consider the evolution of a Fourier mode

$$v_j^n = \sum_k \xi^n(k) \mathrm{e}^{ikj\Delta x} \tag{B.37}$$

where the amplitude $\xi(k) \in \mathbb{C}$ discriminates between stable $|\xi| < 1$ and unstable $|\xi| > 1$ modes. Substitution in Eq. (B.36) gives:

$$\left(\xi^{n+1}(k) - \xi^n(k)\right) \mathrm{e}^{ikj\Delta x} = -\frac{c\Delta t}{2\Delta x}\xi^n(k)\left(\mathrm{e}^{ik(j+1)\Delta x} - \mathrm{e}^{ik(j-1)\Delta x}\right) \tag{B.38}$$

thus

$$\xi = 1 - i\frac{c\Delta t}{\Delta x}\sin\left(k\Delta x\right) \tag{B.39}$$

and then one has instability ($|\xi| > 1$) for any $k$. Thus the FTCS scheme is unstable.
A possible improvement of (B.36) is the Lax stabilization based on the replacement

$$v_j^n \to \frac{1}{2}\left(v_{j+1}^n + v_{j-1}^n\right) \tag{B.40}$$

which gives the scheme

$$v_j^{n+1} = \frac{1}{2}\left(v_{j+1}^n + v_{j-1}^n\right) - \frac{c\Delta t}{2\Delta x}\left(v_{j+1}^n - v_{j-1}^n\right) \quad . \tag{B.41}$$

The von Neumann stability analysis gives now

$$\xi = \cos\left(k\Delta x\right) - i\frac{c\Delta t}{\Delta x}\sin\left(k\Delta x\right) \tag{B.42}$$

and thus the scheme is stable for

$$\frac{c\Delta t}{\Delta x} \leq 1 \quad . \tag{B.43}$$

The latest relation is the famous Courant stability criterion. The physical interpretation of (B.43) is simple: because information in (B.34) propagates at velocity $c$, the numerical scheme must resolve the smallest time, i.e. $\Delta t \leq \Delta x/c$.
Another interpretation of the Lax scheme is obtained by rewriting (B.41) as

$$\frac{v_j^{n+1} - v_j^n}{\Delta t} = -c\frac{v_{j+1}^n - v_{j-1}^n}{2\Delta x} + \frac{v_{j+1}^n - 2v_j^n + v_{j-1}^n}{2\Delta x} \tag{B.44}$$

which is a FTCS scheme for

$$\partial_t v + c\partial_x v = \frac{(\Delta x)^2}{2\Delta t}\,\partial_x^2 v \tag{B.45}$$

thus the Lax scheme is nothing but a numeric diffusivity.
The lesson from this brief discussion on stability criteria is that the development of discrete schemes is more an art than a science. Fortunately, by using a well-known scheme like the pseudospectral code, one does not need to investigate its stability. The only point is to keep $\Delta t$ sufficiently small to satisfy the Courant criterion.

## B.3 The pseudo-spectral code

### B.3.1 The 3D equations

The three-dimensional Navier–Stokes equation for the vorticity field $\boldsymbol{\omega} = \boldsymbol{\partial} \times \boldsymbol{v}$ is

$$\partial_t \boldsymbol{\omega} - \boldsymbol{\partial} \times (\boldsymbol{v} \times \boldsymbol{\omega}) = \nu \partial^2 \boldsymbol{\omega} \quad . \tag{B.46}$$

Introducing now the vector potential $\boldsymbol{b}$ defined by $\boldsymbol{v} = \boldsymbol{\partial} \times \boldsymbol{b}$ one has $\boldsymbol{\omega} = \boldsymbol{\partial}\,(\boldsymbol{\partial} \cdot \boldsymbol{b}) - \partial^2 \boldsymbol{b}$. Because the scalar field $\phi \equiv \boldsymbol{\partial} \cdot \boldsymbol{b}$ is conserved by Navier–Stokes equation, one can take $\phi = 0$ and hence $\boldsymbol{\omega} = -\partial^2 \boldsymbol{b}$. The equation of motion becomes

$$\partial_t \boldsymbol{b} + \left(\partial^2\right)^{-1} [\boldsymbol{\partial} \times (\boldsymbol{v} \times \boldsymbol{\omega})] = \nu \partial^2 \boldsymbol{b} \quad . \tag{B.47}$$

The numerical scheme integrates Eq. (B.47) by computing $\boldsymbol{v}$ and $\boldsymbol{\omega}$ from $\boldsymbol{b}$ in Fourier space, the product $\boldsymbol{v} \times \boldsymbol{\omega}$ in physical space and then derivatives back in Fourier space.

### B.3.2 The 2D equations

The two-dimensional Navier–Stokes equation can be written for scalar vorticity as

$$\partial_t \omega + J(\omega, \psi) = \nu \partial^2 \omega \tag{B.48}$$

where $\psi$ is the stream function defining the velocity $\boldsymbol{v} = (\partial_y \psi, -\partial_x \psi)$ and the Jacobian is $J(\omega, \psi) = \partial_x \omega \partial_y \psi - \partial_y \omega \partial_x \psi$.

### B.3.3 The viscous term

We have already discussed about the sequence of operations performed on the viscous term:

$$\nu \partial^2 v \longrightarrow -\nu k^2 \hat{v}(k) \longrightarrow e^{-\nu k^2 \Delta t}(\dots) \quad . \tag{B.49}$$

In fully developed turbulence the viscous dissipation also involves scales quite large. To enlarge the inertial range a numerical artifice could be typically introduced: the viscous term is replaced by the 'hyper-viscous' one $(-1)^p \nu_p \partial^{2p} v$ which permits to eliminate the spurious effects of the viscosity of the inertial scale.

### B.3.4 Structure of the code

Let us briefly describe the code structure.
After reading the initial conditions (the velocity field in 3D and the vorticity in 2D), these ones are calculated in Fourier space. The nonlinear term, which takes as input the field $\hat{\boldsymbol{b}}$ in 3D and $\hat{\omega}$ in 2D, produces the nonlinear term in Fourier space. In our case, the forcing (i.e., the buoyancy term) is added here. The dealiasing is performed. The time integration RK2 is made in two steps.
In the system which we expect, there are also the scalar-field (temperature or phase field) equation and/or the equations for components of polymer-conformation tensor. These equations are integrated in a way similar to the Navier–Stokes equation.

#### B.3.4.1 The nonlinear term

**3D**

The nonlinear term is:

$$\mathcal{N} = \left(\partial^2\right)^{-1} \boldsymbol{\partial} \times (\boldsymbol{v} \times \boldsymbol{\omega}) \quad . \tag{B.50}$$

The field $\hat{\boldsymbol{b}}$ is the input. The quantity $\hat{\boldsymbol{v}} = i\boldsymbol{k} \times \hat{\boldsymbol{b}}$ is calculated. Then we work out the vorticity $\hat{\boldsymbol{\omega}} = k^2\hat{\boldsymbol{b}}$.
The velocity and the vorticity are calculated in physical space (it has to call 6 times the routine FFT_INV which performs the inverse FFT), their wedge are computed. Then the FFT_DIR (which obviously performs the direct FFT) is called three times to calculate the Fourier transform $\widehat{\boldsymbol{v} \times \boldsymbol{\omega}}$. Finally, the nonlinear term is computed as:

$$\hat{\mathcal{N}} = \frac{i\boldsymbol{k} \times \widehat{(\boldsymbol{v} \times \boldsymbol{\omega})}}{k^2} \quad . \tag{B.51}$$

The total number of FFT is 9.

**2D**

The nonlinear term is calculated as:

$$\hat{\mathcal{N}} = \widehat{\boldsymbol{\partial} \cdot (\boldsymbol{v}\omega)} = ik_x\widehat{u\omega} + ik_z\widehat{w\omega} \quad . \tag{B.52}$$

where we indicate the velocity components as $\boldsymbol{v} \equiv (u, 0, w)$. At first, the velocity is calculated in Fourier space as:

$$\hat{u} = -\frac{ik_z}{k^2}\hat{\omega} \quad \text{and} \quad \hat{w} = \frac{ik_x}{k^2}\hat{\omega} \quad . \tag{B.53}$$

Then we pass to physical space calling 3 inverse FFT, we compute the products $u\omega$ and $w\omega$ and finally we go back in Fourier space with 2 direct FFT where we calculate $\widehat{u\omega}$ and $\widehat{w\omega}$.

# Bibliography


[1] U. Alon, J. Hecht, D. Ofer, and D. Shvarts. Power laws and similarity of Rayleigh–Taylor and Richtmyer–Meshkov mixing fronts at all density ratio. *Phys. Rev. Lett.*, 74(4):534–537, 1995.

[2] Y. Amarouchene and H. Kellay. Polymers in 2D turbulence: suppression of large scale fluctuations. *Phys. Rev. Lett.*, 89(10):104502(1–4), 2002.

[3] G. Amati, K. Koal, F. Massaioli, K. R. Sreenivasan, and R. Verzicco. Turbulent thermal convection at high Rayleigh numbers for a Boussinesq fluid of constant Prandtl number. *Phys. Fluids*, 17:121701(1–4), 2005.

[4] D. M. Anderson, G. B. McFadden, and A. A. Wheeler. Diffuse-interface methods in fluid mechanics. *Ann. Rev. Fluid Mech.*, 30:139–397, 1998.

[5] P. E. Arratia, G. A. Voth, and J. P. Gollub. Stretching and mixing of non-Newtonian fluids in time-periodic flows. *Phys. Fluids*, 17(5):053102(1–10), 2005.

[6] V. E. Badalassi, H. D. Ceniceros, and S. Banrjee. Computation of multiphase systems with phase field meodels. *J. Comput. Phys.*, 190:371–397, 2003.

[7] E. Balkovsky and V. Lebedev. Instanton for the Kraichnan passive scalar problem. *Phys. Rev. E*, 58:5776–5795, 1998.

[8] G. K. Batchelor. *The theory of homogenous turbulence*. Cambridge University Press, Cambridge, 1953.

[9] G. K. Batchelor. Computation of the energy spectrum in homogeneous two-dimensional turbulence. *Phys. Fluids*, 12(Suppl. II):233–239, 1969.

[10] R. Benzi, S. Ciliberto, R. Tripiccione, C. Baudet, F. Massaioli, and S. Succi. Extended self-similarity in turbulent flows. *Phys. Rev. E*, 48(1):R29–R32, 1993.

[11] R. Benzi, V. S. L'vov, I. Procaccia, and V. Tiberkevich. Saturation of turbulent drag reduction in dilute polymer solutions. *Europhys. Lett.*, 68(6):825–831, 2004.

[12] D. Bernard. Turbulence for (and by) amateurs. *Arxiv preprint arXiv:0007106*, 2000.

[13] S. Berti. *Non-Newtonian turbulence: viscoelastic fluids and binary mixtures*. PhD thesis, Università di Torino (Italy) and Université de Nice-Sophia Antipolis (France), 2006.

[14] S. Berti, A. Bistagnino, G. Boffetta, A. Celani, and S. Musacchio. Small-scale statistics of viscoelastic turbulence. *Europhys. Lett.*, 76(1):63–69, 2006.

[15] S. Berti, G. Boffetta, M. Cencini, and A. Vulpiani. Turbulence and coarsening in active and passive binary mixtures. *Phys. Rev. Lett.*, 95:224501(1–4), 2005.

[16] L. Biferale and I. Procaccia. Anisotropy in turbulent flows and in turbulent transport. *Phys. Rep.*, 414(2-3):43–164, 2005.

[17] R. B. Bird, R. C. Armstrong, O. Hassager, and C. F. Curtiss. *Dynamics of polymeric liquids*. Wiley, New York, 1987.

[18] D. Biskamp. *Nonlinear Magnetohydrodynamics*. Cambridge University Press, Cambridge, 1993.

[19] G. Boffetta, A. Celani, and A. Mazzino. Drag reduction in the turbulent Kolmogorov flow. *Phys. Rev. E*, 71:036307(1–5), 2005.

[20] G. Boffetta, A. Celani, and S. Musacchio. Two-dimensional turbulence of diluite polymer solutions. *Phys. Rev. Lett.*, 91(3):034501(1–4), 2003.

[21] G. Boffetta, A. Celani, and M. Vergassola. Inverse energy cascade in two-dimensional turbulence: deviations from Gaussian behavior. *Phys. Rev. E*, 61(1):R29–R32, 2000.

[22] G. Boffetta, A. Mazzino, and A. Vulpiani. Twenty-five years of multifractals in fully developed turbulence: a tribute to Giovanni Paladin. *J. Phys. A: Math. Theor.*, 41:363001(1–25), 2008.

[23] G. Boffetta and G. P. Romano. Structure functions and energy dissipation dependence on Reynolds number. *Phys. Fluids*, 14(10):3453–3458, 2002.

[24] T. Bohr, M. H. Jensen, G. Paladin, and A. Vulpiani. *Dynamical systems approach to turbulence*. Cambridge University Press, Cambridge, 1998.

[25] A. Bray. Theory of phase-ordering kinetics. *Advances in Physics*, 51(2):481–587, 2002.

[26] W. H. Cabot and A. W. Cook. Reynolds number effects on Rayleigh–Taylor instability with possible implications for type-Ia supernovae. *Nature Physics*, 2:562–568, 2006.

[27] J. W. Cahn and J. E. Hilliard. Free energy of a non uniform system. I. Interfacial free energy. *J. Chem. Phys.*, 28:258–267, 1958.

[28] E. Calzavarini, D. Lohse, F. Toschi, and R. Tripiccione. Rayleigh and Prandtl number scaling in the bulk of Rayleigh–Bénard. *Phys. Fluids*, 17:055107–1–055107–7, 2005.

[29] C. Canuto, M. Y. Hussaini, A. Quarteroni, and T. A. Zang. *Spectral Methods in Fluid Dynamics*. Springer Series in Computational Physics. Springer-Verlag, New York, 1998.

[30] B. Castaing, Y. Gagne, E. J. Hopfinger, and R. A. Antonia. High-order velocity structure functions in turbulent shear flows. *J. Fluid Mech.*, 140:63–89, 1984.

[31] A. Celani, M. Cencini, A. Mazzino, and M. Vergassola. Active and passive fields face to face. *New J. Phys.*, 6:72(1–35), 2004.

[32] A. Celani, A. Lanotte, A. Mazzino, and M. Vergassola. Universality and saturation of intermittency in passive scalar turbulence. *Phys. Rev. Lett.*, 84(11):2385–2388, 2000.

[33] A. Celani, A. Lanotte, A. Mazzino, and M. Vergassola. Fronts in passive scalar turbulence. *Phys. Fluids*, 13(6):1768–1783, 2001.

[34] A. Celani, T. Matsumoto, A. Mazzino, and M. Vergassola. Scaling and universality in turbulent convection. *Phys. Rev. Lett.*, 88:054503(1–4), 2002.

[35] A. Celani, A. Mazzino, and M. Vergassola. Thermal plume turbulence. *Phys. Fluids*, 13(7):2133–2135, 2001.

[36] A. Celani and M. Vergassola. Statistical geometry in scalar turbulence. *Phys. Rev. Lett.*, 86(3):424–427, 2001.

[37] F. H. Champagne. The fine-scale structure of the turbulent velocity field. *J. Fluid Mech.*, 86:67–108, 1978.

[38] D. C. Champeney. *Fourier transforms and their physical applications*. Academic Press, New York, 1973.

[39] S. Chandrasekhar. *Hydrodynamic and Hydromagnetic Stability*. The International Series of Monographs on Physics. Clarendon Press, Oxford, 1961.

[40] M. Chertkov. Instanton for random advection. *Phys. Rev. E*, 55(3):2722–2735, 1997.

[41] M. Chertkov. Phenomenology of Rayleigh–Taylor turbulence. *Phys. Rev. Lett.*, 91(11):115001(1–4), 2003.

[42] M. Chertkov, G. Falkovich, I. Kolokolov, and V. Lebedev. Statistics of the passive scalar advected by a large-scale two-dimensional velocity field: analytical solution. *Phys. Rev. E*, 51:4924–4941, 1995.

[43] M. Chertkov, I. Kolokolov, and V. Lebedev. Effects of surface tension on immiscible Rayleigh–Taylor turbulence. *Phys. Rev. E*, 71:055301(R)(1–4), 2005.

[44] M. Chertkov and N. Vladimirova. Self-similarity and universality in Rayleigh-Taylor, Boussinesq turbulence. *Arxiv preprint arXiv:0801.2981*, 2008.

[45] T. T. Clark. A numerical study of the statistics of a two-dimensional Rayleigh–Taylor mixing layer. *Phys. Fluids*, 15(8):2413–2423, 2003.

[46] A. W. Cook, W. H. Cabot, and P. L. Miller. The mixing transition in Rayleigh–Taylor instability. *J. Fluid Mech.*, 511:333–362, 2004.

[47] J. W. Cooley and J. W. Tukey. An algorithm for the machine calculation of complex Fourier series. *Math. Comput.*, 19:297–301, 1965.

[48] S. B. Dalziel, P. F. Linden, and D. L. Youngs. Self-similarity and internal structure of turbulence induced by Rayleigh–Taylor instability. *J. Fluid Mech.*, 399:1–48, 1999.

[49] G. C. Danielson and C. Lanczos. Some improvements in practical Fourier analysis and their application to X-ray scattering from liquids. *J. Franklin Inst.*, 233(4 and 5):365–380 and 435–452, 1942.

[50] E. De Angelis, C. M. Casciola, V. S. L'vov, R. Piva, and I. Procaccia. Drag reduction by polymers in turbulent channel flows: energy redistribution between invariant empirical modes. *Phys. Rev. E*, 67(5):056312(1–12), 2003.

[51] R. C. di Prima and H. L. Swinney. Instabilities and transition in flow between concentric rotating cylinders. In H.L. Swinney and J.P. Gollub, editors, *Hydrodynamic Instabilities and the Transition to Turbulence*, volume 45 of *Topics in Applied Physics*, Berlin, 1981. Springer.

[52] R. W. Dibble, J. Warnatz, and U. Maas. *Combustion: physical and chemical fundamentals, modelling and simulations, experiments, pollutant formation*. Springer, New York, 1996.

[53] G. Dimonte and M. Schneider. Density ratio dependence of Rayleigh–Taylor mixing for sustained and impulsive acceleration histories. *Phys. Fluids*, 12(2):304–321, 2000.

[54] G. Dimonte, D. L. Young, A. Dimitis, S. Weber, M. Marinak, S. Wunsch, C. Garasi, A. Robinson, M. J. Andrews, P. Ramabrabhu, A. C. Calder, B. Fryxell, J. Biello, L. Dursi, P. MacNeice, K. Olson, P. Ricker, R. Rosner, F. Timmes, H. Tufo, Y. N. Young, and M. Zingale. A comparative study of the turbulent Rayleigh–Taylor instability using high-resolution three-dimensional numerical simulations: The Alpha-Group collaboration. *Phys. Fluids*, 16(5), 2004.

[55] H. Ding, P. D. M. Spelt, and C. Shu. Diffuse interface model for incompressible two-phase flows with large density ratios. *J. Comput. Phys.*, 226(2):2078–2095, 2007.

[56] M. Ducea and J. Saleeby. A case of delamination of the deep batholithic crust beneath the Sierra Nevada, California. *Int. Geology Rev.*, 40:78–93, 1998.

[57] R. E. Duff, F. H. Harlow, and C. W. Hirt. Effects of diffusion on interface instability between gases. *Phys. Fluids*, 5(4):417–425, 1962.

[58] G. Falkovich, K. Gawedzki, and M. Vergassola. Particles and fields in fluid turbulence. *Rev. Mod. Phys.*, 73(4):913–975, 2001.

[59] G. Falkovich, V. S. L'vov, and V. E. Zakharov. *Kolmogorov Spectra of Turbulence I*. Springer, 1992.

[60] U. Frisch. *Turbulence. The legacy of A. N. Kolmogorov*. Cambridge University Press, 1995.

[61] U. Frisch, M. Martins Afonso, A. Mazzino, and V. Yakhot. Does multifractral theory of turbulence have logarithms in the scaling relations? *J. Fluid Mech.*, 542:97–103, 2005.

[62] S. Fujioka, A. Sunahara, K. Nishihara, N. Ohnishi, and T. Johzaki. Suppression of the Rayleigh–Taylor instability due to self-radiation in a multiablation target. *Phys. Rev. Lett.*, 92(19):195001(1–4), 2004.

[63] K. Gawedzki and A. Kupiainen. Anomalous scaling of the passive scalar. *Phys. Rev. Lett.*, 75:3834–3837, 1995.

[64] J. A. Glazier, T. Segawa, A. Naert, and M. Sano. Evidence against "ultrahard" thermal turbulence at very high Rayleigh numbers. *Nature*, 398:307–310, 1999.

[65] V. N. Goncharov. Analytical model of nonlinear, single-mode, classical Rayleigh–Taylor instability at arbitrary Atwood numbers. *Phys. Rev. Lett.*, 88(13):134502(1–4), 2003.

[66] T. Gotoh, D. Fukayama, and T. Nakano. Velocity field statistics in homogeneous steady turbulence obtained using a high-resolution direct numerical simulation. *Phys. Fluids*, 14(3):1065–1081, 2002.

[67] H. L. Grant, R. W. Stewart, and A. Moilliet. Turbulence spectra from a tidal channel. *J. Fluid Mech.*, 12(2):241–263, 1962.

[68] A. Groisman and V. Steinberg. Elastic versus iniertial instability in a polymer solution flow. *Europhys. Lett.*, 43(2):165–170, 1998.

[69] A. Groisman and V. Steinberg. Elastic turbulence in a polymer solution flow. *Nature*, 405(53–55), 2000.

[70] A. Groisman and V. Steinberg. Efficient mixing of liquids at low Reynolds numbers using polymer additives. *Nature*, 410:905–908, 2001.

[71] A. Groisman and V. Steinberg. Elastic turbulence in curvilinear flows of polymer solutions. *New J. Phys.*, 6:29(1–48), 2004.

[72] S. Grossmann and D. Lohse. Scaling in thermal convection: a unifying theory. *J. Fluid Mech.*, 407:27–56, 2000.

[73] A. Gyr and H. W. Bewersdorff. *Drag reduction of turbulent flows by additives*. Kluwer Academic, 1995.

[74] J. Herweijer and W. Van de Water. Universal shape of scaling functions in turbulence. *Phys. Rev. Lett.*, 74(23):4651–4654, 1995.

[75] E. J. Hinch. Mechanical models of diluite polymer solutions in strong flows. *Phys. Fluids*, 20:S22–S30, 1977.

[76] H. Isobe, T. Miyagoshi, K. Shibata, and T. Yokoyama. Filamentary structure on the Sun from the magnetic Rayleigh–Taylor instability. *Nature*, 434:478–481, 2005.

[77] D. Jacqmin. Calculation of two-phase Navier–Stokes flows using phase-field modeling. *J. Comput. Phys.*, 155:96–127, 1999.

[78] H. Kellay and J. P. Gollub. Two-dimensional turbulence: a review of some recent experiments. *Rep. Prog. Phys.*, 65:845–894, 2002.

[79] A. N. Kolmogorov. Energy dissipation in locally isotropic turbulence. *Dokl. Akad. Nauk. SSSR*, 32:19–21, 1941.

[80] A. N. Kolmogorov. Local structure of turbulence in an incompressible fluid for very large Reynolds numbers. *Dokl. Akad. Nauk. SSSR*, 30:299–303, 1941.

[81] A. N. Kolmogorov. A refinement of previous hypotheses concerning the local structure of turbulence in a viscous incompressible fluid at high Reynolds number. *J. Fluid Mech.*, 13:82–85, 1962.

[82] R. H. Kraichnan. Turbulent thermal convection at arbitrary Prandtl number. *Phys. Fluids*, 5:1374–1389, 1962.

[83] R. H. Kraichnan. Inertial ranges transfer in two-dimensional turbulence. *Phys. Fluids*, 10:1417–1423, 1967.

[84] R. H. Kraichnan. Anomalous scaling of a randomly advected passive scalar. *Phys. Rev. Lett.*, 72:1016–1019, 1972.

[85] R. H. Kraichnan and D. Montgomery. Two-dimensional turbulence. *Rep. Prog. Phys.*, 43:547–618, 1980.

[86] P. K. Kundu and I. M. Cohen. *Fluids Mechanics*. Elsevier Academic Press, 2nd edition, 2001.

[87] M. Lafay, B. Le Creurer, and S. Gauthier. Compressibility effects in the Rayleigh–Taylor instability for miscible fluids. In J. M. L. M. Palma and A. Silva Lopes, editors, *Advances in Turbulence XI - Proceedings of the 11th EUROMECH European Turbulence Conference, June 25–28, 2007 Porto, Portugal*, volume 117 of *Springer Proceedings in Physics*. Springer, 2007.

[88] L. D. Landau and E. M. Lifshitz. *Fluids Mechanics volume 6 of course of Theoretical physics*. Butterworth Heinemann, 2nd (revised) edition, 2000.

[89] A. G. W. Lawrie. Light-Induced Fluorescence (LIF) complex Rayleigh–Taylor using a reacting tracer. `www.damtp.cam.ac.uk/lab/people/agwl2/research.html`. A visualisation of experiment carried out at Cambridge Laboratory. The experiment is performed in a tank. Initially the denser fluid is above the lighter fluid, these layers being separated by a metallic barrier. At $t = 0$ the barrier is removed and the instability develops. Unfortunately, the removal of the barrier does not permit to control the initial perturbation carefully. Indeed the removal introduces unwanted large-scale disturbances into the flow.

[90] D. Layzer. On the instability of superposed fluids in a gravitational field. *Astrophys. J.*, 122:1–22, 1955.

[91] C.-T. Lee, R. L. Rudnick, and G. H. Jr Brimhall. Deep lithospheric dynamics beneath the Sierra Nevada during the Mesozoic and Cenozoic as inferred from xenolith petrology. *Geochem. Geophys. Geosys.*, 2(12):2001GC000152, 2001.

[92] C. Liu and J. Shen. A phase-field model for the mixture of two incompressible fluids and its approximation by a Fourier-spectral method. *Physica D*, 179(3):211–228, 2003.

[93] D. Lohse and F. Toschi. Ultimate state of thermal convection. *Phys. Rev. Lett.*, 90(3):034502(1–3), 2003.

[94] J.L. Lumley. Drag reduction by additives. *Ann. Rev. Fluid Mech.*, 1:367–384, 1969.

[95] V. S. L'vov, A. Pomyalov, I. Procaccia, and V. Tiberkevich. Drag reduction by polymers in wall bounded turbulence. *Phys. Rev. Lett.*, 92(24):244503(1–4), 2004.

[96] Y. Malécot, C. Auriault, H. Kahalerras, Y. Gagne, O. Chanal, B. Chabaud, and B. Castaing. A statistical estimator of turbulence intermittency in physical and numerics experiments. *Europhys. Lett. B*, 16(3):549–561, 2000.

[97] J. Maurer, P. Tabeling, and G. Zocchi. Statistics of turbulence between two counter-rotating disks in low temperature Helium gas. *Europhys. Lett.*, 26:31–36, 1994.

[98] C. Meneveau and K. R. Sreenivasan. Simple multifractals cascade model for fully developed turbulence. *Phys. Rev. Lett.*, 59(13):1424–1427, 1987.

[99] R. Menikoff, R. C. Mjolsness, D. H. Sharp, and C. Zemach. Unstable normal mode for Rayleigh–Taylor instability in viscous fluids. *Phys. Fluids*, 20(12):2000–2004, 1977.

[100] K.O. Mikaelian. Effects of viscosity on Rayleigh–Taylor and Richtmyer–Meshov instabilities. *Phys. Rev. E*, 47(1):375–383, 1993.

[101] A. S. Monin and A. M. Yaglom. *Statistical Fluids Mechanics – vol. 1 and 2*. MIT press, Cambridge, U.S.A., 1971 and 1975.

[102] S. Musacchio. *Effects of friction and polymers on 2D turbulence*. PhD thesis, Università di Torino (Italy), 2003.

[103] J. J. Niemela, L. Skrbek, K. R. Sreenivasan, and R. J. Donnelly. Turbulent convection at very high Rayleigh numbers. *Nature*, 404:837–840, 2000.

[104] A. Nikolaenko and G. Ahlers. Nusselt number measurements for turbulent Rayleigh–Bénard convection. *Phys. Rev. Lett.*, 91(8):084501(1–4), 2003.

[105] A. M. Obukhov. Some specific features of atmospheric turbulence. *J. Fluid Mech.*, 13:77–81, 1962.

[106] S. A. Orszag. On the elimination of aliasing in finite difference schemes by filtering high-wavenumber components. *J. Atm. Sci.*, 28(6):1074, 1971.

[107] G. Paladin and A. Vulpiani. Anomalous scaling laws in multifractal objects. *Phys. Rep.*, 156(4):147–225, 1987.

[108] J. Paret and P. Tabeling. Intermittency in the two-dimensional inverse cascade of energy: Experimental observations. *Phys. Fluids*, 10(12):3126–3136, 1998.

[109] G. Parisi and U. Frisch. On the singularity structure of fully developed turbulence. In M. Ghil, R. Benzi, and G. Parisi, editors, *Turbulence and predictability in geophysical fluid dynamics, Proceed. Intern. School of Physics "E. Fermi", 1983, Varenna, Italy*, pages 84–87, Amsterdam, 1985. North-Holland.

[110] F. Pasquilli and Smith F. B. *Atmospheric diffusion*. Ellis Horwood, Chichester, 1983.

[111] T. T. Perkins, S. R. Quake, D. E. Smith, and S. Chu. Relaxation of a single DNA molecule onserved by optical microscopy. *Science*, 264(5160):822–826, 1994.

[112] N. A. Phillips. The general circulation of the atmosphere: A numerical experiment. *Quart. J. Roy. Met. Soc.*, 82:123–164, 1956.

[113] N. A. Phillips. An example of nonlinear computational instability. *The Atmosphere and the Sea in Motion*, pages 501–504, 1959.

[114] O. Poujade. Rayleigh–Taylor turbulence in nothing like Kolmogorov turbulence in the self-similar regime. *Phys. Rev. Lett.*, 97:185002(1–4), 2006.

[115] W. H. Press, S. A. Teukolsky, W. T. Vetterling, and B. P. Flannery. *Numerical recipes in Fortran - The art of scientific computing*. Cambridge University Press, 2nd edition, 1992.

[116] A. N. Pushkarev and V. E. Zakharov. Turbulence of capillary waves. *Phys. Rev. Lett.*, 76(18):3320–3323, 1996.

[117] A. N. Pushkarev and V. E. Zakharov. Turbulence of capillary waves – theory and numerical simulation. *Physica D*, 135:98–116, 2000.

[118] P. Ramabrabhu and M. J. Andrews. Experimental investigation of Rayleigh–Taylor mixing at small Atwood numbers. *J. Fluid Mech.*, 502:233–271, 2004.

[119] P. Ramaprabhu, G. Dimonte, and M. J. Andrews. A numerical study of the influence of initial perturbations on the turbulent Rayleigh–Taylor instability. *J. Fluid Mech.*, 536:285–319, 2005.

[120] Lord Rayleigh. Investigation of the character of the equilibrium of an incompressible heavy fluid of variable density. *Proc. London Math. Soc.*, 14:170–177, 1883.

[121] S. P. Regan, J. A. Delettrez, F. J. Marshall, J. M. Soures, V. A. Smalyuk, B. Yaakobi, R. Epstein, V. Yu. Glebov, P. A. Jaanimagi, D. D. Meyerhofer, P. B. Radha, T. C. Sangster, W. Seka, S. Skupsky, C. Stoeckl, and R. P. J. Town. Shell mix in the compressed core of spherical implosions. *Phys. Rev. Lett.*, 89(8):085003(1–4), 2002.

[122] O. Reynolds. An experimental investigation of the circumstances which determine whether the motion of water shall be direct os sinuous and the law of resistance in parallel channels. *Phil. Trans. R. Soc. London*, 174(935–982), 1883.

[123] L. F. Richardson. *Weather prediction by numerical process*. Cambridge University Press, Cambridge, 1922.

[124] J. R. Ristorcelli and T. T. Clark. Rayleigh–Taylor turbulence: self-similar analysis and direct numerical simulations. *J. Fluid Mech.*, 507:213–253, 2004.

[125] D. M. Schultz, K. M. Kanak, J. M. Straka, R. J. Trapp, B. A. Gordon, D. S. Zrnić, G. H. Bryan, A. J. Durant, T. J. Garrett, P. K. Klein, and D. K. Lilly. The mysteries of Mammatus clouds: observations and formation mechanisms. *J. Atmos. Sci.*, 10:2409–2435, 2006.

[126] A. J. Sethian. *Level Set methods and Fast Marching Methods: Evolving Interfaces in Computational Geometry, Fluid Mechanics, Computer Vision and Materials Science*. Cambridge University Press, Cambridge, 1999.

[127] D. H. Sharp. An overview of Rayleigh–Taylor instability. *Physica D*, 12:3–18, 1984.

[128] B. I. Shraiman and E. D. Siggia. Scalar turbulence. *Nature*, 405:639–646, 2000.

[129] E. D. Siggia. High Rayleigh number convection. *Ann. Rev. Fluid Mech.*, 26:137–168, 1994.

[130] L. M. Smith and V. Yakhot. Bose condensation and small-scale structure generation in a random force driven 2D turbulence. *Phys. Rev. Lett.*, 71:352–355, 1993.

[131] A. Smolianski, H. Haario, and P. Luukka. Vortex shedding behind a rising bubble and two-bubble coalescence: A numerical approach. *Appl. Math. Model*, 29:615–632, 2005.

[132] K. R. Sreenivasan. On local isotropy of passive scalars in turbulence shear flow. *Proc. R. Soc. Lon. A*, 434:165–182, 1991.

[133] K. R. Sreenivasan and R. A. Antonia. The phenomenology of small-scale turbulence. *Ann. Rev. Fluid Mech.*, 29:435–472, 1997.

[134] K. R. Sreenivasan and P. Kailasnath. An update on the intermittency exponent in turbulence. *Phys. Fluids A*, 5(2):512–514, 1993.

[135] K. R. Sreenivasan and C. M. White. The onset of drag reduction by dilute polymer additive, and the maximum drag reduction asymptote. *J. Fluid Mech.*, 409:149–164, 2000.

[136] P. Tabeling. Two-dimensional turbulence: a physicist approach. *Phys. Rep.*, 362:1–62, 2002.

[137] M. Tabor and P. G. de Gennes. A cascade theory of drag reduction. *Europhys. Lett.*, 2:519–522, 1986.

[138] Sir G. Taylor. The instability of liquid surfaces when accelerates in a direction perpendicular to their planes I. *Proc. R. Soc. A*, 201:192–197, 1950.

[139] B. A. Toms. Some observations on the flow of linear polymer solutions through straight tubes at large Reynolds numbers. In North Holland, editor, *Proceedings of the International Congress on Reology*, volume II, pages 135–141, Amsterdam, 1949.

[140] C. Van Atta and R. Antonia. Reynolds number dependence of skewness and flatness factors of turbulent velocity derivatives. *Phys. Fluids*, 23(2):252–257, 1980.

[141] J. T. Waddell, C. E. Niederhaus, and J. W. Jacobs. Experimental study of Rayleigh–Taylor instability: low Atwood number systems with single-mode initial perturbations. *Phys. Fluids*, 13(5):1263–1273, 2001.

[142] Z. Warhaft. Passive scalars in turbulent flows. *Ann. Rev. Fluid Mech.*, 32:203–240, 2000.

[143] J. C. Wyngaard and H. Tennekes. Measurements of the small-scale structure of turbulence at moderate Reynolds number. *Phys. Fluids*, 12:1962–1969, 1970.

[144] X. Xu, K. M. S. Bajaj, and G. Ahlers. Heat transport in turbulent Rayleigh–Bénard convection. *Phys. Rev. Lett.*, 84(19):4357–4360, 2000.

[145] A. M. Yaglom. On the local structure of a temperature field in a turbulent flow. *Dokl. Akad. Nauk. SSSR*, 69(743–746), 1949.

[146] P. K. Yeung, S. B. Pope, A. G. Lamorgese, and D. A. Donzis. Acceleration and dissipation statistics of numerically simulated isotropic turbulence. *Phys. Fluids*, 18(6):065103(1–14), 2006.

[147] D. L. Young. Numerical simulation of Rayleigh–Taylor instability. *Physica*, 12(D):12–44, 1984.

[148] Y. N. Young and F. E. Ham. Surface tension in incompressible Rayleigh–Taylor mixing flow. *J. Turbul.*, 71(7):1–23, 2006.

[149] Y. N. Young, H. Tufo, A. Dubey, and R. Rosner. On the miscibile Rayleigh–Taylor instability: two and three dimensions. *J. Fluid Mech.*, 447:377–408, 2001.

[150] D. L. Youngs. Three-dimensional numerical simulation of turbulent mixing by Rayleigh–Taylor instability. *Phys. Fluids A*, 3:1312–1320, 1991.

[151] P. Yue, J. J. Feng, and J. Shen. A diffuse-interface method for simulating two-phase flows of complex fluids. *J. Fluid Mech.*, 515:293–317, 2004.

[152] N. J. Zabusky. Vortex paradigm for accelerated inhomogeneous flows: Visiometrics for the Rayleigh–Taylor and Richtmer-Meshkov environments. *Ann. Rev. Fluid Mech.*, 31(495–536), 1999.

[153] V. E. Zakharov and N. N. Filonenko. The energy spectrum for stochastic oscillation of a fluid surface. *Dokl. Akad. Nauk. SSSR*, 170(6):1292–1295, 1966.

[154] Y. B. Zeldovich, A. Ruzmaikin, and D. Sokoloff. *Magnetic field in astrophisics*. Gordon and Breach, New York, 1983.

[155] M. Zingale, S. E. Woosley, J. B. Bell, M. S. Day, and C. A. Rendleman. The physics of flames in type Ia supernovae. *Astrophys. J.*, 632:1021–1026, 2005.

# Acknowledgements - Ringraziamenti

*"... E un canarino canterino addomesticherò*
*per le giornate scure*
*di quando il mare e il cielo dicono di no*
*e non si può viaggiare..."*
Un aeroplano a vela Song of Gianmaria Testa (1995)

Vorrei ringraziare innanzitutto Andrea Mazzino, il mio relatore, per la sua costante e paziente guida nel mondo della turbolenza. Grazie anche a coloro con cui ho avuto la fortuna di lavorare e a cui devo, quindi, il concretizzarsi di questa tesi: Guido Boffetta, Antonio Celani, ovviamente Andrea, Paolo Muratore-Ginanneschi e Stefano Musacchio. Ringrazio Paolo anche per l'accoglienza riservatami nel periodo trascorso ad Helsinki.
Grazie a Marco Martins Afonso e al Prof. Roberto Festa per la disponibilità in fase di scrittura della tesi.
Grazie Marco per essere sempre disponibile a rispondere ai miei quesiti scientifici (e di inglese!), alle lunghe chiacchierate su skype e per gli innumerevoli incoraggiamenti!
Vorrei ringraziare anche Alessandro Bottaro e Damien Biau con cui ho avuto l'opportunità di lavorare e discutere.
Grazie a tutto coloro che hanno fatto o che continuano a far parte del gruppo di atmosfera e con cui ho lavorato fianco a fianco in questi anni: Anita Visintini, il Prof. Corrado Ratto, Massimiliano Burlando, Marta Antonelli, Elisabetta Brogi, Marina Pizzo, Federico Cassola, Luca Villa, Patrizia De Gaetano, Aldo Gastaldi, Daniele Vertua, Elisa Canepa, Andrea Bistagnino, Tommaso Magro, Valeria Kosir, Manuela Todini, Agnese Seminara e Fabrizio Rinaldi...
Grazie a Marco Tizzi e a Luigi Balduzzi, in loro ho trovato degli insostituibili compagni di dottorato e degli ottimi amici! Grazie per le nostre discussioni serie, i nostri pensieri in libertà, le risate e l'aiuto in questi anni!
Grazie ai miei amici vicini e lontani... grazie a Francesco, Marietta, Valentina C., a Giovanna per il buonoumore che riesce a trasmettermi in qualsiasi momento, Linda&Daniele, Valentina A., Roberto, Daniela, Paolo S., ai miei compagni di trekking Paola&Maurizio per i meravigliosi momenti condivisi in montagna, a Valentina Z. e a Mattia per la nostra profonda e sicura amicizia e per saper essere felici per me!
Grazie ai miei genitori... per essere un porto sicuro a cui approdare in qualsiasi frangente!
A Daniele per quanto ormai è passato, per quanto è ora e, spero, per quanto continuerà ad essere... insieme.